Principles of Nuclear Cardiology Imaging

2

Ernest V. Garcia, James R. Galt, Marina Piccinelli, and Ji Chen

Introduction

Nuclear cardiology imaging is solidly based on many branches of science and engineering, including nuclear, optical, and mathematical physics; electrical and mechanical engineering; chemistry; and biology. This chapter uses principles from these scientific fields to provide an understanding of both the signals used and the imaging system that captures these signals. These principles have been simplified to fit the scope of this atlas.

Nuclear cardiology's signal is a radioactive tracer, and its imaging systems are either single-photon emission CT (SPECT) or positron emission tomography (PET) cameras. This combination has met with remarkable success in clinical cardiology. This success is the result of the combination of sophisticated electronic nuclear instruments and a highly specific signal. The signal is as important as or more important than the imaging system, which can be explained with the following analogy: When we look at the heavens on a clear night, our naked eye can see stars, objects that are millions of miles away, yet when we look into our patients just a few feet away, even with sophisticated systems, we can sometimes miss a signal associated with cardiac disease. The reason is that a star generates an incredibly powerful signal surrounded by a dark background, a signal much more powerful than the signals we currently use. This analogy provides several lessons. First, it illustrates the need to continue to improve our signals. Second, it provides a motivation: By improving our signal, we have the capacity to detect anything. Finally, it explains the success of nuclear cardiology imaging over cardiovascular MRI, echocardiography, or CT for detecting perfusion abnormalities.

There is a misconception that MRI, echocardiogram, and CT are superior to nuclear cardiology imaging because of their superior spatial resolution. Yet, for detecting perfusion defects, what is really necessary is superior contrast resolution. It is this superior contrast resolution that allows us to differentiate between normal and hypoperfused myocardium, facilitating the visual analysis of nuclear cardiology perfusion images. Because these objects are bright compared with the background, we have been able to develop computer algorithms to totally, automatically, and objectively process and quantify our images, a feat yet to be successfully performed by other modalities.

This chapter explains the many important scientific principles necessary to understand this analogy, as well as nuclear cardiology imaging in general, starting from how radiation is emitted from a nucleus to how these sophisticated imaging systems detect this radiation. These principles are explained at a simple but highly applied level, so the nuclear cardiologist can understand them and apply them in routine clinical practice. The better one's understanding of how images are formed and what can go wrong in their formation, the higher one's accuracy in interpreting studies and the more successful one's practice should be.

E. V. Garcia (✉) · J. R. Galt · M. Piccinelli · J. Chen
Department of Radiology and Imaging Sciences, Emory University School of Medicine, Atlanta, GA, USA
e-mail: ernest.garcia@emory.edu

© Springer Nature Switzerland AG 2021

V. Dilsizian, J. Narula (eds.), *Atlas of Nuclear Cardiology*, https://doi.org/10.1007/978-3-030-49885-6_2

Fundamentals

Figures 2.1, 2.2, 2.3, 2.4, 2.5, and 2.6 introduce some of the fundamentals of radioactivity and radionuclides.

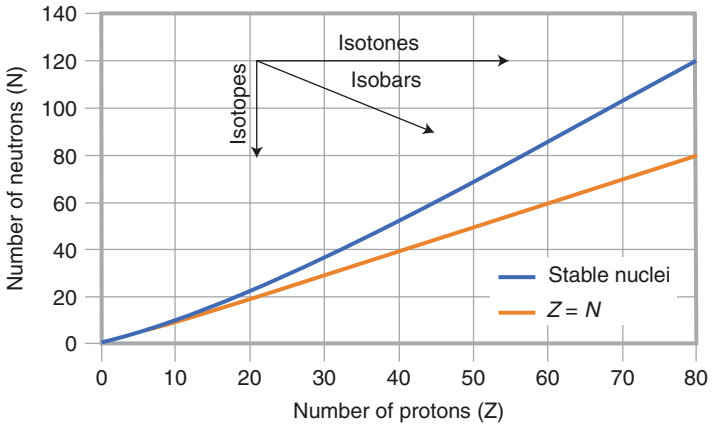

Fig. 2.1 Stability of the nucleus. This graph plots as a *blue line*, the number of neutrons versus the number of protons for stable nuclei. The *yellow line* indicates a neutron–proton ratio of 1. Only nuclides with low proton numbers fall on this line. For the *blue line*, note that as the number of protons increases, more neutrons are required to keep the nucleus stable. Nuclides with neutron–proton ratios that are not on the *blue line* of stable nuclei are unstable and, thus, radioactive. These radioactive nuclides are known as *radionuclides*. The type of radioactivity emitted depends on which side of the line the radionuclide is found. Isotopes are a family of nuclides that all have the same number of protons, or atomic number (Z), and are not necessarily radioactive. Isotones are nuclides with the same number of neutrons (N), and isobars have the same mass number (A) or number of mass particles in the nucleus ($A = Z + N$)

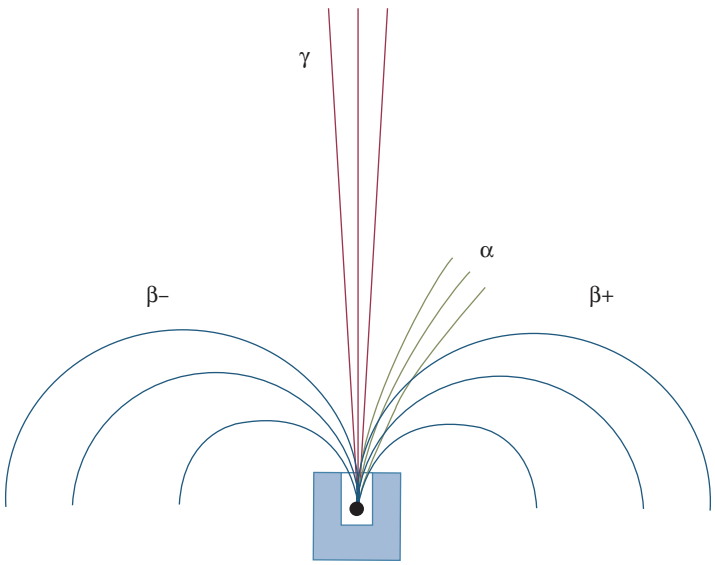

Fig. 2.2 Types of radiation. This diagram represents the path deviation of different types of radiation from nuclei by a magnetic field perpendicular to the page. The direction of the deflection depends on the charge of the radioactive particle. The least penetrating radiation is deflected to the right and corresponds to the heaviest radiation, called an alpha particle (α). An α particle is actually the nucleus of a helium atom (two protons plus two neutrons) with a positive charge. The moderately penetrating radiation deflected in the direction opposite to an α particle consists of negative particles called beta particles (β). Because these particles are more strongly bent, they are lighter than the α particles. The β particles are actually electrons emitted from the nucleus. Showing the same degree of penetration but bending in the direction opposite to the β particles are positron particles, or positive electrons (β+). These particles are made of antimatter and emitted by positron tracers. The radioactive particles that go straight and are not deflected do not consist of charged particles. They are called gamma (γ) rays and have been shown to be identical to particles emitted from an x-ray tube [1]. Both x-rays and γ-rays are called *photons* and are used in nuclear cardiology imaging

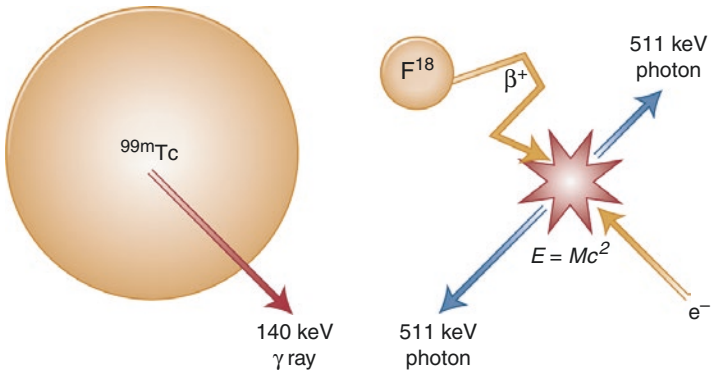

Fig. 2.3 Single-photon emission CT (SPECT) versus positron emission tomography (PET) radionuclides. This figure shows two very different types of radionuclides, technetium-99m (^{99m}Tc) and fluorine-18 (^{18}F). ^{99m}Tc is a large radionuclide that emits a single photon or γ-ray per radioactive decay that is used in SPECT to create images. The energy of the emitted photon is 140 keV (kiloelectron volts). The *m* in ^{99m}Tc means that the nucleus is metastable (almost stable but really unstable). ^{18}F is a much smaller radionuclide that emits a positron (β+) antiparticle. This ionized antiparticle travels through a medium interacting with it, losing energy and slowing down until it interacts with an electron, usually from some atom. Because the electron and the positron are antiparticles of each other (i.e., same mass but opposite charge), they undergo a phenomenon called *pair annihilation*. In pair annihilation, the mass of both particles disintegrates and is converted into energy as explained by Einstein's famous equation, $E = mc^2$, where E is the emitted energy, m is the mass of the two particles, and c is the speed of light in a vacuum. Because of the nature of the interaction, the energy is usually emitted in the form of two photons traveling in exactly opposite directions from each other and each having the same energy, 511 keV, which is the energy equivalent to the rest mass of an electron. These two photons are used to create images in PET

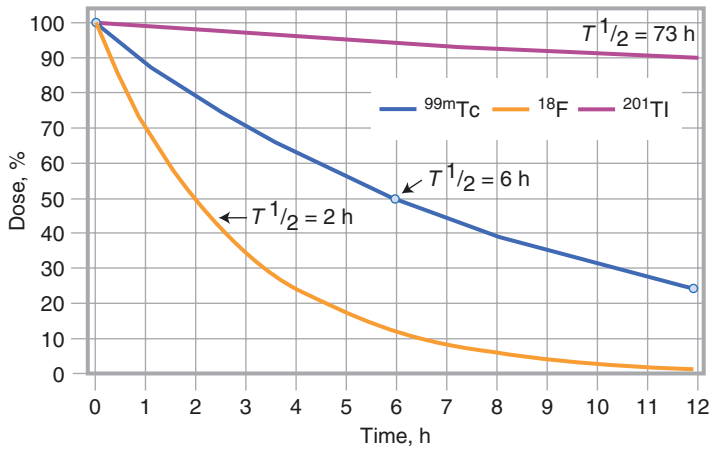

Fig. 2.4 Radioactive decay law: concept of half-life. This diagram shows decay curves for three different radionuclides: technetium-99m (^{99m}Tc), fluorine-18 (^{18}F), and thallium-201 (^{201}Tl). The decay curves express the amount of radioactive nuclides that have not decayed as a function of time. The shorter the interval between emissions for a specific radionuclide, the faster the radioactivity is depleted. It is practical to express the rate of radioactive transformations (disintegrations) by specifying the period during which half of all the atoms initially present will disintegrate. This period of time is known as the *half-life*, or T½. Note from the graph that the ^{18}F curve is disintegrating the fastest of the three radionuclides; it reaches a level of 50% of original at 2 hours; therefore, the half-life of ^{18}F is 2 hours. Compare this with the half-life of ^{201}Tl, which is 73 hours, and the half-life of ^{99m}Tc, which is 6 hours. The amount of radioactive nuclide is specified in terms of its disintegration rate or its activity. This relationship is provided by the radioactive decay law:

$$A(t) = A_0 e^{-(0.693t)} / T\frac{1}{2}.$$

In this equation, $A(t)$ is the radioactivity remaining at time t, A_0 is the activity at time 0, and $T½$ is the half-life of the radionuclide

A common unit of radioactivity is the curie (Ci), which is 3.7×10^{10} disintegrations per second. Another common unit of radioactivity used is the becquerel (Bq), which is one disintegration per second. One thousandth of a curie is a millicurie (mCi), which corresponds to 3.7×10^7 disintegrations per second. Note from the graph that if a 40-mCi dose of a ^{99m}Tc radiopharmaceutical (radioactive pharmaceutical) is delivered to an imaging clinic at 6 a.m., 6 hours later, at noon, only half—or 20 mCi—remains, and at 6 p.m., only half of that—or 10 mCi—remains

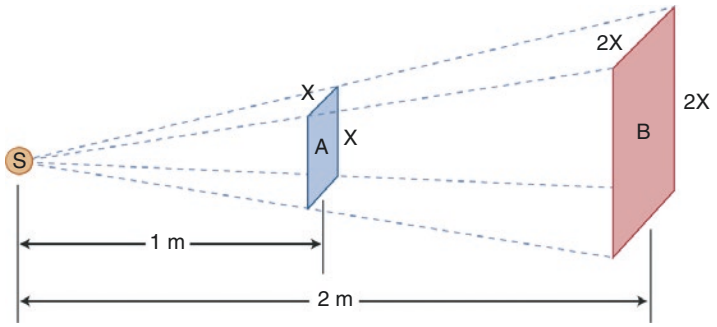

Fig. 2.5 Inverse square law. This diagram illustrates the concept of the inverse square law for radioactivity. The intensity of a radioactive point source at a distance from the source obeys the same law as for visible light. If the amount of radioactivity at the point source (*S*) remains constant, then the intensity of the radioactivity (number of photons) passing through a flat surface is inversely proportional to the square of the distance from the source. At a distance of 1 m, the diverging radioactive beam covers an area (*A*, *small square*) with each side of dimension *x*, or an area of x^2. At 2 m, the diverging beam covers an area (*B*, *large square*) in which each side is now twice as long as *A* (*2x*) and the area is $4x^2$, which is four times the area at 1 m. Because the amount of radioactivity remains constant, the number of photons falling on *square A* must spread out over four times as large an area by the time it reaches *square B*. Thus, the activity per unit area at *B*, which is twice as far as *A* from the source, is one fourth of the activity passing through *A* [2]. The value of this principle to radiation workers is that they can significantly reduce their radiation burden just by increasing their distance between themselves and a radioactive source, such as a patient already injected with a radioactive dose

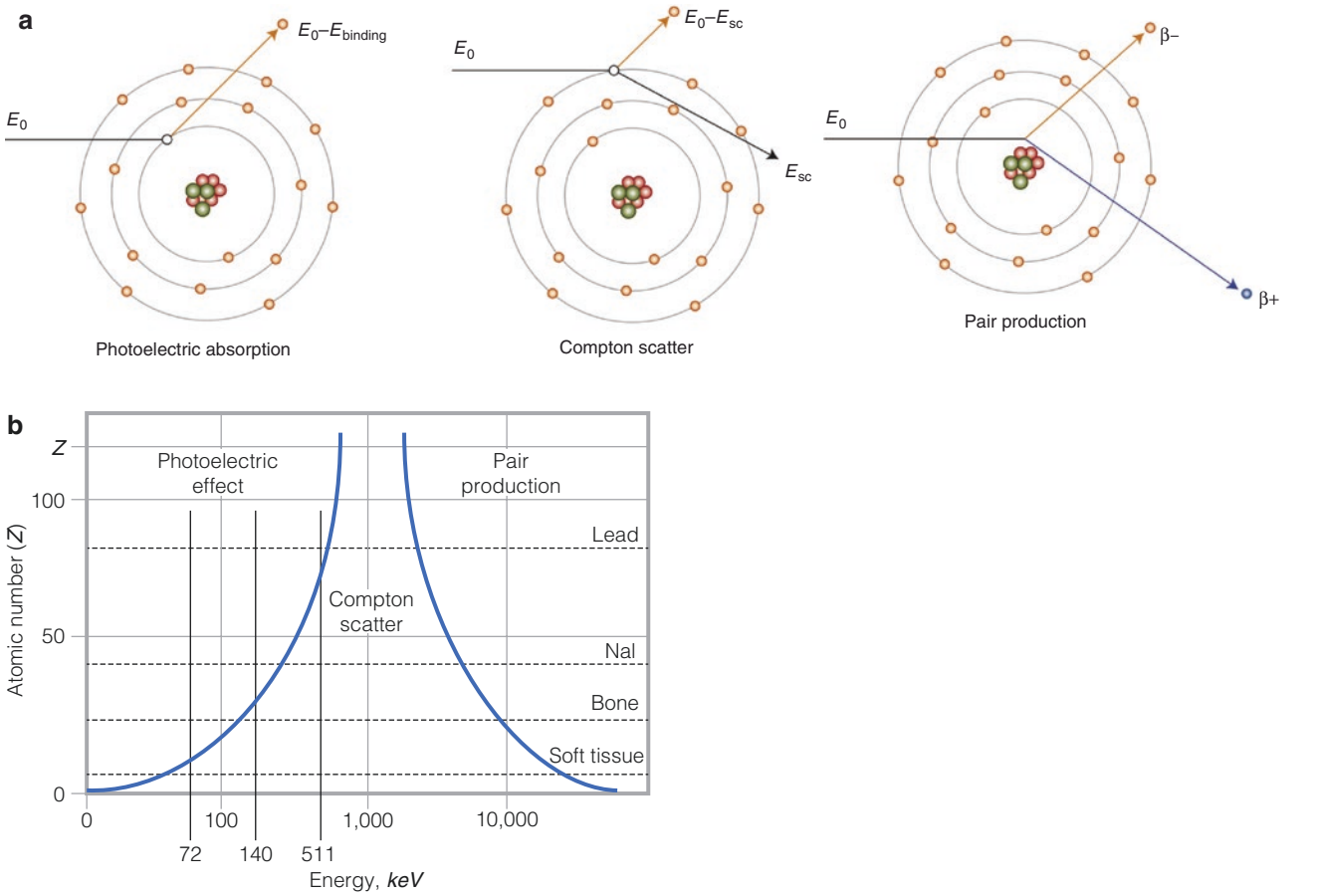

Fig. 2.6 Interaction of radiation with matter: photons. High-energy photons, such as γ-rays and x-rays, interact with matter in three ways that are relevant to nuclear medicine: through the photoelectric effect, Compton scattering, and pair production [3]. Each of these processes results in the emission of charged particles (electrons or positrons) that produce much more ionization than the original event. Thus, high-energy photons are classified as secondary ionizing radiation

(**a**) The photoelectric effect (or photoelectric absorption) occurs when a photon (γ- or x-ray) is completely absorbed as it interacts with an inner-shell electron. All the energy is lost to the electron, now called a *photoelectron*, which is emitted from the atom with an energy equivalent to the photon energy (E_0) less the binding energy of the electron ($E_{Binding}$). After photoelectric absorption, the atom has a vacancy in an inner electron shell that will be filled by an outer-shell electron, resulting in the emission of characteristic x-rays and possibly Auger electrons

Compton scattering occurs when a photon interacts with an outer-shell electron, changing its direction and losing some energy. The amount of energy of the photon after scattering depends on the angle of scatter (θ) according to the following formula:

$E_{sc} = E_0/1 + (E_0/551\ \text{keV}) \times (1 - \cos(\theta))$.

In this formula, E_0 is the energy of the photon before scattering, E_{sc} is the energy of the photon after scattering, and θ is the angle between the photon's original path and its new one. The larger the angle, the more energy is lost. Maximum energy is lost when the photon reverses course ($\theta = 180°$) and backscatters. All the energy lost to the γ-ray ($E_0 - E_{sc}$) is transferred to the electron, which on ejection from the atom is called a *recoil electron* (the binding energy of the outer-shell electron is negligible). Energies of Compton-scattered photons as a function of angle are given in Table 2.1

Pair production occurs when a photon passes near a charged particle (usually the nucleus of an atom). The photon is destroyed and a positron–electron pair (β+, β–) is created. According to the formula $E = mc^2$, the mass of the electron is equivalent to 511 keV; thus, the photon must have at least 1022 keV for pair production to occur. Energy in excess of 1022 keV is shared by the positron and the electron as kinetic energy. Because of the high energy required for the process, it is of little importance in clinical nuclear medicine laboratories

(**b**) The most probable interactions between high-energy photons and matter depend on the energy of the photons and the density of the material. Compton scattering is by far the most common interaction within the patient from the photons produced by clinical radiopharmaceuticals. The photoelectric effect is more likely to take place in the lead shielding of the collimator

Table 2.1 shows the relationship between the photopeak energy of common radionuclides used in nuclear cardiology, the scattering angle of the Compton-scattered photon, and the resulting energy of that photon. Note that in many instances, the original emitted photon may undergo a large scatter angle and still be counted by a 20% energy window in a camera's pulse height analyzer.

		Scattering angle			
Radionuclide	E_0, keV	30°	60°	90°	180°
Thallium-201	72	71	67	63	56
Technetium-99m	140	135	123	110	90
Positron annihilation	511	451	341	256	170

keV kiloelectron volts

Table 2.1 Energies of compton-scattered photons (E_0)

Figure 2.7 illustrates photon attenuation.

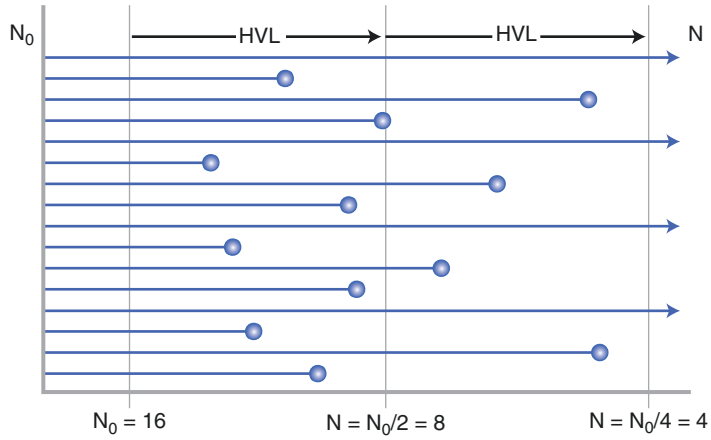

Fig. 2.7 Photon attenuation. As photons are absorbed through the photoelectric effect or scattered away from the detector through Compton scattering, their loss is called *attenuation*. The percentage of photons lost depends on the energy of the photons, the density of the material, and the material's thickness. The dependence on thickness is straightforward: the thicker the material, the more photons will be absorbed. The thickness at which half of the photons are absorbed is called the *half-value layer* (HVL). In the example, N_0 photons pass through a material. After 1 HVL, one half of photons has been lost; after 2 HVLs, only one fourth of the photons is left. In practice, the attenuation of a beam of photons is usually calculated using the linear attenuation coefficient ($\mu = \ln 2/\text{HVL}$) in the following equation:

$I = I_0 e - \mu^x$.

In this equation, I_0 is the initial beam intensity and I is the intensity after traveling through thickness x. The values of linear attenuation coefficients depend on the energy of the photon and the composition of the material. The denser the material and the higher the energy of the photon, the less attenuation and the lower the value of μ. Linear attenuation coefficients and HVLs for radionuclides and materials of interest to nuclear cardiology are given in Table 2.2

Table 2.2 shows the relationship between the photopeak energy of common radionuclides used in nuclear cardiology and their corresponding linear attenuation coefficient (μ) and HVL in soft tissue, bone, and lead. Note that the denser the material, the smaller the HVL has to be in order to reduce the photon beam by 50%. Figure 2.8 shows interaction of radiation (charged particles) with matter.

		Soft tissue (1.0 g/cm³)		Bone (1.9 g/cm³)		Lead (11.3 g/cm³)	
Radionuclide	Energy, *keV*	μ, *1/cm*	HVL, *cm*	μ, *1/cm*	HVL, *cm*	μ, *1/cm*	HVL, *cm*
Thallium-201	72	0.191	3.62	0.493	1.40	39.1	0.018
Technetium-99m	140	0.153	4.52	0.295	2.35	30.7	0.023

The values in the table were calculated from data obtained from Hubble and Seltzer [4]

Table 2.2 Linear attenuation coefficients (μ) and half-value layers (HVLs)

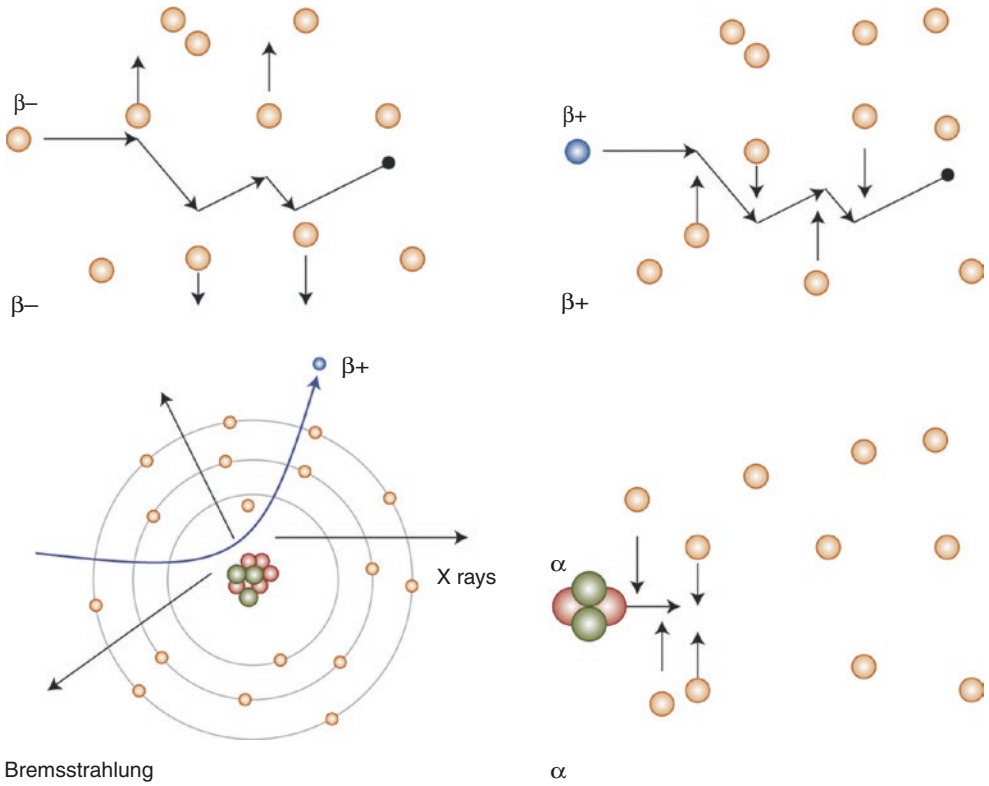

Fig. 2.8 Interaction of radiation with matter: charged particles. High-energy charged particles such as alpha particles (α), beta particles (β), and the photoelectrons and recoil electrons discussed earlier slow down and lose energy as they pass through matter. This loss is a result of the forces their charges exert on the electrons (and, to a lesser extent, on the nuclei) of the material. These interactions are called *collisions*. The loss of energy is termed *collisional losses* (even though it does not actually involve a collision between the two particles) or *radiation losses*, depending on the nature of the encounter

The β particles have the same mass as electrons, and as they pass through material, the electrical forces of the electrons (attractive for β+ and repulsive for β−) cause them to change course with each interaction. These collisions transfer some of the β particles' energy to the orbital electrons, causing them to escape their orbit (the ejected electron is called a delta ray [Δ]) or to be raised to a higher energy state (excitation). Due to their tortuous path, the depth at which β particles will penetrate a material (range) varies between different β particles of the same energy, a process called *straggling*. Two measures of the depth of penetration of beta particles are the extrapolated range (an estimation of the maximum positron penetration) and the average range (the mean penetration). A short positron range is desirable for positron emission tomography (PET) imaging because PET determines the origin of the electron–positron annihilation event, not the actual site of the positron emission. Table 2.3 presents extrapolated and average ranges for several PET radionuclides

The α particles are much more massive than electrons. As collisions occur between α particles and electrons, the electrons are excited or swept from orbit, but the encounter has little effect on the direction of the α particle. As a result, α particles of the same energy all have the same range, with very little straggling. The range is also very small, so that α particles present very little danger as an external radiation source given that they are stopped by a few centimeters of air or a few micrometers of tissue

Table 2.3 shows the relationship between the maximum energy of the emitted positron and the distance range that these particles travel in air and water. Note that the lower the energy and the denser the medium, the less it travels and, thus, the higher the resulting spatial resolution.

		Extrapolated range, *cm*		Average range, *cm*
Radionuclide	Maximum energy, *MeV*	Air	Water	Water
Carbon-11	0.961	302	0.39	0.103
Nitrogen-13	1.19	395	0.51	0.132
Oxygen-15	1.723	617	0.80	0.201
Fluoride-18	0.635	176	0.23	0.064
Rubidium-82	3.35	1280	1.65	0.429

Data from Cherry et al. [5], with permission from Elsevier

Table 2.3 Positron particle range

Formation of Radionuclides

Figures 2.9 and 2.10 illustrate the formation of radionuclides by nuclear reactors and cyclotrons.

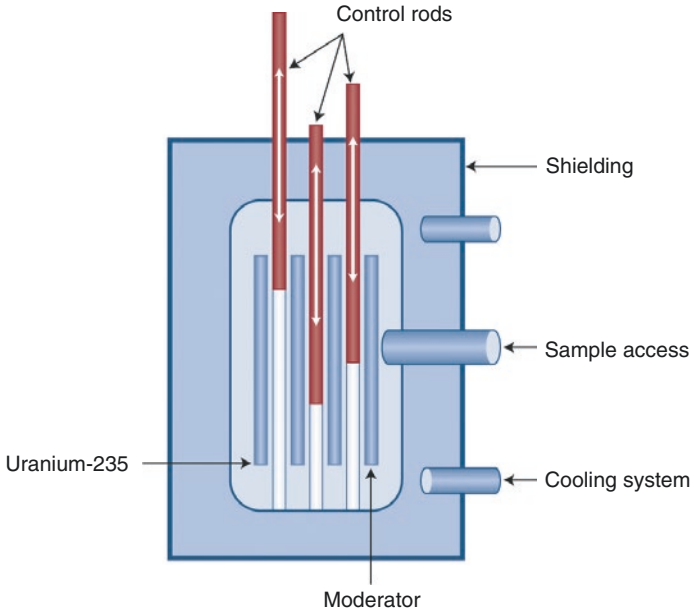

Fig. 2.9 Formation of radionuclides: nuclear reactors. The radionuclides used in nuclear cardiology do not occur naturally and must be manufactured. This may be done by extracting them from the spent fuel of a nuclear reactor, bombarding a target nuclide with high-energy neutrons to make a nuclide that is neutron-rich (too many neutrons to be stable), or bombarding a target with high-energy, positively charged particles, such as protons, using a cyclotron or other particle accelerator to make proton-rich nuclides. Generators are devices that allow the separation of a daughter radionuclide from the parent in a shielded container that may be transported long distances from the manufacturing site (reactor or accelerator)

Nuclear reactors are an important source of radionuclides for nuclear medicine, including iodine-131 and xenon-133. Most importantly, molybdenum-99 (^{99}Mo), the parent of technetium-99m, is produced in a nuclear reactor. The heart of a nuclear reactor is a core of fissionable material (usually uranium-235 [^{235}U] and ^{238}U). Fission splits the uranium nucleus into two lighter nuclei and produces two or three fission neutrons. Some of these neutrons strike other uranium nuclei, converting them to ^{236}U; this quickly undergoes fission and produces many more fission neutrons, which stimulate even more fission events. The uranium in the core is surrounded by a moderator ("heavy water" and graphite) that slows down the fission neutrons to an energy that is more likely to produce further reactions. The ensuing nuclear chain reaction is regulated by control rods made of boron or cadmium, which absorb neutrons. Fission products usually have an excess of neutrons and decay further with emission. More than 100 nuclides are created in the fission process. These fragments can be extracted by chemical means from material removed from the core. Another way to use a nuclear reactor to produce radionuclides, neutron activation, is to place a target into the high-neutron flux of the core while keeping it isolated from the core itself. ^{99}Mo can be produced by either process, but most is extracted as a fission fragment

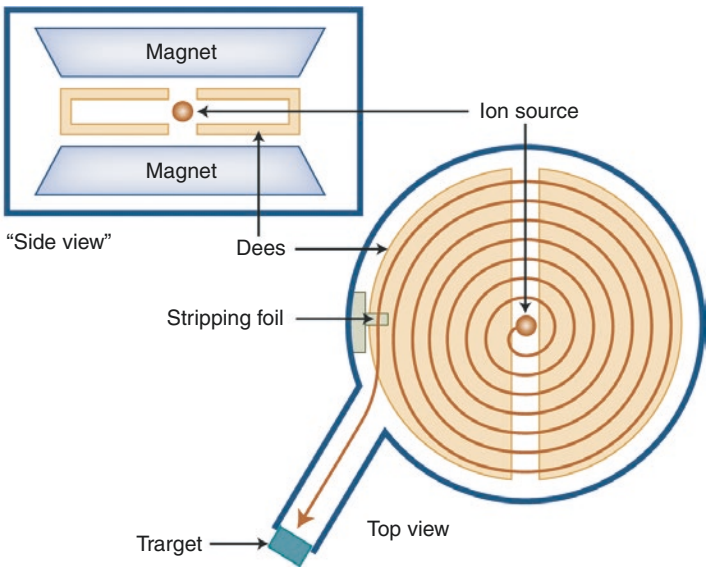

Fig. 2.10 Formation of radionuclides: cyclotrons. Cyclotrons are charged particle accelerators that are used to produce radionuclides by bombarding a target with particles or ions that have been accelerated to high rates of speed. The two basic components of a cyclotron are a large electromagnet and semicircular, hollow electrodes called "dees" because of their shape. Ions are injected into the center of the device between the dees. An alternating current applied to the dees causes the ions to be attracted to one side. Once inside the dee, the ion will travel in a curve because any charged particle moving in a magnetic field (supplied by the electromagnet) moves in a circular path. Although there is no electric field inside the dee, the current is carefully timed so that the polarization of the dees changes as the particles emerge from one side. This accelerates the ions, and their arc of travel becomes larger as they move faster and faster, picking up speed each time they cross the gap between the dees. At the maximum radius, the ions are deflected out of the cyclotron and strike a target, creating new nuclides. An example of this is the use of a cyclotron to bombard an oxygen-18 target with protons, resulting in conversion of the nucleus to fluorine-18 (after the emission of a neutron). Several cyclotron-produced radionuclides used in nuclear cardiology are listed in Table 2.4

Positive-ion cyclotrons accelerate α particles or protons and use an electrostatic deflector to direct the ion beam to the target. Negative-ion cyclotrons, as shown in this figure, accelerate negative hydrogen (H^-) ions, a proton with two electrons. A stripping foil, made of carbon, strips off the two electrons from the ion, leaving a proton. The positive charge of the proton causes it to arch in the opposite direction, which in turn causes the beam to exit the cyclotron and strike the target. Most hospital-based and community-based cyclotrons are negative-ion cyclotrons because they require less shielding and are more compact than positive-ion cyclotrons

Table 2.4 compares the energy of the radiation, half-lives, and modes of production of SPECT radionuclides versus PET radionuclides commonly used in nuclear cardiology procedures. Note that because of the short half-life of most cyclotron-produced PET tracers, a cyclotron must be located nearby. Only fluorine-18 is routinely distributed commercially [6].

Common SPECT radionuclides				
Radionuclide	*Production*	*Decay*	*Emission, keV*	*Half-life*
Iodine-123	Cyclotron	Electron capture	159 (γ-ray)	13.21 hr
Thallium-201	Cyclotron	Electron capture	68–80 x-ray 167 (10%; γ-ray)	73 hr
Technetium-99m	Generator	Internal transition	140 (γ-ray)	6 hr
Common PET radionuclides				
Radionuclide	*Production*		*Positron energy, keV*	*Half-life*
Oxygen-15	Cyclotron		735	122 sec
Nitrogen-13	Cyclotron		491	9.96 min
Carbon-11	Cyclotron		385	20.3 min
Fluoride-18	Cyclotron		248	110 min
Rubidium-82	Generator		1523	1.3 min

Table 2.4 Common radionuclides for use in nuclear cardiology

Figure 2.11 illustrates some types of generators important in preparing radionuclides for use in nuclear medicine.

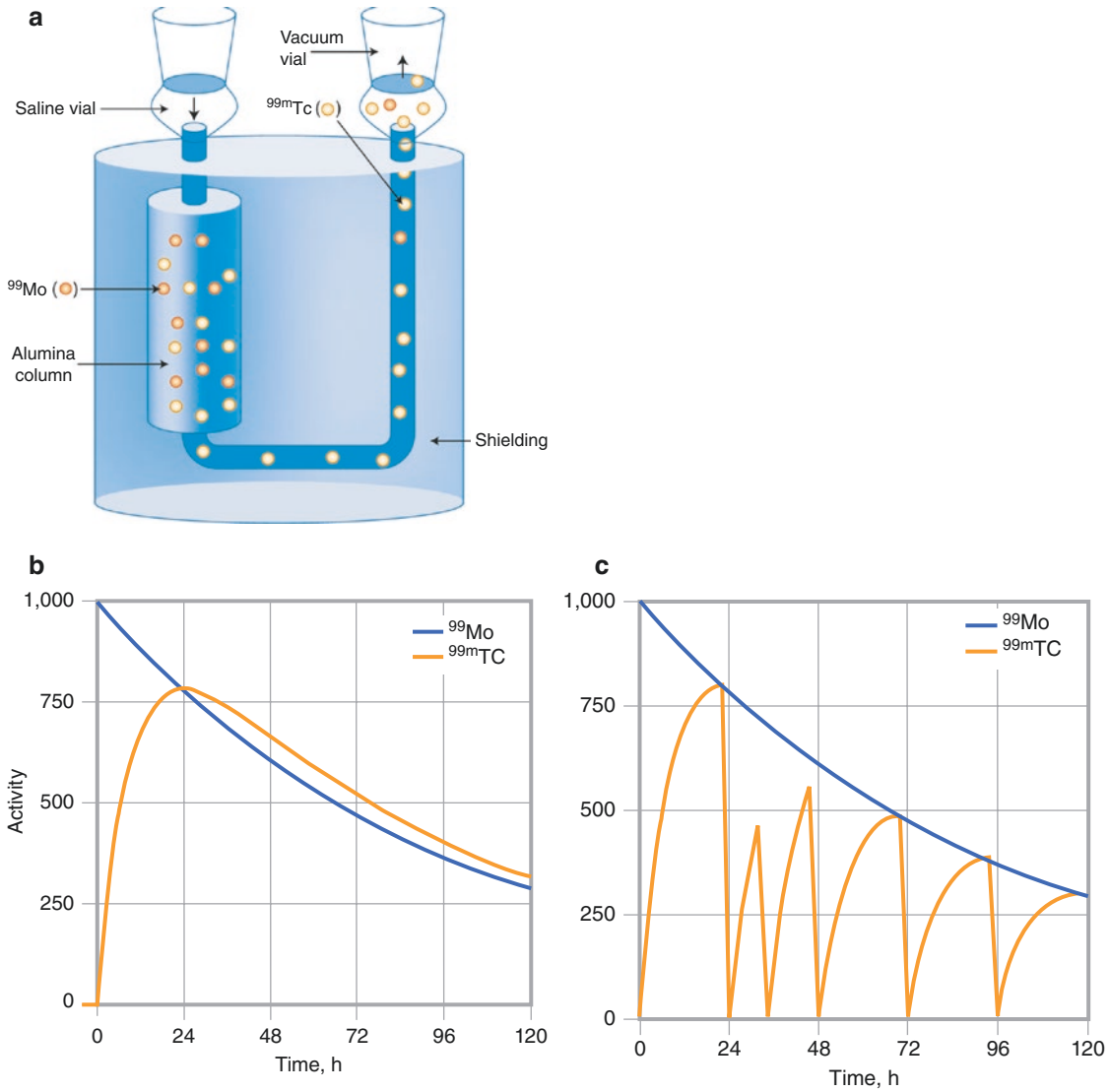

Fig. 2.11 Formation of radionuclides: molybdenum-99–technetium-99m (^{99}Mo–^{99m}Tc) generator. Generators are devices that allow the separation of a radionuclide from a relatively long-lived parent, allowing the production of short-lived radionuclides at a location remote from a reactor or cyclotron (such as a hospital, clinic, or local radiopharmacy). The daughter is continuously replenished by the parent inside the generator, which shields both radionuclides while allowing the daughter to be extracted repeatedly [7]

(**a**) The most common generator used in nuclear medicine is the ^{99}Mo-^{99m}Tc generator, which produces ^{99m}Tc (half-life [t½], 6 h) from the β decay of ^{99}Mo (t½, 66 h). The ^{99}Mo is produced in a nuclear reactor. The heart of the generator is a porous column of alumina impregnated with ^{99}Mo. A vacuum vial is used to pull saline out of a second vial through the porous column. Technetium (both ^{99m}Tc and ^{99}Tc) is washed out of the column by the saline and is collected in a vacuum vial, leaving the ^{99}Mo behind. The generator must be well shielded because ^{99}Mo emits both β particles and 740–780-keV γ-rays. The process of extracting ^{99m}Tc from the generator is called *milking* or *elution*, and the extracted ^{99}Tc-saline solution is called *eluate*. After milking, the ^{99m}Tc solution must be tested for ^{99}Mo and aluminum. ^{99}Mo is detected by using a dose calibrator and a shield that blocks the low-energy photon from ^{99m}Tc. The maximum amount of ^{99}Mo allowed under Nuclear Regulatory Commission regulations is 0.15 Bq ^{99}Mo per kilobecquerel (kBq) ^{99m}Tc (0.15 Ci ^{99}Mo per millicurie ^{99m}Tc). Aluminum is detected chemically, with a maximum permissible level of 10 μg/mL of eluate

(**b**) The ^{99m}Tc is produced by the β decay of ^{99}Mo in the alumina column if the generator is undisturbed. This process is an example of transient equilibrium, in which the parent's half-life is somewhat longer than the daughter's half-life. After a few hours, the daughter activity is almost equal (actually slightly higher) to the parent activity

(**c**) Activity in the generator with repeated milkings is shown. Fortunately, the optimal frequency for milking the generator is at intervals slightly less than 24 h. The dip at 32 h shows that if the generator is milked, the process of ^{99m}Tc buildup begins again (and, in this case, results in only slightly less activity at the next regular milking). ^{99}Mo-^{99m}Tc generators are designed to last at least 2 weeks in the nuclear pharmacy

Another generator of importance to nuclear cardiology is the strontium-82 (^{82}Sr)–rubidium-82 (^{82}Rb) generator. ^{82}Rb (t½ = 1.3 min) is produced by a β decay of ^{82}Sr (t½ = 25 day, manufactured using an accelerator). The daughter activity equals the parent activity very soon after elution and allows elution every hour. This is an example of secular equilibrium in which the parent's half-life is a great deal longer than the daughter's half-life. The short half-life of ^{82}Rb makes it impractical to transport the dose to the patient. The generator is designed to deliver the dose directly into an intravenous line. ^{82}Rb generators are designed to last about 1 month in the clinic. ^{82}Sr and ^{85}Sr may be low-level contaminants and are found in routine quality control by assaying the eluent after complete decay of the ^{82}Rb

Imaging Devices and Principles

Devices and principles of nuclear cardiology imaging are shown in Figs. 2.12, 2.12, 2.13, 2.14, 2.15, 2.16, 2.17, 2.18, 2.19, 2.20, 2.21, 2.22, 2.23, 2.24, 2.25, 2.26, 2.27, 2.28, 2.29, 2.30, 2.31, 2.32, 2.33, 2.34, 2.35, 2.36, 2.37, 2.38, and 2.39.

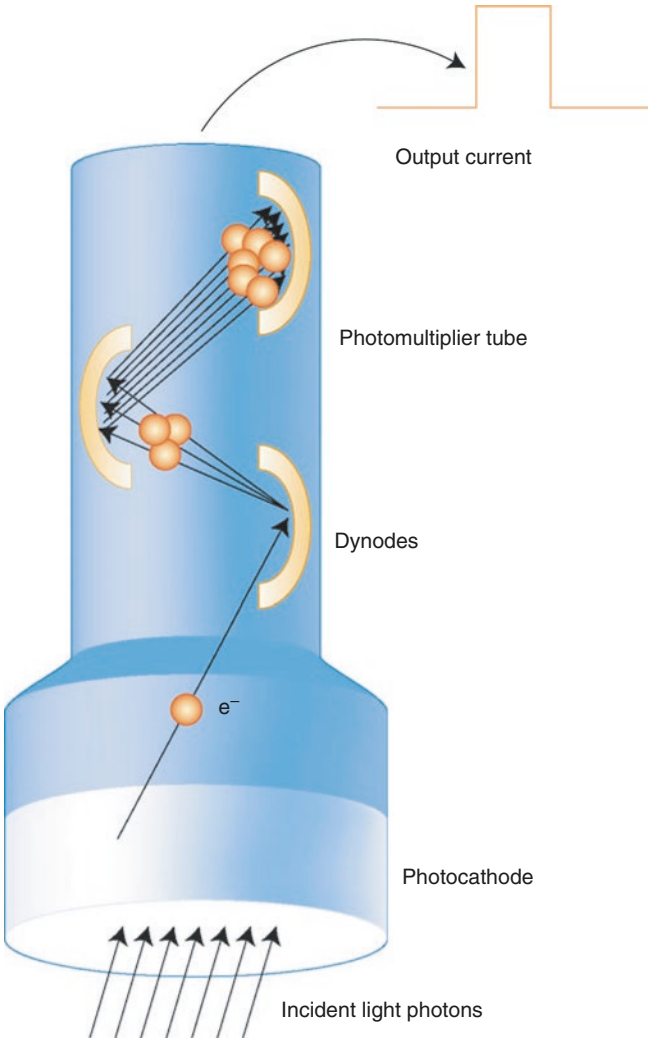

Fig. 2.12 Operation of photomultiplier tubes (*PMTs*). PMTs convert energy from visible light into an electric signal. Light interacting with the material in the photocathode causes it to release electrons, which are accelerated along the tube by a high-voltage differential. As the electrons travel through the tube, they strike metal electrodes called *dynodes*, at which point even more electrons are ejected. This cascade of multiplication continues until the electrons are output as a current at the other end. The voltage (height) of the pulse generated by the PMT is directly proportional to the amount of visible light that strikes the photocathode

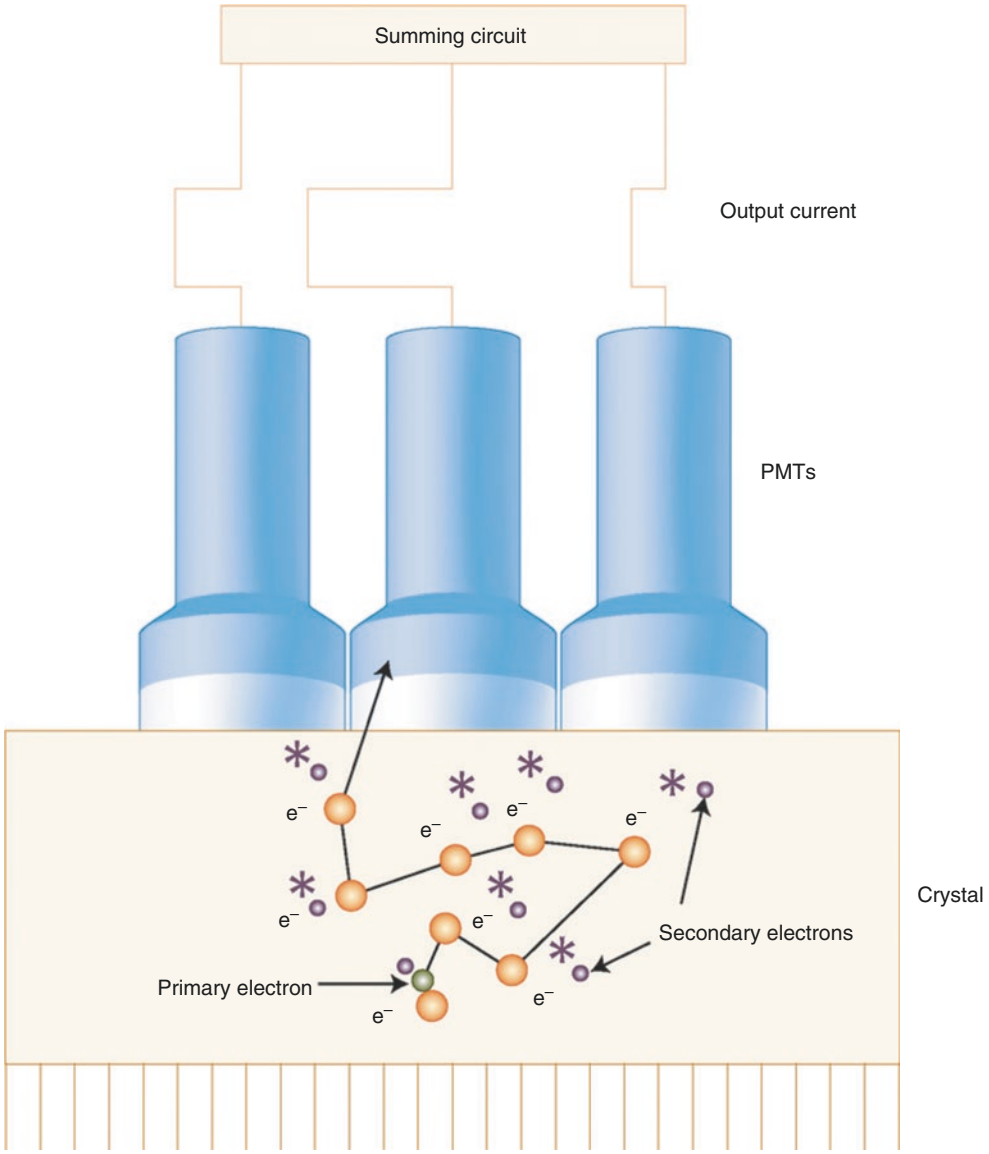

Fig. 2.13 Operation of the crystal. The crystal is used to convert γ-rays into visible light. A γ-ray travels through the collimator and interacts with one of the atoms in the crystal, ejecting an electron (called the primary electron) through the photoelectric effect. This ejected electron continues traveling through the crystal and excites a large number of secondary electrons, which lose their excitation energy by emitting visible light. The glow of the scintillation is converted into electrical signals by the PMTs. The location of the scintillation event is determined by the positioning circuitry based on the relative signals from the different PMTs. The brightness of the scintillation is proportional to the energy of the photon, measured by the pulse height analyzer

Note that the γ-ray travels some distance through the crystal before it interacts with a crystal atom. If the crystal is very thin, a γ-ray may travel through the entire width of the crystal with no interaction. Therefore, a thicker crystal results in a higher sensitivity for the detection of γ-rays. Conversely, note that the primary electron travels in an irregular path and may excite atoms far away from its point of origin. The thicker the crystal is, the farther the electron may travel before it exits the crystal. Thus, a thick crystal implies that the scintillation may be more spread out, which essentially reduces the resolution of the detector. So, just as with collimators (*see* Fig. 2.16), there is a trade-off between sensitivity and resolution with the size and shape of the crystal

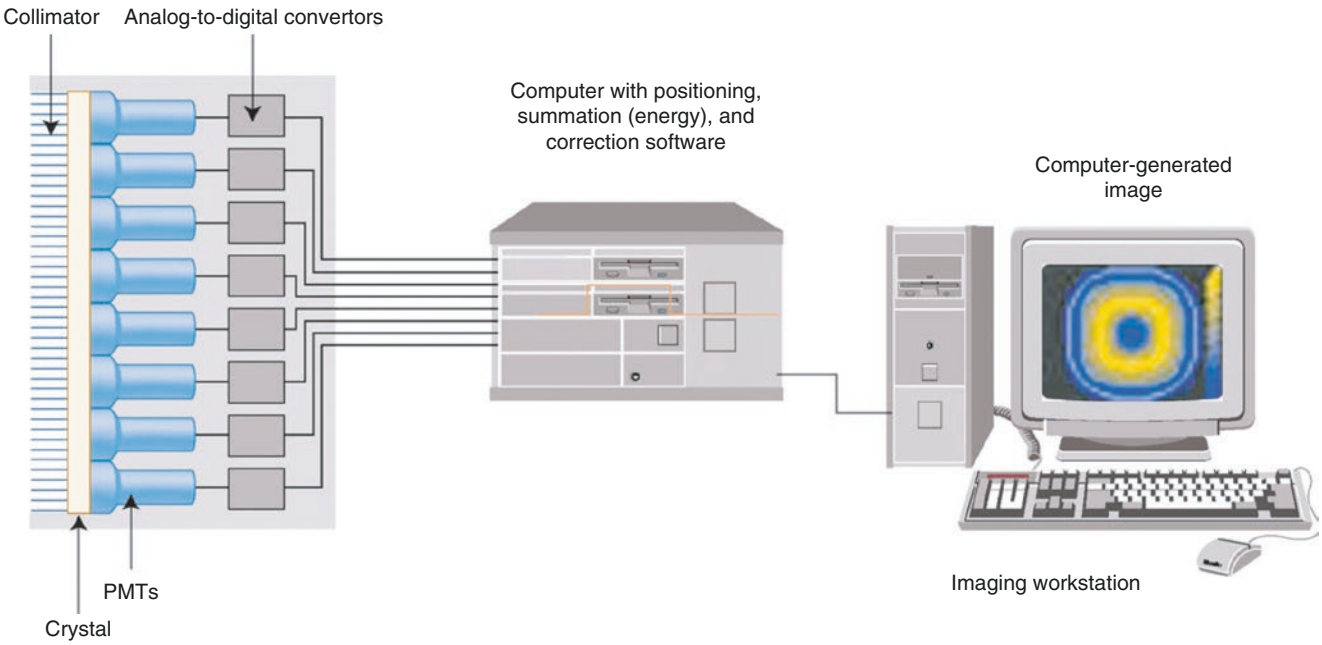

Fig. 2.14 Digital scintillation camera. The main components of SPECT systems are the scintillation camera, the gantry (the frame that supports and moves the heads), and the computer systems (hardware and software). These components work together to acquire and reconstruct the tomographic images

The basic components of a scintillation camera are a collimator, a sodium iodide crystal, PMTs, and an analog or digital computer designed to determine the location and energy of a photon striking the crystal. γ-Rays (photons) pass through the collimator and cause a scintillation event (a short burst of visible light) to occur in the crystal. The glow of the scintillation is converted into electrical signals by the PMTs. The location of the scintillation event is determined based on the relative signals from the different PMTs. The brightness of the scintillation is proportional to the energy of the photon. Scintillation cameras were developed in the late 1950s and early 1960s. These cameras used pulse height analyzers and spatial positioning circuitry invented by Hal Anger of the University of California at Berkeley to determine the location and energy of the incident photon [8]. Early cameras were completely analog devices in which the output was sent to an oscilloscope, creating a flash on the screen. A lens focused the screen on a piece of radiographic film that was exposed, one flash at a time. This allowed for planar imaging, but for SPECT the images must be made available to the computer digitally

Today, camera systems convert the position and pulse height signals generated from analog circuitry in the camera to digital signals using analog-to-digital converters. The signals may then be further corrected for energy and position through digital processing. Camera designs that convert the output of each PMT to a digital signal, as shown here, have become common. The computer may then perform all of the positioning and pulse height analyses without the need for complicated analog circuitry. This results in greater processing flexibility, greater spatial resolution, and higher count rates

Another step in the digitization of scintillation cameras is the replacement of PMTs with solid-state detectors called *photodiodes*. One camera with this design uses individual cesium iodide (CsI) scintillation crystals, each backed with a silicon photodiode. Each CsI crystal is 3 mm^2, giving a resolution similar to that of a conventional camera without the need for positioning circuitry. Eliminating the PMTs greatly reduces the size and weight of the scintillation camera, with some trade-offs in cost and energy resolution. These types of cameras are usually known as solid-state cameras

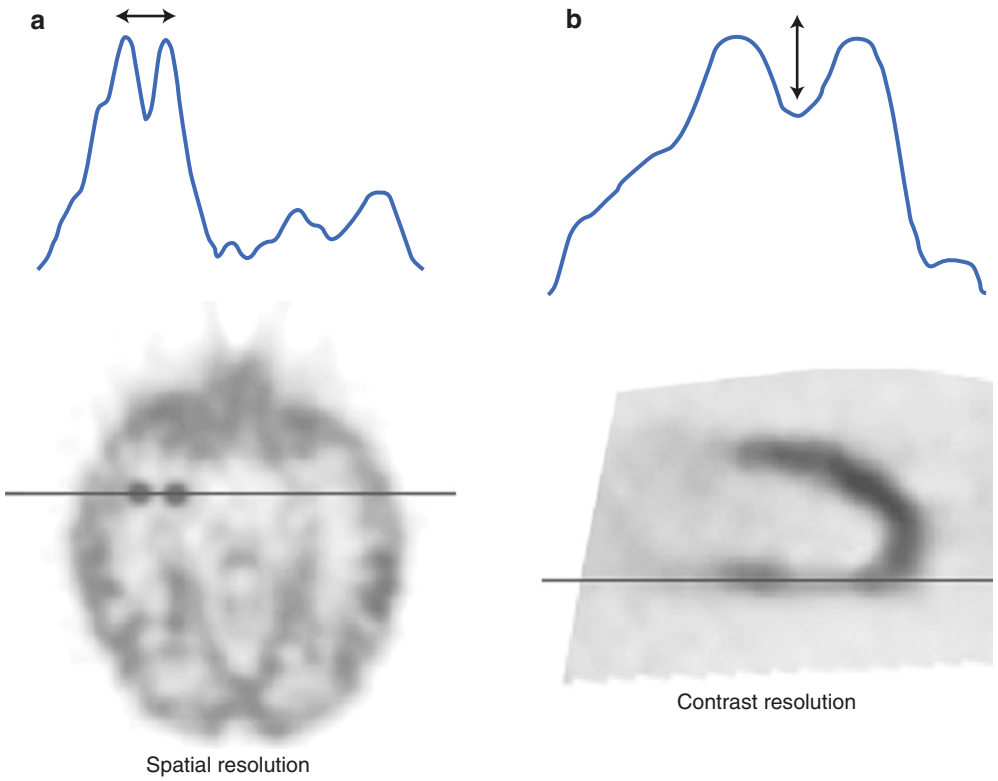

Fig. 2.15 Principle of spatial and contrast resolution. The most common measurements of image quality are spatial resolution and contrast resolution. *Spatial resolution* refers to how well objects can be separated in space (as opposed to blurring them together), and *contrast* refers to how well different levels of brightness (representing radionuclide concentration in a scintigram) can be discriminated

Spatial resolution is the measure of how close two point sources of activity can come together and still be distinguished as separate. Because no medical imaging modality is perfect, a point source never appears as a single bright pixel but instead as a blurred distribution. Two blurry points eventually smear together into a single spot when they are moved close enough to each other. Resolution is measured by taking a profile (a graph of counts encountered along a line drawn through a region of interest in the image) through a point source and analyzing the resulting curve. A profile through a perfect point source would look like a sharp single spike rising above the flat background. A profile through a real point source appears as a Gaussian-shaped curve; this curve is called the *point spread function*. (**a**) When the two Gaussian curves of two point sources get close enough together, they cannot be distinguished as separate. This distance is a measure of image resolution. Two brain tumors are imaged and a profile is taken through the resulting reconstruction. As the tumors move closer together, the discrete peaks of the profile start to merge into a single peak

Contrast resolution in nuclear cardiology images can be defined as the measure of counts (or intensity) in the target (the object we are trying to image) compared with the intensity in a background region. High counts in the target increase contrast; high counts in the background region (e.g., lung uptake) decrease contrast. Low contrast can make the target fade into the background. (**b**) Contrast is also easily measured using a profile. This figure shows a count profile taken through a decreased area of a myocardial perfusion image. In this case, the "target" counts are those in the perfusion abnormality, and the "background" counts are those in the normal myocardium. The depth of the valley in the profile, compared with the overall height of the rest of the curve, is a measure of contrast

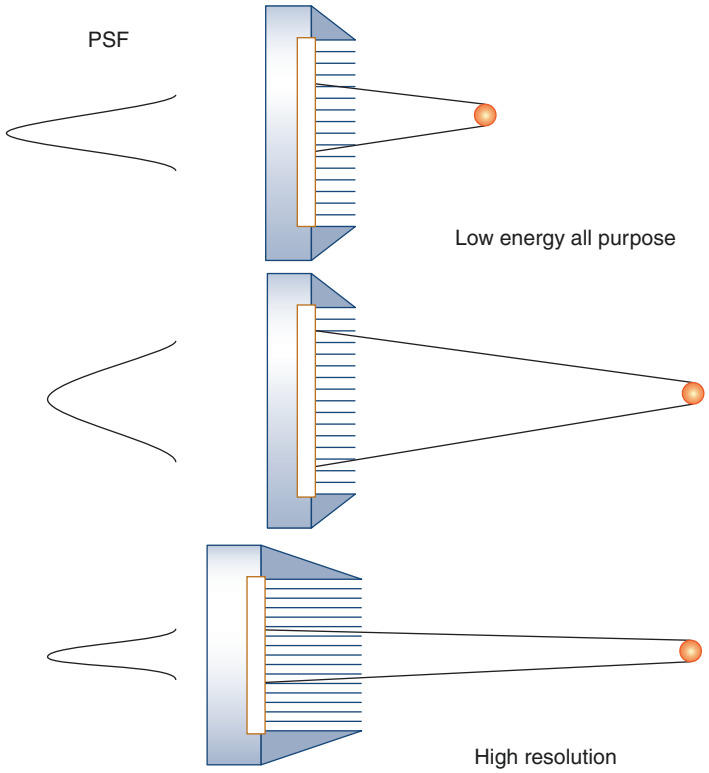

Fig. 2.16 Principle of collimation. Because γ-rays are emitted from a source uniformly in all directions, a photon from any area of the body can theoretically strike any area of the detector. Instrumentation is needed to determine the directions of the photon's emissions in order to be able to localize the source. This process is called *collimation*. For nuclear cardiology, collimators generally consist of an array of long, narrow (usually) parallel holes that exclude all photons except those that travel parallel to the direction of the hole. Collimators are rated by their sensitivity and resolution. *Resolution* is defined in Fig. 2.15; *sensitivity* is the number of photons that travels through the collimator in a certain amount of time (as a fraction of photons emitted from the source)—that is, counts per second or counts per minute. In this instance, image resolution is affected by collimation because some photons not traveling in exactly a parallel path get through the collimator holes. Thus, a single point source will appear fuzzy on the detector. How much the point "spreads out"—the width of its point spread function (PSF)—is related to the spatial resolution and depends on the length and width of the holes. More specifically, spatial resolution is given by the full width of the PSF as half its maximum. Low-energy all-purpose (LEAP) and general-purpose collimators have relatively short, wide holes that accept more photons than do high-resolution collimators with long, narrow, and/or smaller holes. Increasing the length of the hole increases resolution by decreasing the angle subtended by the hole and thus eliminates more γ-rays traveling at angles not parallel to the hole. Thus, a higher resolution is achieved at the cost of sensitivity. In general, the sensitivity and resolution of a collimator are inversely related. A very high-sensitivity collimator will have low resolution, and a very high-resolution collimator will have low sensitivity. Here, the PSFs for differently shaped collimators are shown at the *left* of the figure. Note that the width of the PSF curve is broader for LEAP collimators, indicating a lower resolution, but the total area underneath this PSF curve is higher than that of the high-resolution collimator, indicating higher sensitivity. This figure also demonstrates that the resolution of the image, as seen by the PSF curves on the *left*, depends on the distance between the source and the collimator. This is discussed in more detail in Fig. 2.17

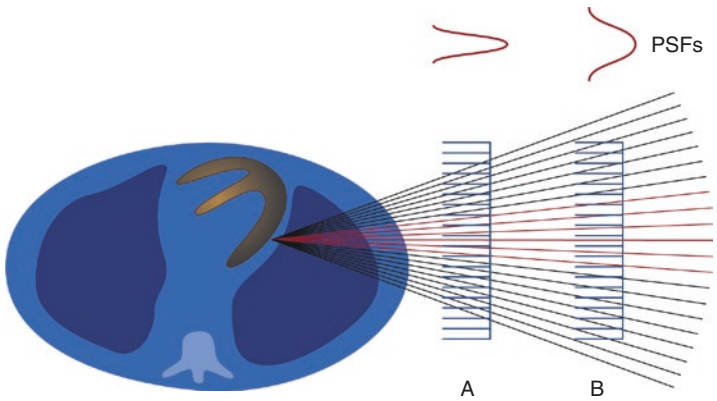

Fig. 2.17 Resolution versus sensitivity. In air, recall that the amount of radiation from a point source falling on a plane decreases as $1/r^2$. However, if a collimator is placed between the source and the detector, this relationship no longer holds. The same number of γ-rays will travel through the collimator, no matter how far the source is from the detector, because γ-rays that travel too obliquely from the line of the collimator holes will not pass through any collimator, no matter how close it is to the source. However, a ray that is near enough to being parallel to a collimator hole will be able to pass through a collimator, no matter how distant it is from the source. The primary difference between a collimator placed near the source and one placed far away from the source is which collimator hole a γ-ray will pass through

A γ-ray traveling exactly parallel to the collimator will pass through the hole that is directly "aimed" at the source. If the γ-ray is slightly oblique to the collimator, it may pass through a hole not exactly in line with the source. How far away that hole is from the "correct" hole depends on how far the source is from the collimator. In this figure, notice that when the collimator is close to the source (*A*), most of the γ-rays travel through the collimator holes that are nearly in line with that source, even when those γ-rays are slightly oblique to the holes. However, if the detector is far away from the source (*B*), the same number of γ-rays travels through the collimator but more of the oblique rays travel through holes farther away from the one directly in line with the source. This causes a blurring or loss of resolution, which is seen in the PSFs shown for each of the collimator positions at the *top* of the figure. Note that the farther away the detector is from the source, the lower and more spread out the PSF. However, the area underneath these curves does not change. Therefore, the number of photons detected stays the same with collimator-source distance, but the image resolution decreases as the distance increases. This resolution decrease with source-to-detector distance is termed the *detector response* or *geometric response*

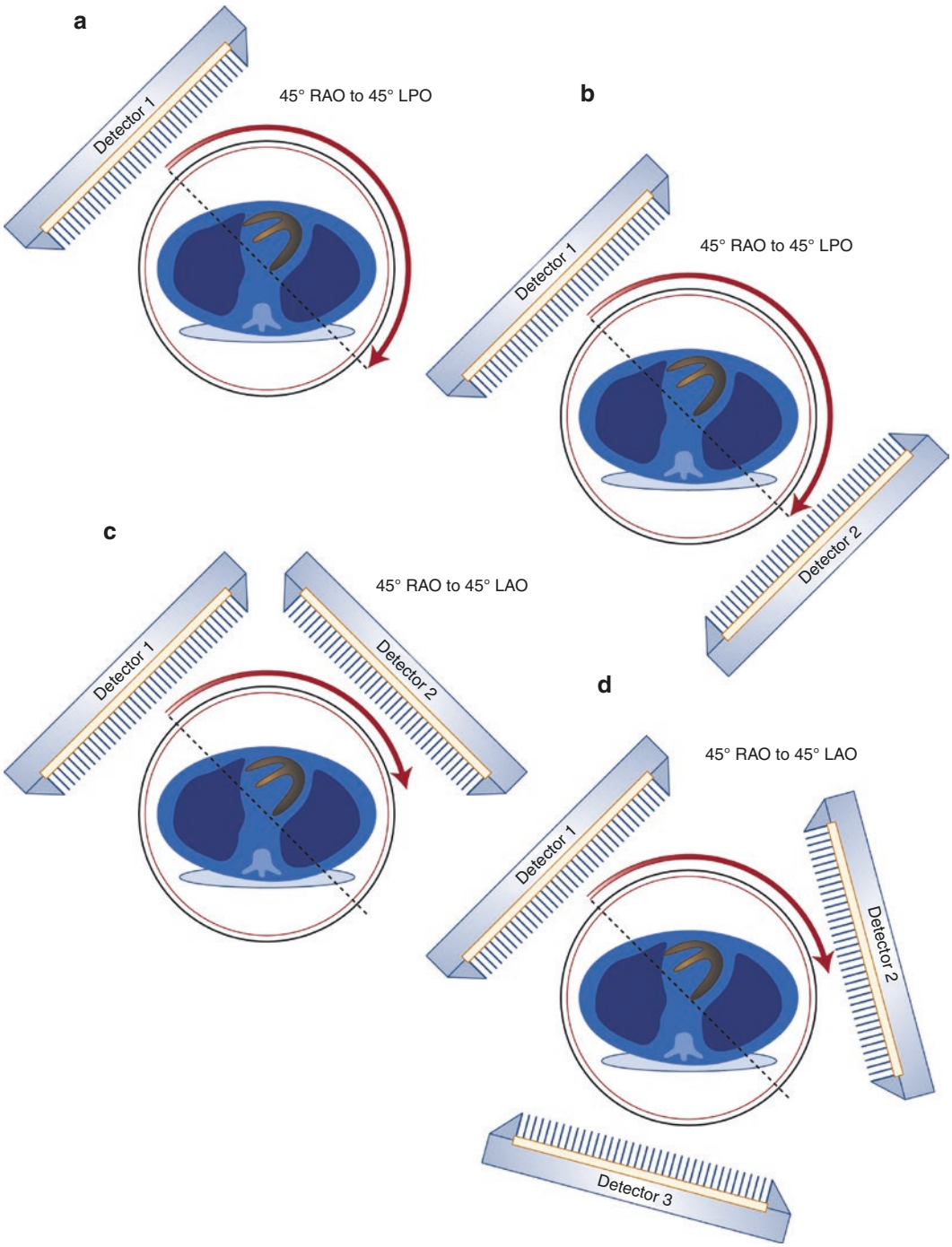

Fig. 2.18 SPECT cameras: multiheaded cameras. Multidetector SPECT systems have more than one scintillation camera attached to the gantry. (**a**) The most obvious benefit of adding more detectors to a scintillation camera system is the increase in sensitivity. Doubling the number of heads doubles the number of photons that may be acquired in the same amount of time. The user may take advantage of the increase in sensitivity by acquiring more counts, adding higher-resolution collimation, or increasing throughput. (**b**) This figure shows two large field-of-view rectangular cameras mounted opposite each other, 180° apart. This configuration may speed 360° SPECT imaging by halving the imaging time while collecting the same number of counts, because a full 360° of projections can be acquired by rotating the gantry 180°. (**c**) For cardiac SPECT, in which a 180° orbit is recommended, SPECT systems with two detectors mounted next to each other (at 90°) on the gantry allow a full 180° orbit to be acquired while only rotating the gantry through 90°. (**d**) Triple detector cameras are usually dedicated to SPECT imaging. The three heads, as discussed for double-headed systems, will result in increased sensitivity that may be used to increase throughput, counts, or resolution. If the three detectors are mounted rigidly 120° from one another, however, the system must rotate through 120° to obtain 180° of data. Thus, these systems also do not have a great impact on cardiac imaging with 180° orbits

For any multiheaded system, the primary advantage is increase in throughput, because the acquisition will take less time. However, the gain in sensitivity may be traded to give more precise images by allowing the use of higher-resolution collimators

Drawbacks of multiple-headed cameras include an increase in quality control required by the addition of the additional heads and some loss of flexibility. Double-detector systems do not allow the same flexibility of movement that is enjoyed with many single-headed systems. They may not be easily used for some types of planar imaging (e.g., gated blood pool), in which it is often difficult to position the camera correctly. One unique SPECT system acquires planar projections by rotating the patient in an upright position while the camera(s) remain(s) fixed. LAO left anterior oblique, LPO left posterior oblique, RAO right anterior oblique

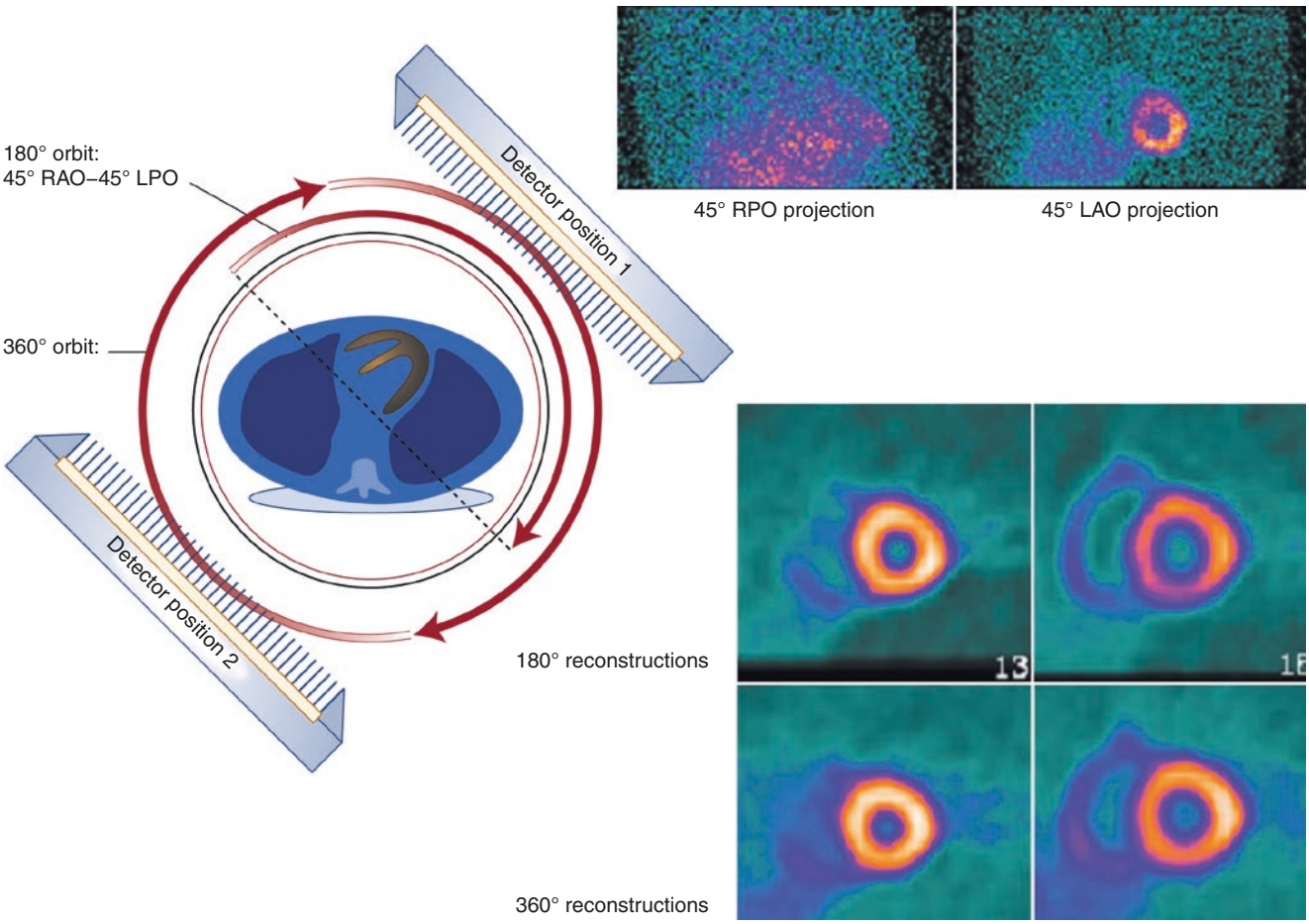

Fig. 2.19 SPECT cameras: 180° versus 360° data acquisition. Although 360° orbits are generally preferred for body SPECT, 180° orbits may be better for cardiac SPECT. The heart is located forward and to one side of the center of the thorax, resulting in a great deal of attenuation when the camera is behind the patient. The angles chosen for the 180° orbit are those closest to the heart, from the 45° right anterior oblique (*RAO*) to the 45° left posterior oblique (*LPO*). These projections are those that suffer least from attenuation, scatter, and detector response because they are the ones that get the camera head as close as possible to the heart. Projections taken from the posterior aspect of the body are generally noisier and of lower resolution than those taken from the anterior angles. This is easily seen by comparing the 45° left anterior oblique (*LAO*) projection shown here to the 45° right posterior oblique (*RPO*) projection. Reconstructions from 180° acquisitions have higher resolution and contrast than those from 360° acquisitions; this is particularly true for thallium-201 images [9–11]. However, because 180° reconstructions are not truly complete (i.e., new information is available from the other 180° of projections), occasional artifacts seen with 180° reconstructions can be avoided with 360° reconstructions. In particular, 360° reconstructions are generally more uniform than 180° reconstructions. Both of these effects can be seen on the reconstructions on the *bottom right* of this figure

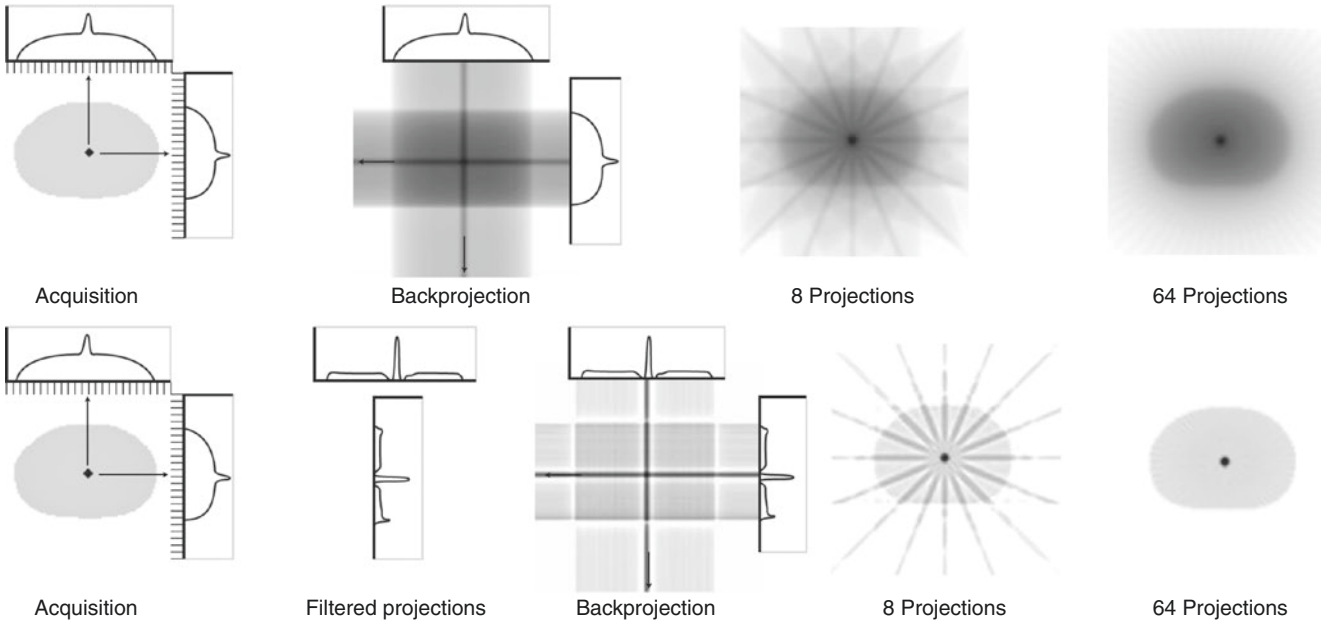

Fig. 2.20 Principle of filtered backprojection reconstruction. Filtered backprojection is an analytic method of image reconstruction. Filtered backprojection, as its name implies, is a combination of filtering and backprojection. The principle of backprojection is shown in the *top row*. When a projection image is acquired, each row of the projection contains counts that emanate from the entire transverse plane. When projection images are obtained from many angles about the body, enough information is available in each row of the set of angular projections to reconstruct the original corresponding transverse slice. Backprojection assigns the values in the projection to all points along the line of acquisition through the image plane from which they were acquired. This operation is repeated for all pixels and all angles, adding the new values with the previous, in what is termed a *superposition operation*. As the number of angles increases, the backprojection improves

Although simple backprojection is useful for illustrative purposes, it is never used in practice without the step of filtering. Note that the backprojection from the top row is quite blurred compared with the original distribution from which it was created. Also, the reconstructions created from eight projections show instances of the "star artifact," which consists of radial lines near the edges of the object. This artifact is a natural result of backprojection applied without filtering. In clinical practice, the projections are filtered prior to backprojection; filtered backprojection is shown in the *bottom row*. After the projections are acquired, a ramp filter is applied to each of them prior to backprojection. Ramp filters are discussed in more detail in Fig. 2.21. The ramp-filtered projections are characterized by enhancement of edge information and the introduction of negative values (or lobes) into the filtered projections. During the backprojection process, these negative values cancel portions of the other angular contributions and, in effect, help to eliminate the star artifact and the blurring seen in the unfiltered backprojection. However, enough projections must be acquired to ensure that proper cancellation is obtained. Radial blurring or streaking toward the periphery of the image often indicates that too few projections were acquired. Finally, a noise-reducing filter such as a Butterworth or Hanning filter is usually applied before, during, or after the backprojection operation. Such filters are discussed in more detail in Fig. 2.21

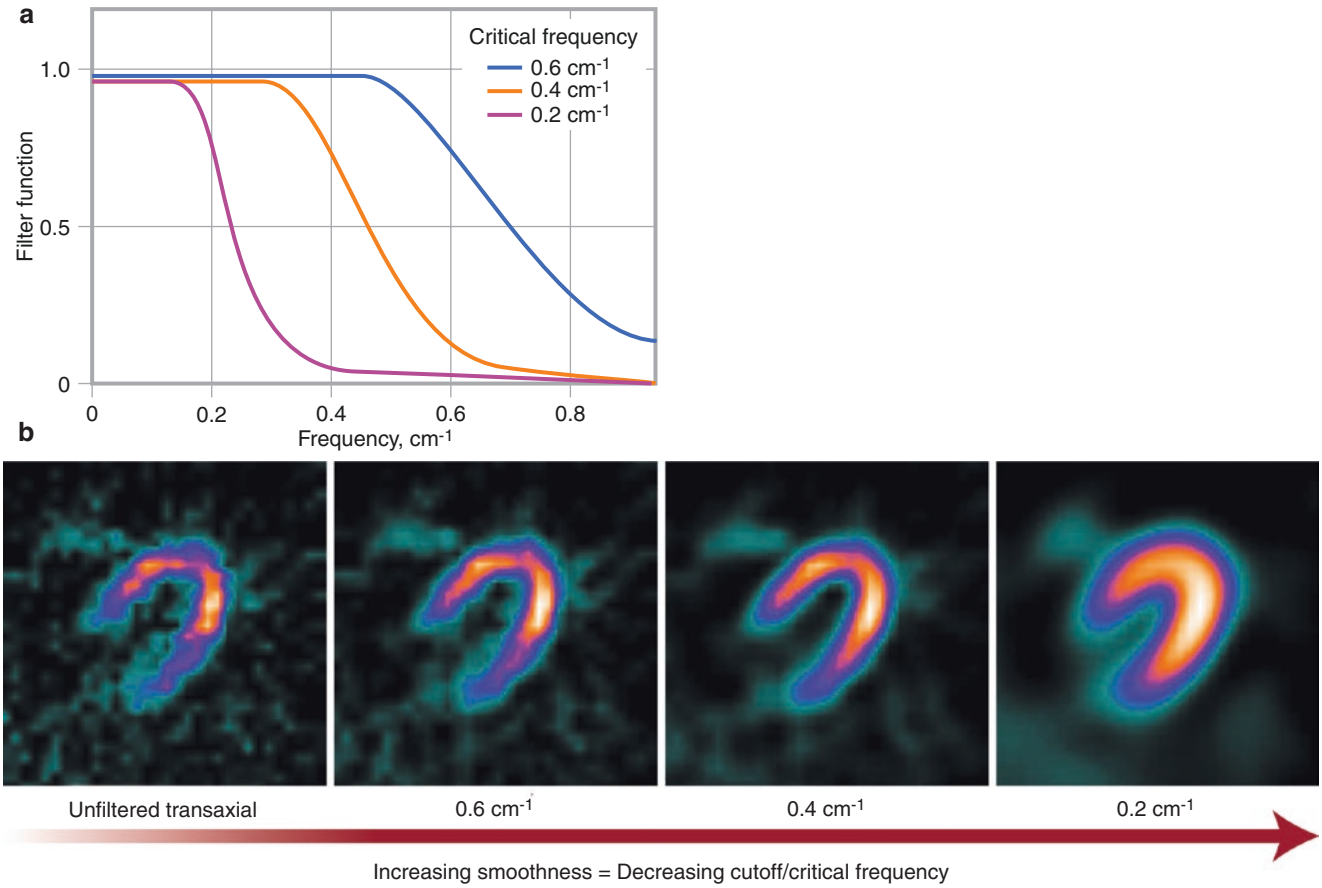

Fig. 2.21 Image filtering. Filtering is the process by which images are smoothed, sharpened, reduced in noise, or used in reconstruction, such as the ramp filter in filtered backprojection. Filtering digital images is accomplished by transforming the images from the spatial domains that are used to frequency space [12, 13]. This transformation is usually performed using a mathematical process called a *Fourier transform*. This transform represents images in terms of cycles per centimeter or variations of counts over distance. In this representation, smaller objects, edges of objects that abruptly change in counts, and image noise are all associated with high frequencies. Larger, smooth organs are associated with lower frequencies. A filter works by defining a curve that specifies how much of each frequency should be modified. If the filter value is 1 at a specific frequency, then it is not modified; if it is less than 1, it is reduced by that amount; and if it is more than 1, it is enhanced by that amount

Because the filtered backprojection reconstruction process uses a ramp filter that enhances image noise, smoothing must be applied to the reconstructed images to reduce the image noise. The most common filters used for smoothing cardiac perfusion images are the Hanning and Butterworth filters. Both these filters are known as *low-pass filters* because they tend to leave the lower frequencies alone while reducing the higher frequencies. The Butterworth filter is defined by two parameters: the critical frequency and the order of the filter. The critical frequency is used to define when the filter begins to drop to zero (known as the *cutoff frequency* for a Hanning filter). The order of the filter determines the steepness of the function's downward slope

(**a**) The *color curves* are three examples of critical frequencies for the Butterworth filter. (**b**) The four transaxial cardiac images are examples of that same transaxial image with the various critical frequencies of the Butterworth filter applied. The leftmost transaxial image has had the gray filter applied. Note that the gray filter is 1 for every frequency; thus, no smoothing is performed. This is the original noisy image that results from the filtered backprojection process. The next image has had the purple filter applied, with a critical frequency of 0.6 cycles/cm. This image appears slightly smoother than the one with no smoothing. As the other two filters are applied with increasingly lower critical frequencies, the image becomes smoother

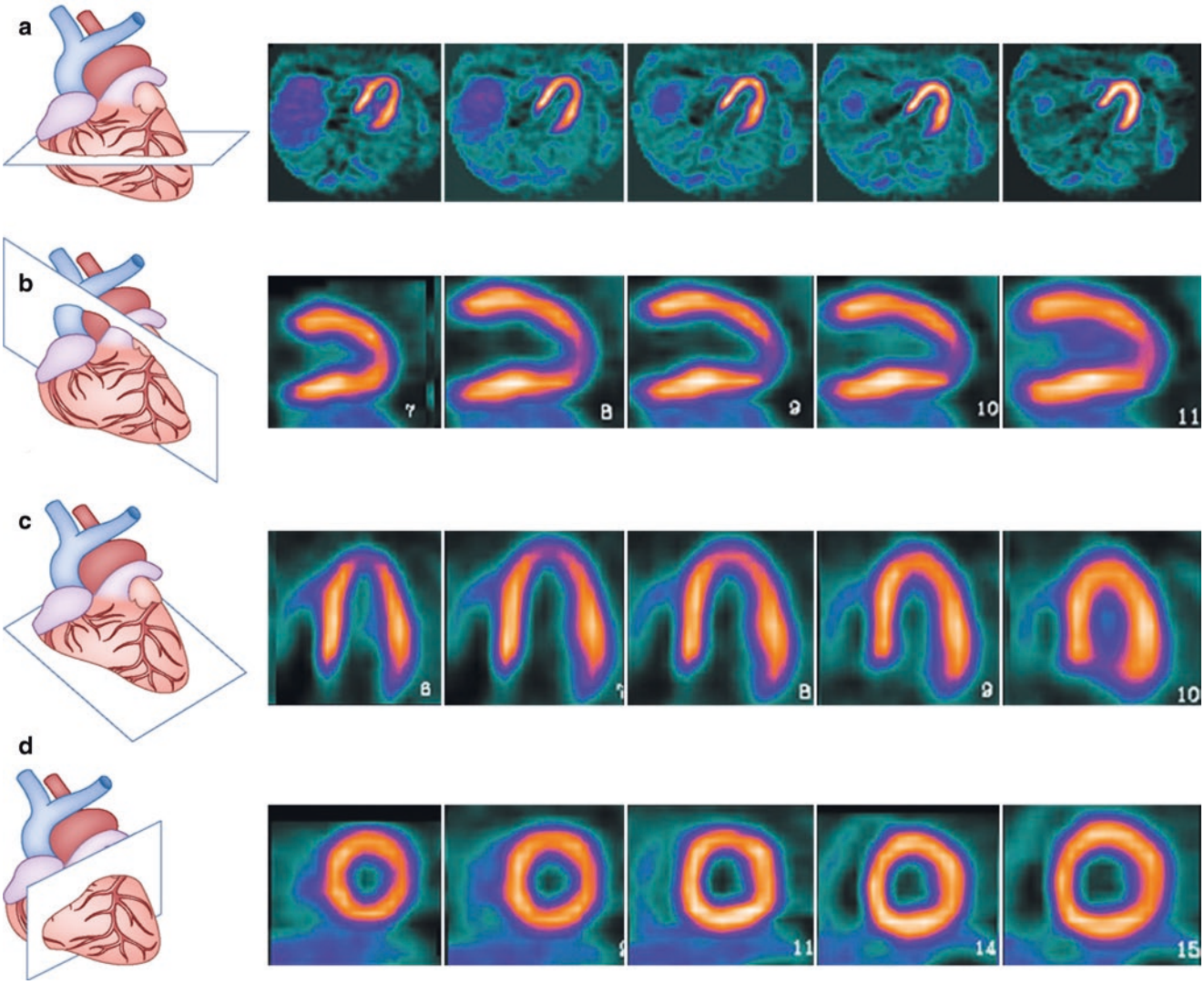

Fig. 2.22 Oblique angle reorientation. *Transaxial images*: The natural products of rotational tomography are images that represent cross-sectional slices of the body, perpendicular to the imaging table (or the long axis of the body). These images are called *transverse* or *transaxial* slices. (**a**) An example of transaxial slices is shown

Oblique images: We are not restricted to the natural *x*, *y*, and *z* directions, however, for the display of images. The computer may be used to extract images at any orientation, and these images are called *oblique images*. Because of the variation in the heart orientation of different patients, it is important that oblique slices are adjusted to try to match the same anatomy from patient to patient. The important oblique sections used for viewing cardiac images are defined as follows:

Vertical long-axis slices: The three-dimensional set of transaxial sections, some of which are shown in (**a**), is resliced parallel to the long axis and perpendicular through the transaxial slices. Each of the resulting oblique images is called a *vertical long-axis slice* (**b**). They are displayed with the base of the left ventricle toward the left side of the image and the apex toward the right. Serial slices are displayed from medial (septal) to lateral, *left to right*

Horizontal long-axis slices: The three-dimensional block of vertical long-axis slices is recut parallel to the denoted long axis and perpendicular to the stack. The resulting oblique cuts are called *horizontal long-axis slices* (**c**). They contain the left ventricle with its base toward the bottom of the image and its apex toward the top. The right ventricle appears on the left side of the image. Serial horizontal long-axis slices are displayed from inferior to anterior, from *left to right*

Short-axis slices: Slices perpendicular to the denoted long axis and perpendicular to the vertical long-axis slices are also cut from the stack. These are termed *short-axis slices*; they contain the left ventricle with its anterior wall toward the top, its inferior wall toward the bottom, and its septal wall toward the left. (**d**) Serial short-axis slices are displayed from apex to base, from *left to right*

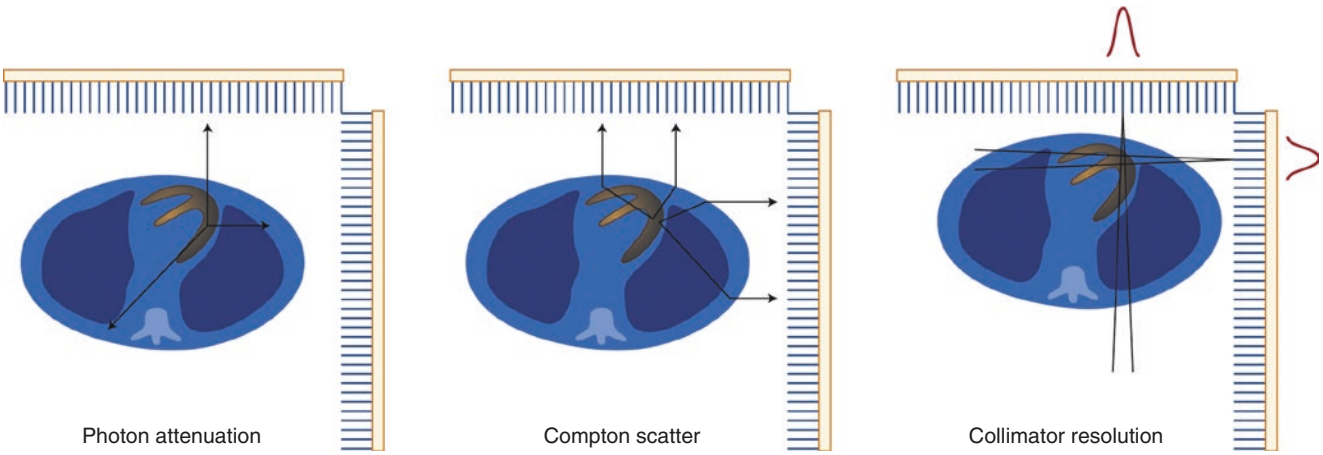

Fig. 2.23 Physical factors that may affect SPECT image formation. Accurate reconstructions of the radionuclide distribution in the body depend on accurate detection of the emitted γ-rays. However, not all of the γ-rays emitted by a radionuclide emerge from the body, and those that do are not all detected in the right place. These complicating factors degrade the resulting image. The three factors that cause degradations in SPECT are attenuation, scatter, and distance-dependent resolution or blur of collimation. Attenuation is the absorption of γ-rays by other materials and includes photons lost due to both the photoelectric effect and Compton scattering. The probability that a γ-ray is absorbed increases with the density of the material through which it must pass but decreases with increasing energy of the photon

Other γ-rays may interact with electrons in the material through which they are passing, causing them to change direction and lose energy. These γ-rays may still emerge from the body but from a direction other than their original path. If these γ-rays are detected by the gamma camera, they appear to be originating from the wrong place. Finally, γ-rays traveling in paths other than parallel to a collimator hole may still travel through that hole and be detected by the camera. This becomes more likely as the source gets farther and farther away from the collimator. The result is a blurring in the final image that depends on the distance between the source and collimator, called the *detector response*, which was discussed in Fig. 2.17

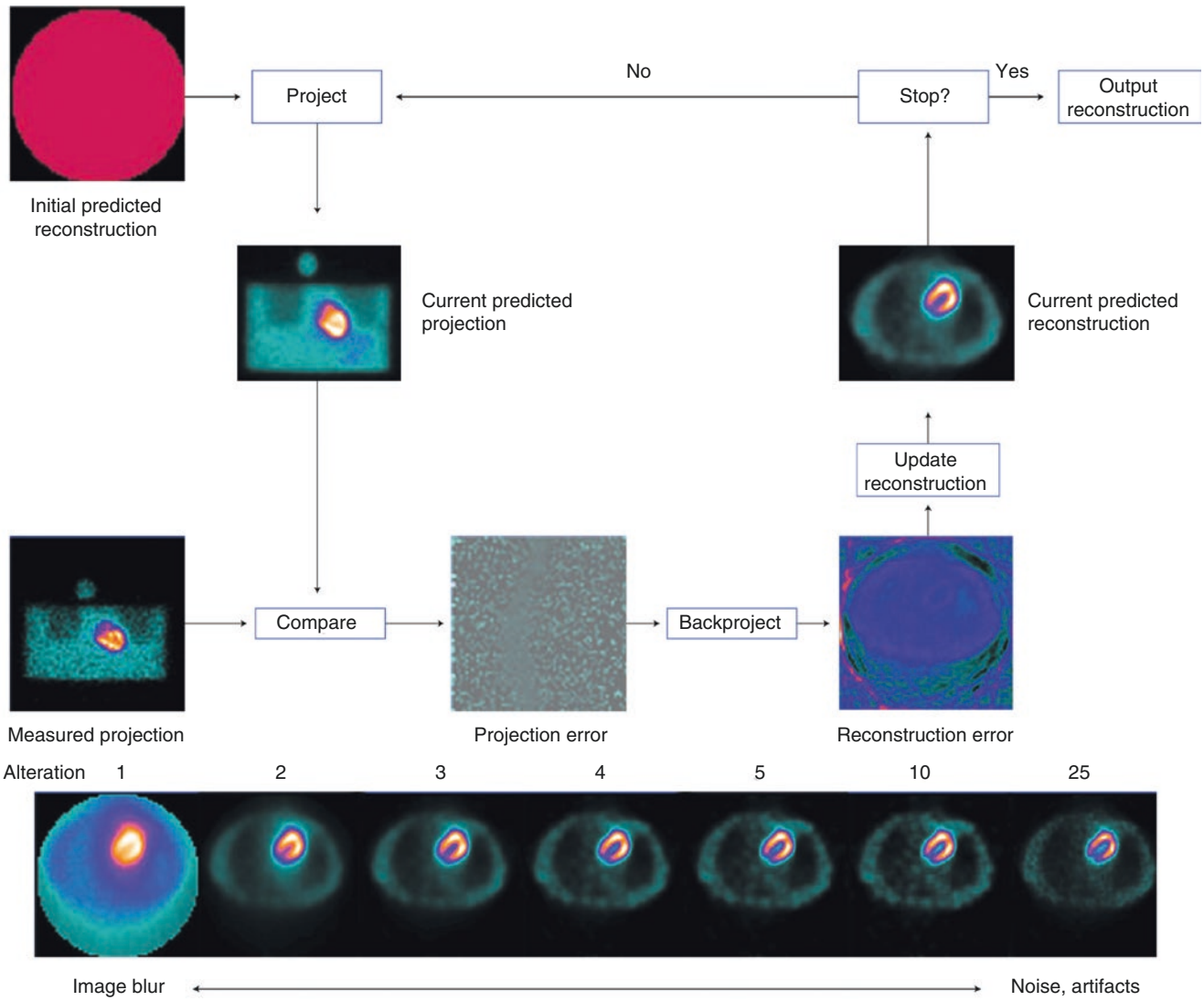

Fig. 2.24 Principle of iterative reconstruction. Iterative reconstruction techniques require many more calculations and, thus, much more computer time to create a transaxial image than does filtered backprojection. However, their great advantage is their ability to incorporate into the reconstruction process corrections for the factors that degrade SPECT images. Iterative techniques use the original projections and models of the acquisition process to predict a reconstruction. The predicted reconstruction is then used again with the models to recreate new predicted projections. If the predicted projections are different from the actual projections, these differences are used to modify the reconstruction. This process is continued until the reconstruction is such that the predicted projections match the actual projections. The primary differences between various iterative methods are how the predicted reconstructions and projections are created and how they are modified at each step. Practically speaking, the more theoretically accurate the iterative technique, the more time-consuming the process. Maximum-likelihood methods allow the noise to be modeled, whereas least squares techniques such as the conjugate gradient method generally ignore noise

The most widely used iterative reconstruction method is maximum-likelihood expectation maximization (MLEM) [14]. The MLEM algorithm attempts to determine the tracer distribution that would "most likely" yield the measured projections given the imaging model and a map of attenuation coefficients, if one is available. An example of the reconstruction of the myocardium with the MLEM algorithm is shown at the *bottom*. The point of convergence of this algorithm and the related number of iterations for clinical use are a source of debate. To date, there is no common rule for stopping the algorithms after an optimal number of iterations on clinical data, and protocols describing the optimal number of iterations are largely empirically based. As can be seen in the reconstructions at the bottom, as the iteration number increases, the images generally get less blurry but more noisy

Another approach to the MLEM algorithm for iterative reconstruction is the ordered-subsets expectation maximization (OSEM) approach [15]. This approach performs an ordering of the projection data into subsets. The subsets are used in the iterative steps of the reconstruction to greatly speed up the reconstruction. The advantage of OSEM is that an order-of-magnitude increase in computational speed can be obtained

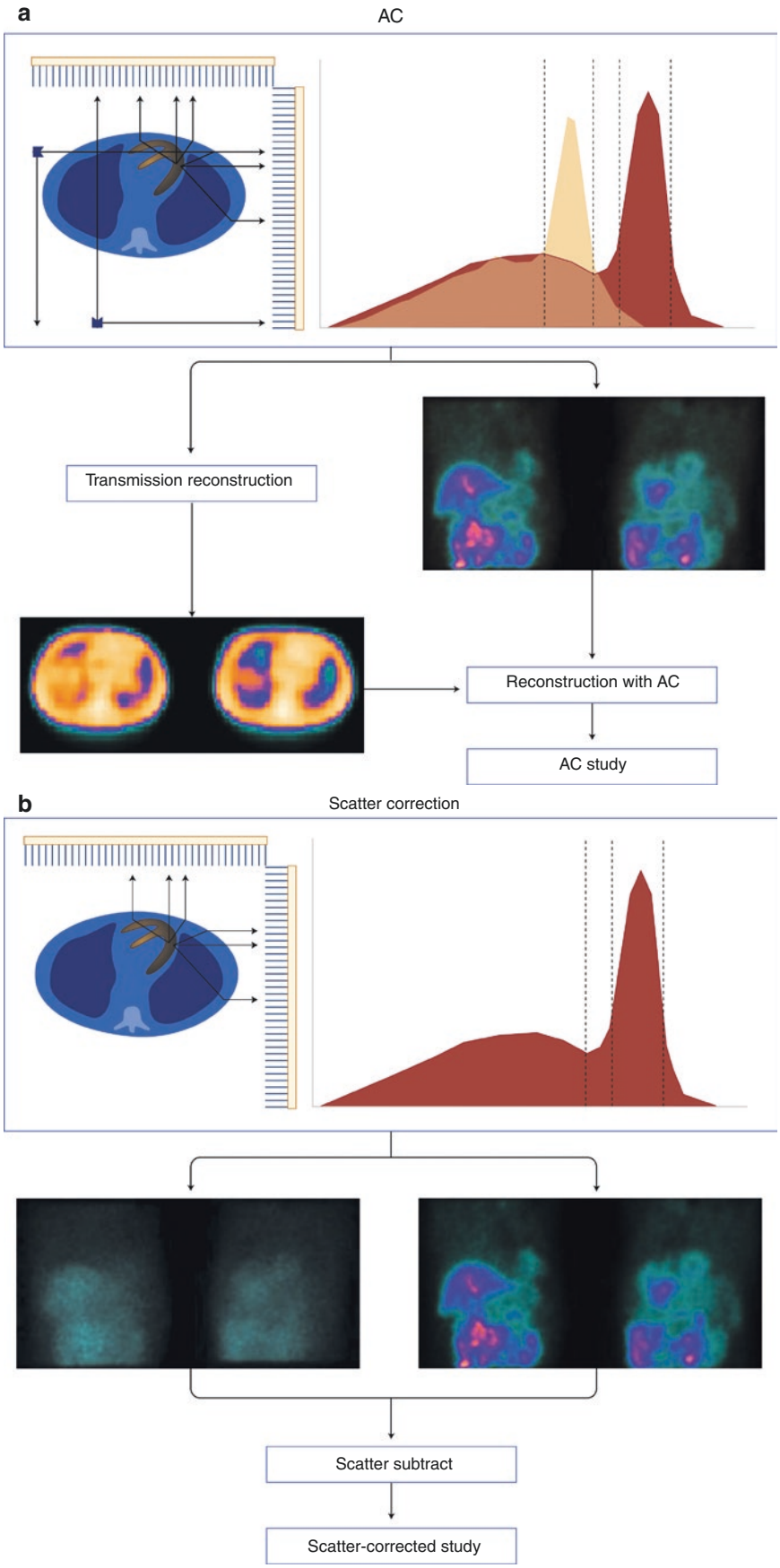

Fig. 2.25 SPECT attenuation correction (AC) and scatter correction. (**a**) SPECT myocardial perfusion imaging uses transmission scan–based AC. Transmission scanning measures the distribution of attenuation coefficients (attenuation map) of the patient, which is used in iterative reconstruction to correct for the decrease in counts resulting from photon attenuation. (**b**) SPECT scatter correction uses the Compton window subtraction method [16]. In this method, an image that consists of scattered photons is acquired by a second energy window placed below the photopeak window. This image is multiplied with a scaling factor and then subtracted from the acquired photopeak window image to produce a scatter-corrected image. Another energy window–based approach uses two energy windows, one above and one below the photopeak window, to estimate the portion of scattered photons in the photopeak window [17]

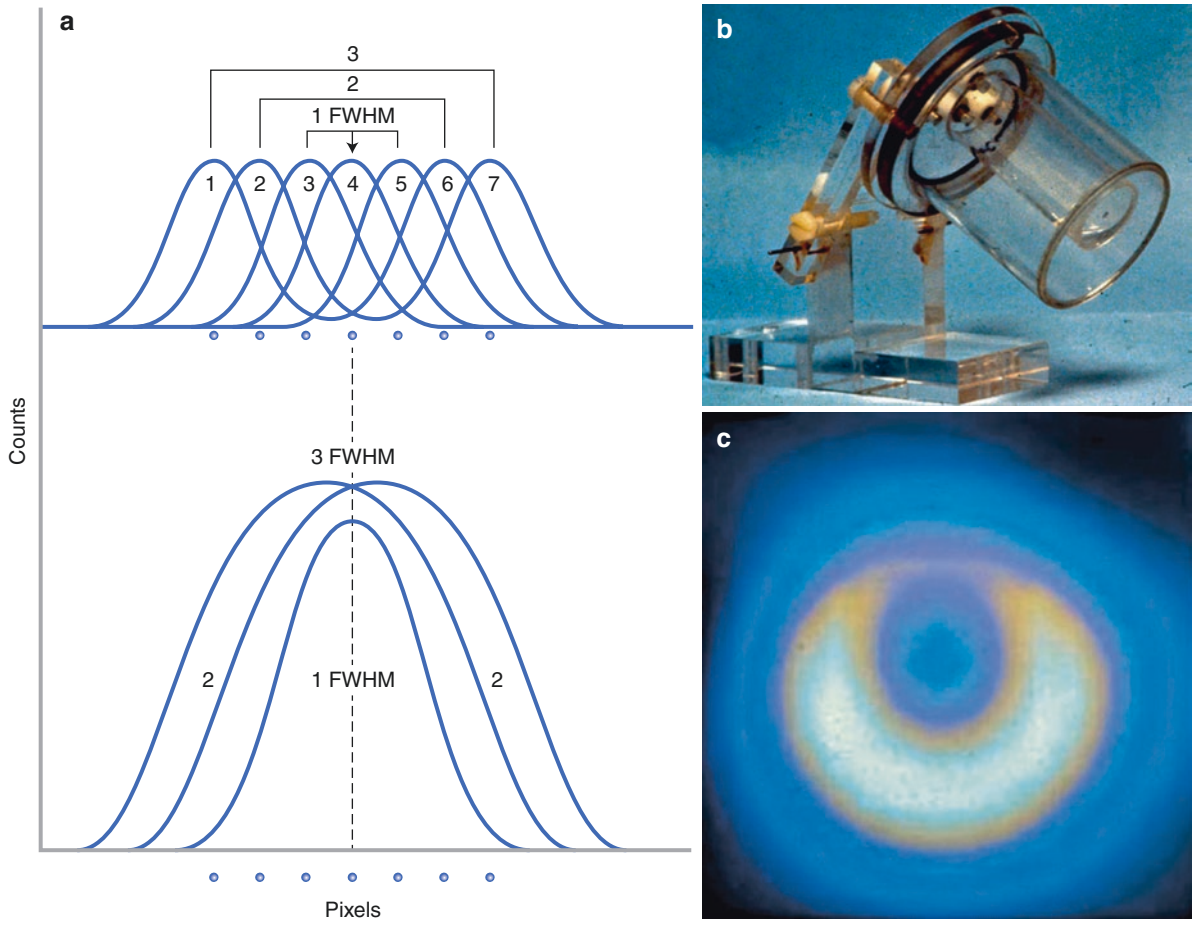

Fig. 2.26 (**a**) Partial volume effect. The inherent limitation of the resolution of nuclear imaging systems makes the image of a point source appear as a Gaussian curve. Therefore, the image of an object made up of multiple points appears as overlapping Gaussian curves, which have a higher value for the center point than for the peripheral points, even when the object has a uniform distribution of the radiotracer. As a result of this phenomenon, myocardial brightness increases when myocardial thickness increases [13] up to twice the resolution of the system (full width at half maximum, FWHM), as shown here. If the object is thicker than two times FWHM, the resulting count profile will reach a plateau representative of the true expected counts. (**b** and **c**) The partial volume effect is used quite successfully to assess left ventricular regional myocardial thickness and thickening, but care must be taken when interpreting gated SPECT images because the myocardium appears brighter in areas where it is thicker and dimmer in areas where it is thinner. These figures show a study in which a phantom representing an eccentric myocardial chamber is filled with a constant concentration of thallium-201. Note that the thinner anterior wall appears to be hypoperfused, in comparison to the inferior wall. This can be a cause of misinterpretation when, for example, the patient has a hypertrophic, thickened septum, making the left ventricular lateral wall with normal thickness and perfusion appear to be hypoperfused

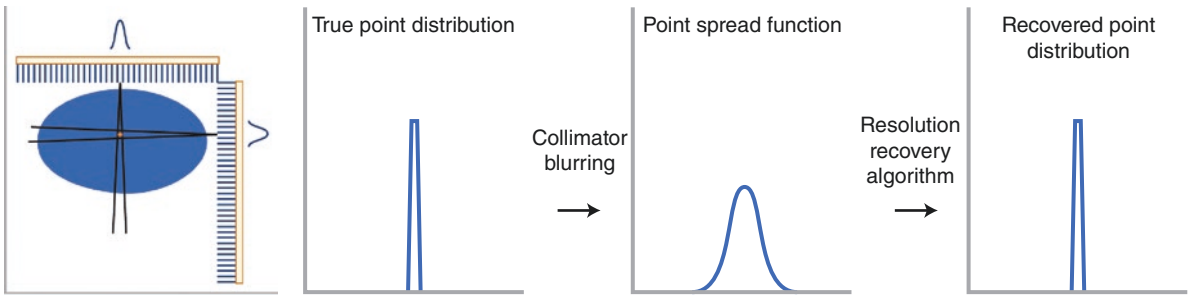

Fig. 2.27 Principle of resolution recovery. The limited resolution of nuclear imaging systems makes the image of a point source appear as a Gaussian curve (point spread function, PSF). The PSF of a nuclear imaging system increases in width with distance away from the surface of the collimator. Measurement of the PSF of the system at various distances allows the development of a resolution recovery algorithm, which deblurs the image and improves the defect contrast. Two types of resolution recovery algorithms are now commercially available: inverse filtering based on the frequency–distance principle [18], and three-dimensional modeling of the distance-dependent collimator response in iterative reconstruction [19]. As shown in this figure, the main idea of resolution recovery is to apply a mathematical algorithm to transform the blurred image response into a sharp response

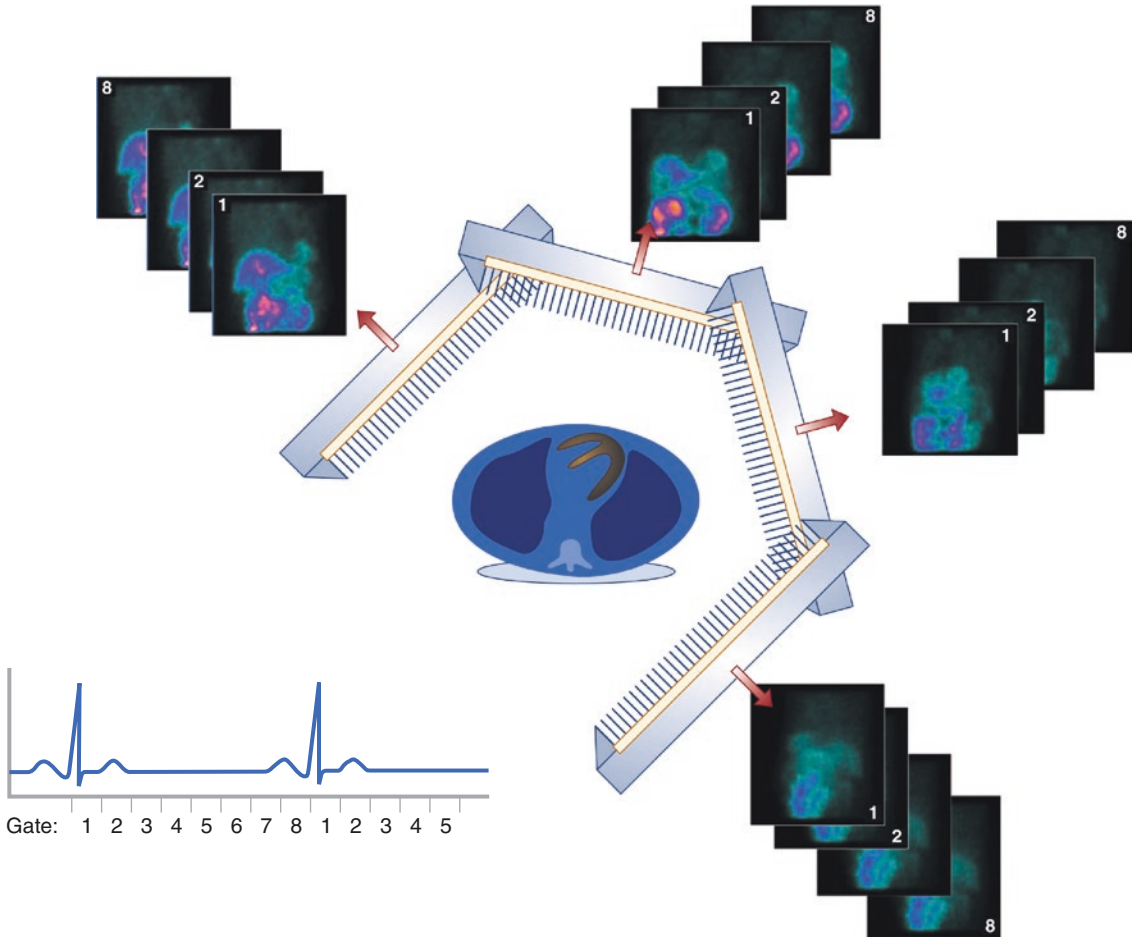

Fig. 2.28 Electrocardiogram (ECG)-gated SPECT myocardial perfusion imaging (MPI) acquisition. Similar to ungated SPECT MPI acquisition, ECG-gated SPECT MPI acquisition collects projection images at equally spaced angles along a 180° or 360° arc during the camera rotation. At each angle, instead of acquiring only one projection in the ungated acquisition mode, the camera acquires several (8, 16, or 32) projection images, each of which corresponds to a specific phase of the cardiac cycle. This is done by synchronizing the computer acquisition to the R wave from the patient's ECG. Here, the cardiac cycle is divided into eight separate frames. If the heart rate is, for example, one beat per second, the computer algorithm assigns a one eighth of a second time interval to each frame. Once the first R wave is detected, all counts are acquired into the first frame; as one eighth of a second elapses, the counts are now acquired into the second frame, and so on until the first second has elapsed or a new R wave is detected, starting the same procedure over again. This technique produces four-dimensional image volumes (three dimensions in space plus time) and allows clinicians to assess not only myocardial perfusion but also myocardial function

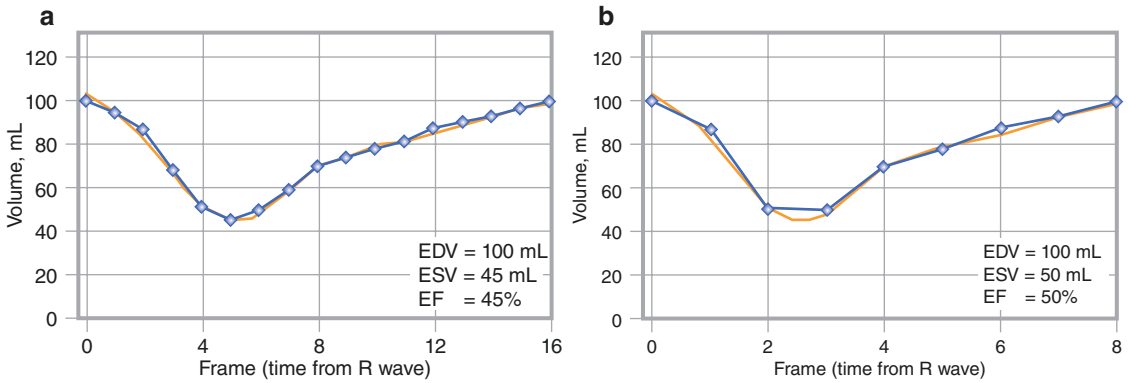

Fig. 2.29 Principle of temporal resolution. (**a** and **b**) The volume-time curve plots the value of the left ventricular cavity volume as a function of the gated SPECT time interval. The smaller the time interval (the larger the number of frames acquired during a cardiac cycle), the higher the temporal resolution and the closer the volume-time curve is to the "truth" and, thus, the more accurate the volume and ejection fraction measurements. It is generally agreed that some commonly used eight-frame-gated SPECT approaches produce errors in the measurement of diastolic function, and it has been suggested that 16-frame imaging is quite effective [20]. There are techniques that use a mathematical algorithm (the Fourier transform) to replace the discrete eight samples with a continuous curve on a segment-by-segment basis and, thus, are less dependent on higher temporal resolution to obtain accurate parameters. EDV end-diastolic volume, EF ejection fraction, ESV end-systolic volume

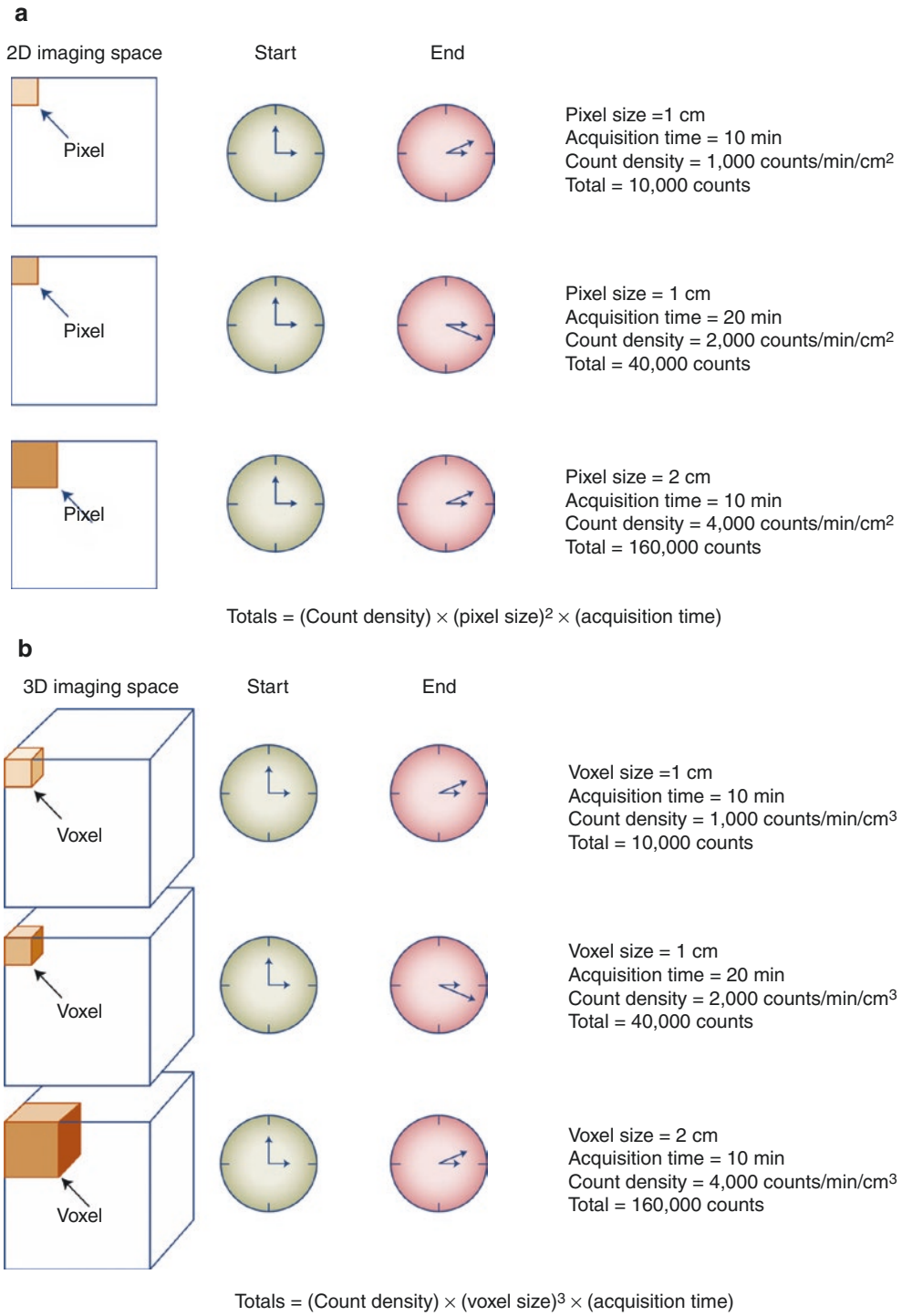

Fig. 2.30 Total counts versus count density, preset time of acquisition, and pixel/voxel size. Nuclear imaging acquires photons emitted from the patient and digitizes the data into a matrix (*image*). Each matrix position corresponds to a pixel, and the pixel value (total counts) corresponds to the number of accepted photons at that position. (**a**) The pixel value is proportional to the radiotracer concentration, the length of the acquisition, and the square of the pixel size. (**b**) If the image is three-dimensional (e.g., reconstructed tomographic image), each element of the image is cubic instead of a square and is called a "voxel." The voxel value (total counts) is proportional to the radiotracer concentration, the length of the acquisition, and the cubic (not square) voxel size. 3D three-dimensional, 2D two-dimensional

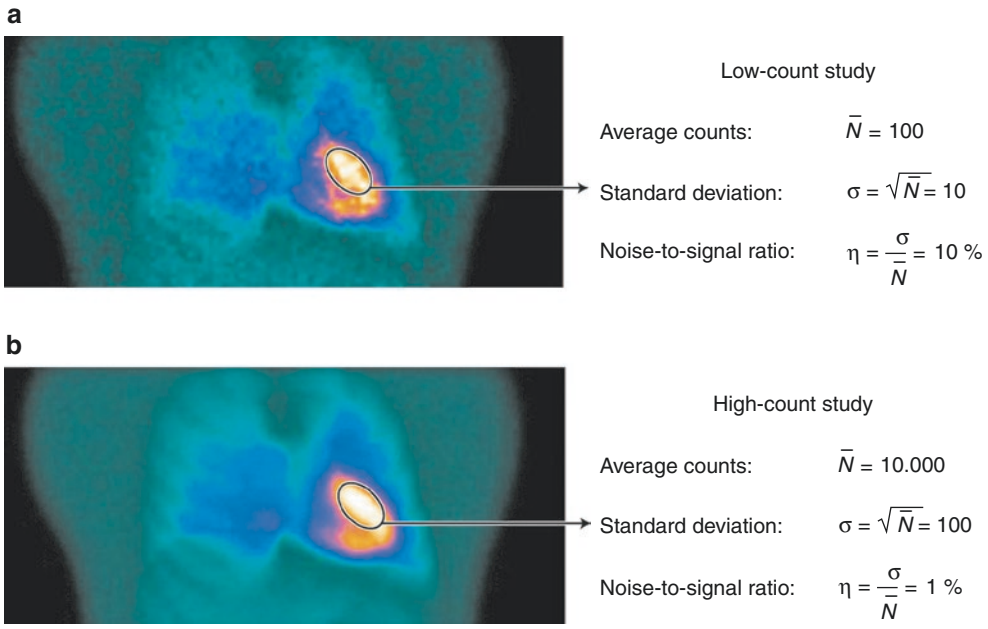

Fig. 2.31 Statistics: noise level versus total counts. Nuclear imaging measures radioactive decay, which is a random process and follows the Poisson distribution. The standard deviation of a measured pixel value (counts) from a planar image projection is the square root of the pixel value. A low-count study (**a**) has a bigger standard deviation and a higher noise-to-signal ratio such that the image appears to be noisier than that of a high-count study (**b**). This example shows that if a pixel contains 100 counts, it corresponds to a 10% error and if another pixel contains 10,000 counts, it corresponds to a 1% error

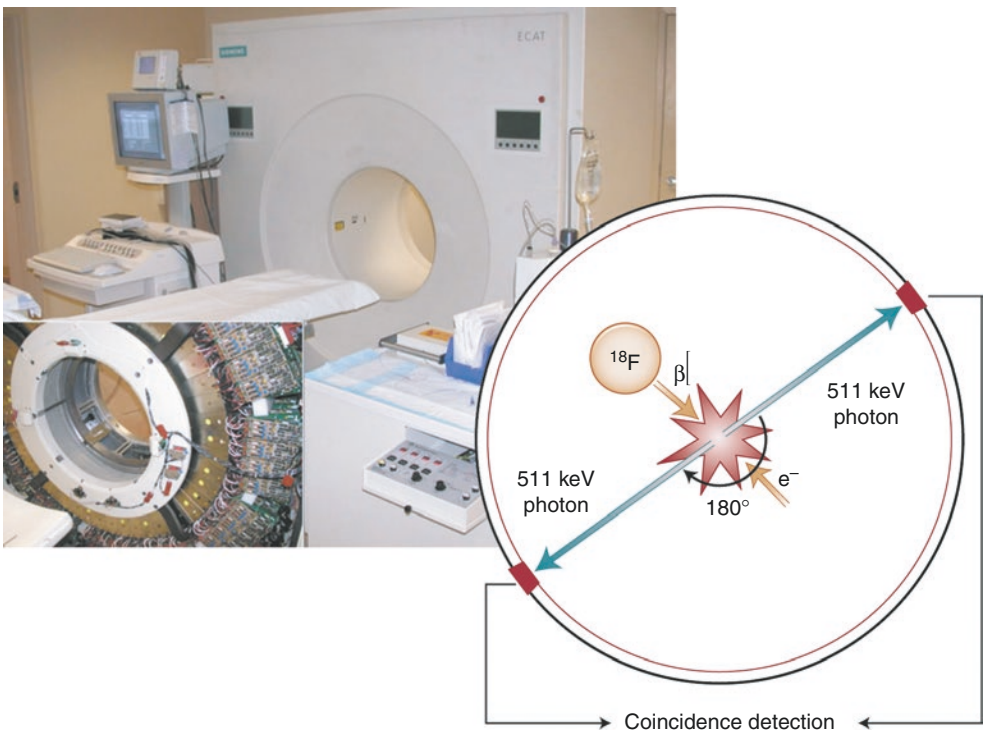

Fig. 2.32 PET scanners; electronic collimation. PET cameras detect paired photons (511 keV of energy each) produced by the positron annihilation effect. The paired 511-keV photons travel in opposite directions at a 180° angle from each other. Thus, positron decay can be localized without collimation with the use of the principle of coincidence detection, because if two detectors acquire a count within a short time window, it is assumed that they came from the same pair annihilation, so the event is positioned by drawing a straight line between the two detectors. Because PET cameras do not require collimators, these systems have a much higher sensitivity than SPECT systems. ^{18}F fluorine-18

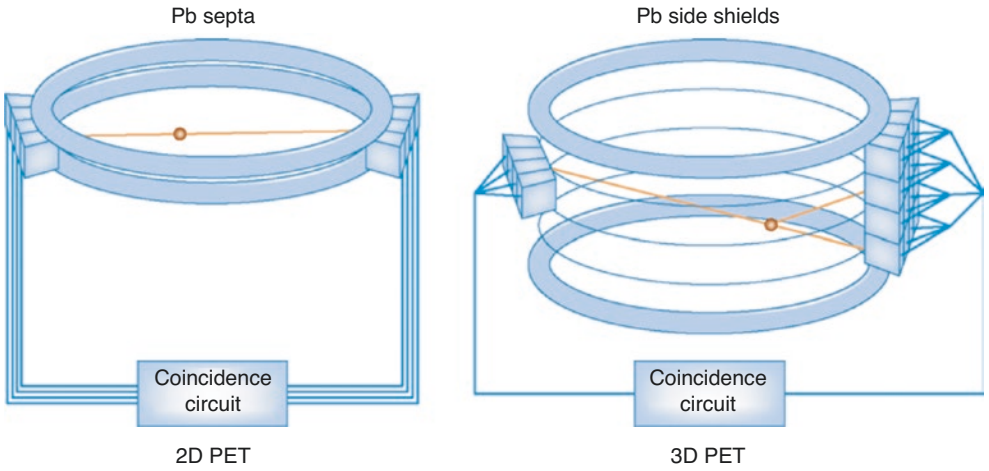

Fig. 2.33 Two-dimensional (2D) versus three-dimensional (3D) PET systems. 2D PET systems, equipped with lead (Pb) septa, accept coincidences only from crystals in the same ring of detectors. 3D PET systems, by removing the septa, accept coincidences in any ring and greatly increase the count rate and sensitivity. However, the difficulties associated with removing the septa are that it greatly increases scatter, it greatly increases random events, and it greatly increases the count rate, so it greatly increases dead time [21]. These problems must be effectively compensated for when using 3D PET in cardiac imaging

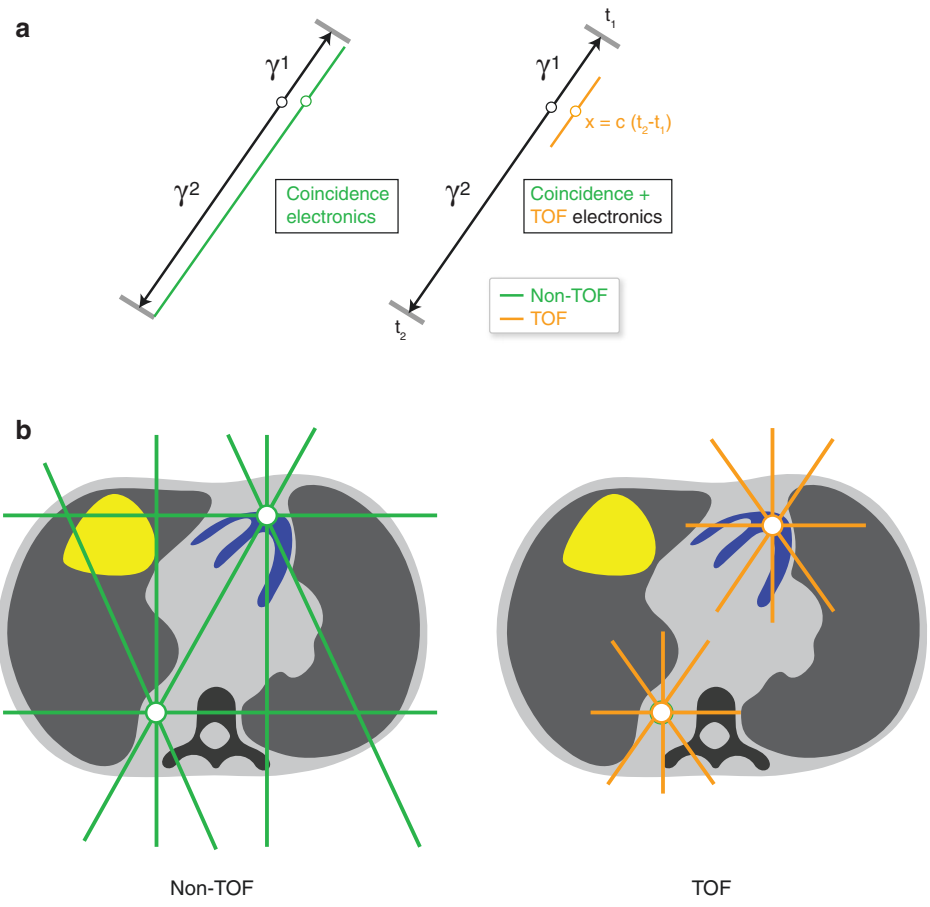

Fig. 2.34 Time of Flight (TOF) imaging vs. Non-TOF imaging. (**a**) On the left, **c**onventional PET coincidence electronics (*see* Fig. 2.32). The right panel shows that the coincidence electronics in advanced PET scanners with TOF electronics are capable of measuring the time interval between one photon (γ_1) hitting one detector and the second photon (γ_2) from the same annihilation event hitting an opposing detector. That difference in time (t_2 - t_1) multiplied by the speed of light (c) estimates the location of the annihilation event along the coincidence ray between the two detectors. (**b**) In TOF, instead of backprojecting an entire line (*left panel*), only the line segment corresponding to the time window of the event is projected. The result is increased lesion contrast and increased spatial resolution [22]

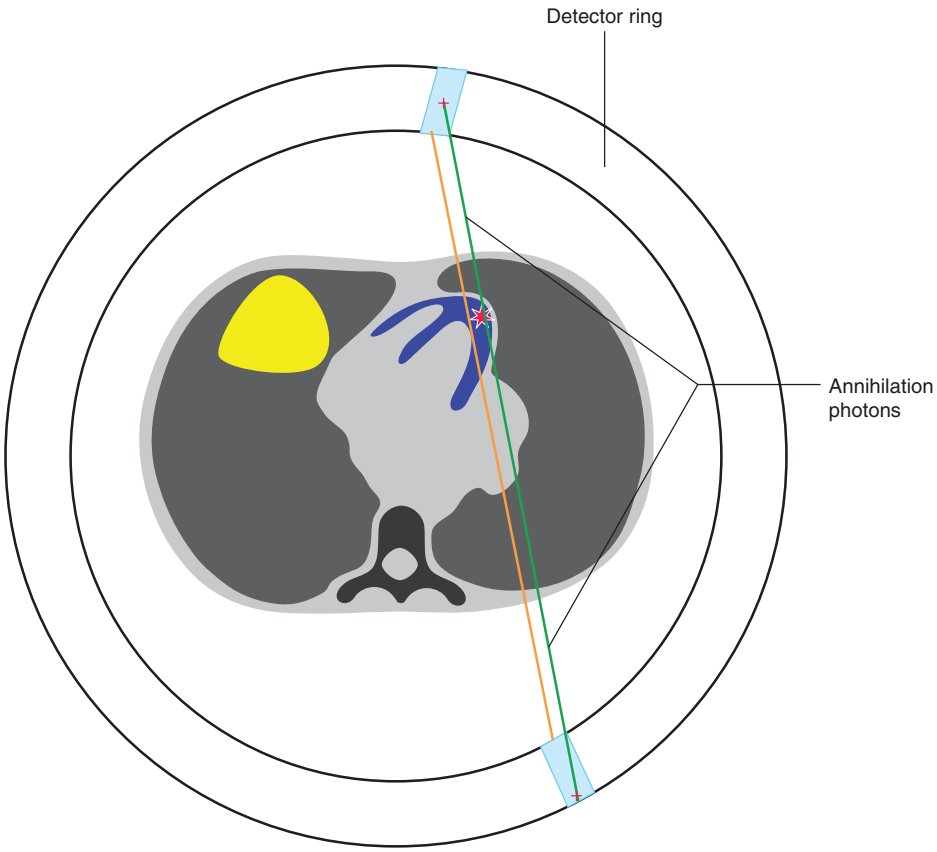

Fig. 2.35 Depth of interaction (DOI) digital PET detectors vs. conventional PET detectors. DOI detectors record both the event that the photon was absorbed by the specific detector (*blue rectangle*) and the depth within the detector (*red plus sign*) where it was absorbed. As the positron annihilation takes place further from the center of the field of view, the reconstructed line of response (*red*) is increasingly further away from the true line of response (*green*) in systems that locate the annihilation photons in the middle of the detector rather than at the true depth of the interaction, as with DOI detectors. This increased accuracy in positioning the backprojected line of response results in increased lesion contrast and increased spatial resolution [23]

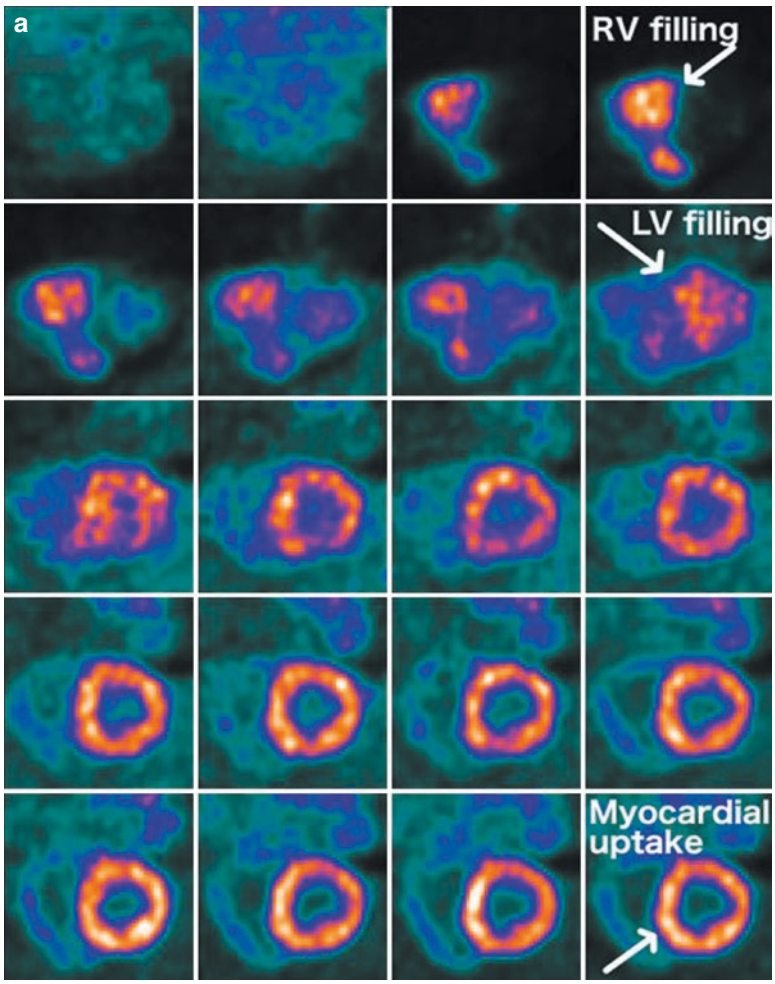

Fig. 2.36 PET-derived myocardial absolute blood flow (MBF) quantification. (**a**) Dynamic sequence of PET images. Once injected, the radiotracer rapidly travels to the right ventricle (RV), then to the left ventricle (LV), and is progressively captured by the myocardial tissue in the second half of the acquisition interval; posterior direction on top of images. (**b**) Procedure for MBF quantification. *B1*, A summed image is created from frames of the second half of the acquisition interval and used to identify regions of interest (ROIs) on the image sequence, namely the myocardium (*black lines*), and the location for the extraction of the input function (IF) (*red*); the IF represents the tracer's arterial blood concentration and is measured by sampling a small region of the LV cavity. *B2*, The segmented myocardium is subdivided into vascular territories according to standard anatomical classification. *B3*, Time activity curves (TACs) are derived by sampling the dynamic sequence of PET images in the segmented ROIs: the input function (IF) is characterized by a rapid increase of radiotracer concentration in the initial frames, followed by a rapid decrease in the second half of the acquisition time. Conversely, radiotracer concentration progressively increases in the myocardial tissue, reaching a plateau towards the end of the acquisition. The exchange of activity between blood and tissue is commonly described by means of compartmental models that allow MBF estimation. *B4*, MBF values in mL/min/g can be displayed by means of conventional polar maps; myocardial flow reserve (MFR) is computed as the MBF hyperemic values divided by the resting MBF. (**c**) Common errors and artifacts in dynamic PET acquisition and processing. Differently from myocardial relative perfusion imaging (MPI), clinical estimation of MBF can be technically more demanding, as a number of factors greatly affect MBF final values. A careful analysis of TACs can facilitate the identification of errors and/or artifacts, as in the two examples here: *C1*, Image acquisition should start at the same time as tracer infusion. In case of delayed acquisition, the initial phase of the TACs, particularly important for the IF definition, may be missing, causing the final MBF values to be completely unreliable. *C2*, Because the ROIs are commonly defined on a single summed image, patient motion and/or breathing motion can result in the misplacement of the ROIs on a number of time frames and, consequently, in inconsistent TACs. In the given example, the shifting of the heart in the posterior direction during frames 24, 25 and 26 clearly results in unsteady activity values for the IF and all myocardial tissues; during frame 27, the heart has returned to its initial position. These inconsistencies should be corrected prior to MBF calculation

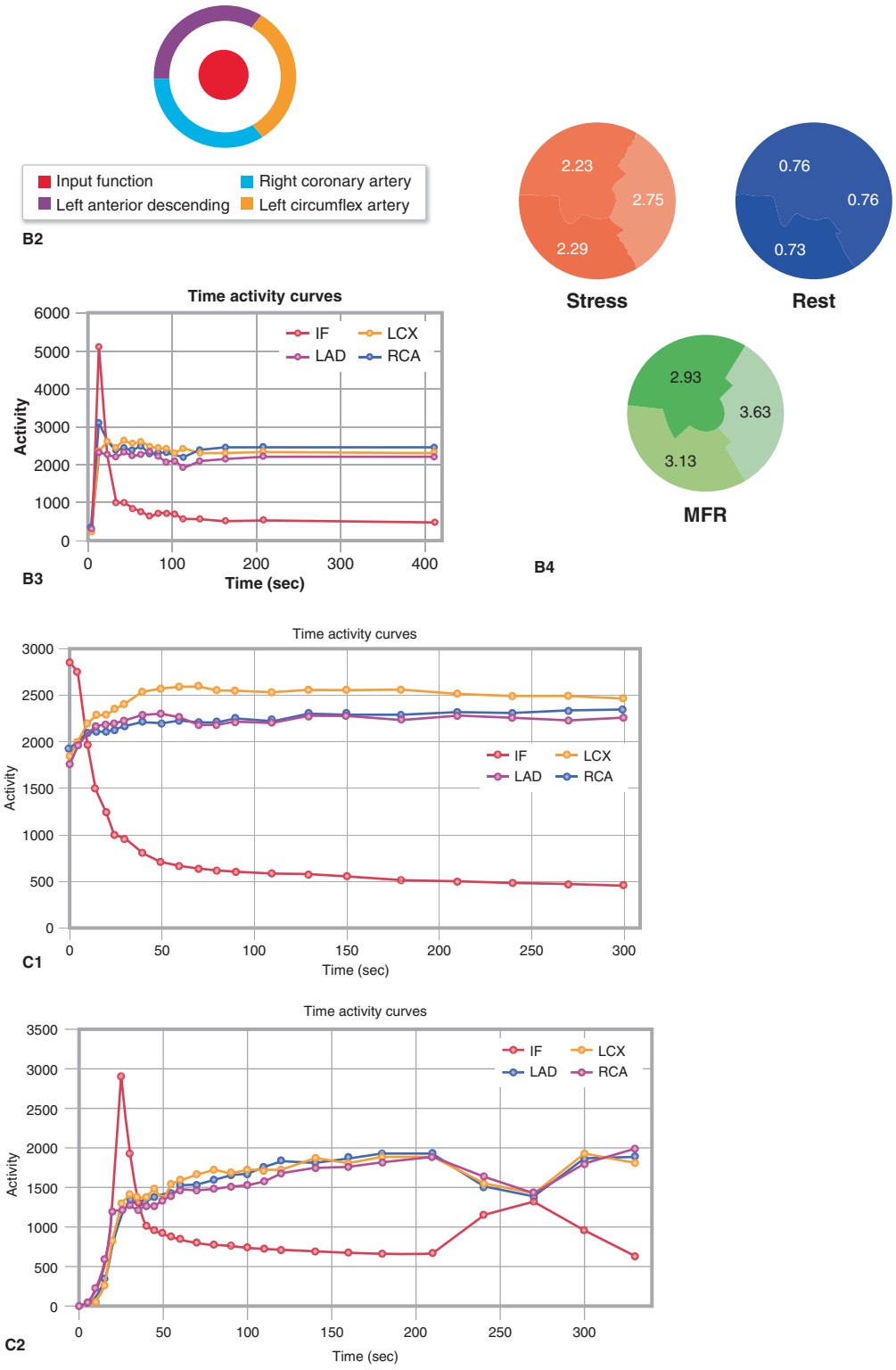

Fig. 2.36 (continued)

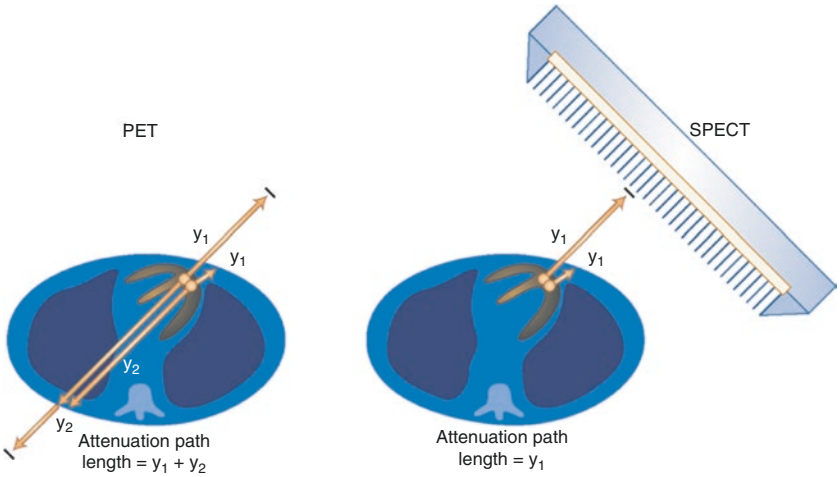

Fig. 2.37 PET *versus* SPECT attenuation correction (AC). PET imaging measures 511-keV photons. Because the two photons must be detected to record the event, the entire path length influences the attenuation. In SPECT imaging, even though the energy of the photon is lower, its path length to the detector is much shorter, so it is less affected by attenuation. Thus, the two PET photons undergo higher attenuation when they travel through the body than do the single photons measured in SPECT imaging. Therefore, there is more attenuation in PET studies than in SPECT, making PET more susceptible to attenuation artifacts. Only attenuation-corrected cardiac images should be used in clinical interpretation [24]. Unlike SPECT, PET data can be accurately corrected for attenuation by simply multiplying each projection line by the appropriate AC factor. For both PET and SPECT, a measurement of the patient-specific attenuation map is required for accurate AC and can be done either by radionuclide imaging or by radiographic CT

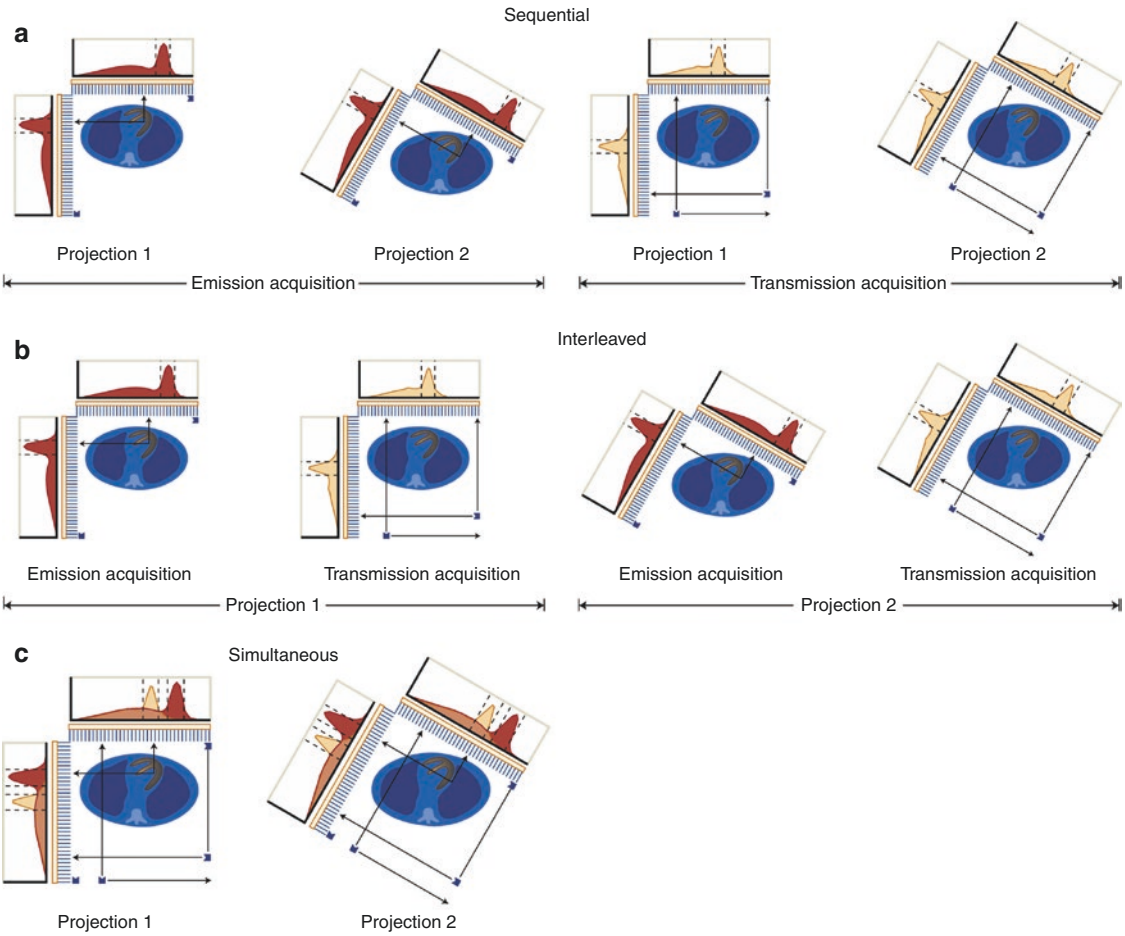

Fig. 2.38 Types of attenuation correction (AC): sequential, interleaved, and simultaneous. Accurate AC requires two acquisitions from a single study: emission and transmission. (**a**) The two acquisitions can be done sequentially, one following the other, but registration between the two acquisitions challenges the quality control of this approach in practice. (**b**) To reduce the risk of emission/transmission misalignment, the two acquisitions can be done in an interleaved mode, in which the camera acquires emission and transmission projection images sequentially at each stop and rotates around the patient only once in one study. (**c**) Simultaneous mode completely solves the problem and reduces the length of the acquisition; however, cross talk between the emission and transmission photons degrades at least one of the two acquisitions and should be properly compensated for with accurate AC

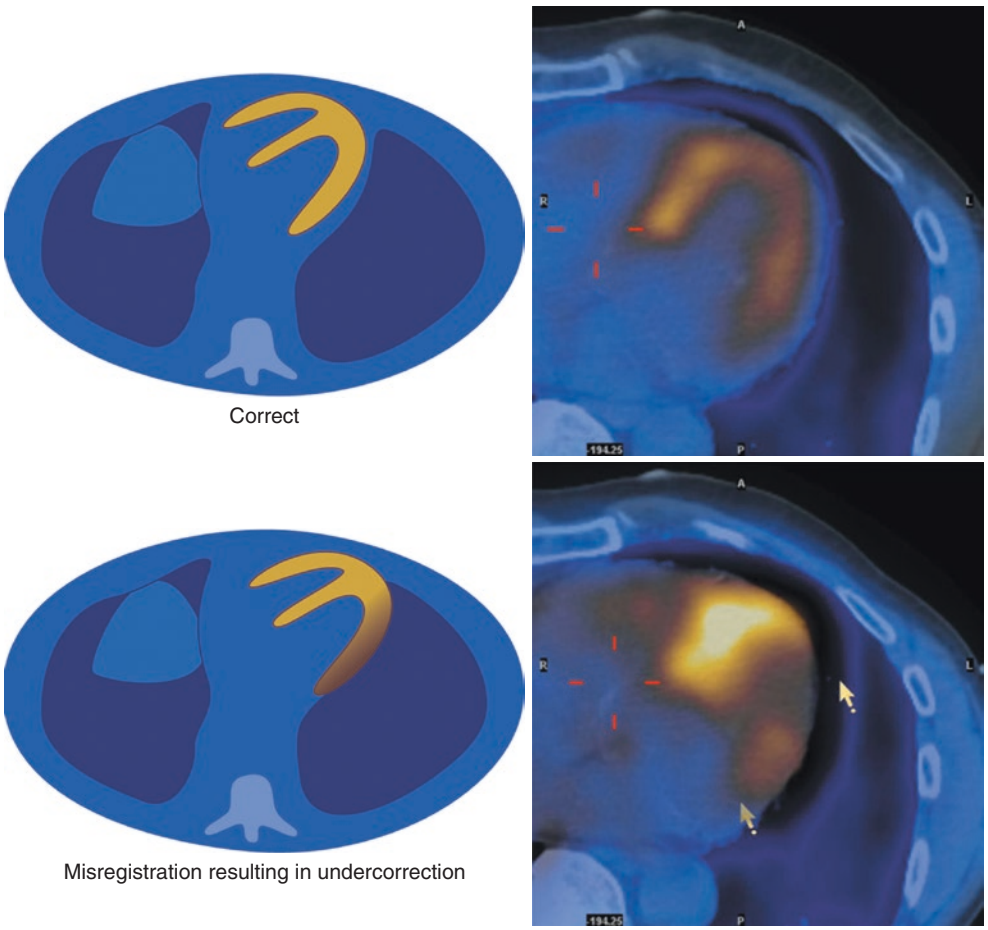

Fig. 2.39 Attenuation correction (AC) artifact due to misregistration. This figure explains the artifact caused by misregistration between the emission and transmission scans due to patient motion. AC requires that the emission scan and the transmission scan that is used to correct for photon attenuation be perfectly registered with each other. Simultaneous acquisitions of both emission and transmission scans ensure that these two are registered. When these two acquisitions are performed sequentially and the patient moves between the two acquisitions, artifacts are created. The *top left panel* shows a diagram of a transaxial emission cardiac image superimposed on the corresponding transaxial transmission image. Note that the entire cardiac silhouette lies in the pericardium, not touching the lung area, represented in *dark blue*. The *top right image* shows an actual AC emission cardiac image when correctly registered with the transmission image. The *bottom left panel* shows a diagram of a transaxial emission cardiac image superimposed on the corresponding transaxial transmission image. Note that the two images are misregistered; the free left ventricular lateral myocardial wall overlaps a portion of the lung. The *bottom right image* shows an actual attenuation-corrected emission cardiac image that is similarly misregistered in relation to the transmission image. Note that the left ventricular free wall overlaps a portion of the lung. This misregistration causes the lateral wall to be undercorrected, so it appears as though it is hypoperfused

Quality Control Procedures

Quality control (QC) procedures are necessary to ensure images of diagnostic quality. These procedures are pertinent to guarantee both the quality of studies when performing planar imaging and the quality of the planar projections used in SPECT imaging. Table 2.5 lists quality control procedures required for planar imaging.

Test	Frequency
Energy peaking	Daily
Uniformity test	Daily
Sensitivity	Manufacturer's recommendation
Resolution and linearity	Manufacturer's recommendation

Table 2.5 Quality control procedures for planar imaging

Energy peaking consists of either manually or automatically placing the correct pulse height analyzer's energy window over the photopeak energy of the radionuclide to be used. This process is usually performed with a radioactive point source imaged a distance away by an uncollimated camera or an extended sheet source on the collimated camera. Either way, the entire field of view should be illuminated by the radioactive source. This process should be performed daily, even in camera systems that perform this function automatically and track the shift of the window. A screen capture of the spectrum with the window superimposed can be used to record these results [25].

The uniformity flood field is another QC procedure that should be performed daily to document the camera uniformity. This procedure is also done using a radioactive point source and without a collimator. An intrinsic uniformity test can be performed using a source of low radioactivity (~100 μCi) in a small volume (~0.5 mL) to mimic a point source positioned at least five diameters from the camera's crystal, directly over the center of the detector. If this process proves difficult or time-consuming, it can be replaced with an extrinsic uniformity flood measurement. Extrinsic uniformity is measured with an extended radioactive sheet source that covers the entire collimated camera face [26].

Sensitivity QC tests that the device is consistently counting the same radioactive source should be performed weekly. These tests can be done at the same time the intrinsic (or extrinsic) uniformity tests are done by recording the number of counts acquired for a given time period, adjusted to the magnitude of radiation used to create the image.

The resolution and linearity test is performed to document spatial resolution and its change over time, as well as how the camera reproduces straight lines. This test consists of imaging an extended radioactive sheet flood source through a spatial resolution test phantom known as a "bar phantom." Images of the phantom should be archived to record the camera's performance and the QC procedure. These images are assessed for how straight the bar lines are imaged and for intrinsic spatial resolution. Changes in resolution are assessed by documenting the smallest bars that are discerned [25].

Table 2.6 summarizes the QC procedures necessary to ensure images of diagnostic quality when performing SPECT imaging, which are described in this chapter. Of course, all the QC procedures required for planar imaging are also required for SPECT imaging. Several excellent reviews on how to detect and account for SPECT imaging artifacts have been published [27, 28].

Test	Requirement
Center-of-rotation and multidector registration	Mandatory/Manufacturer's recommendation
Uniformity calibration	Mandatory/Manufacturer's recommendation
Motion correction	Optional

Table 2.6 Quality control procedures for SPECT imaging

Figures 2.40, 2.41, 2.42, and 2.43 illustrate areas of quality control for SPECT imaging.

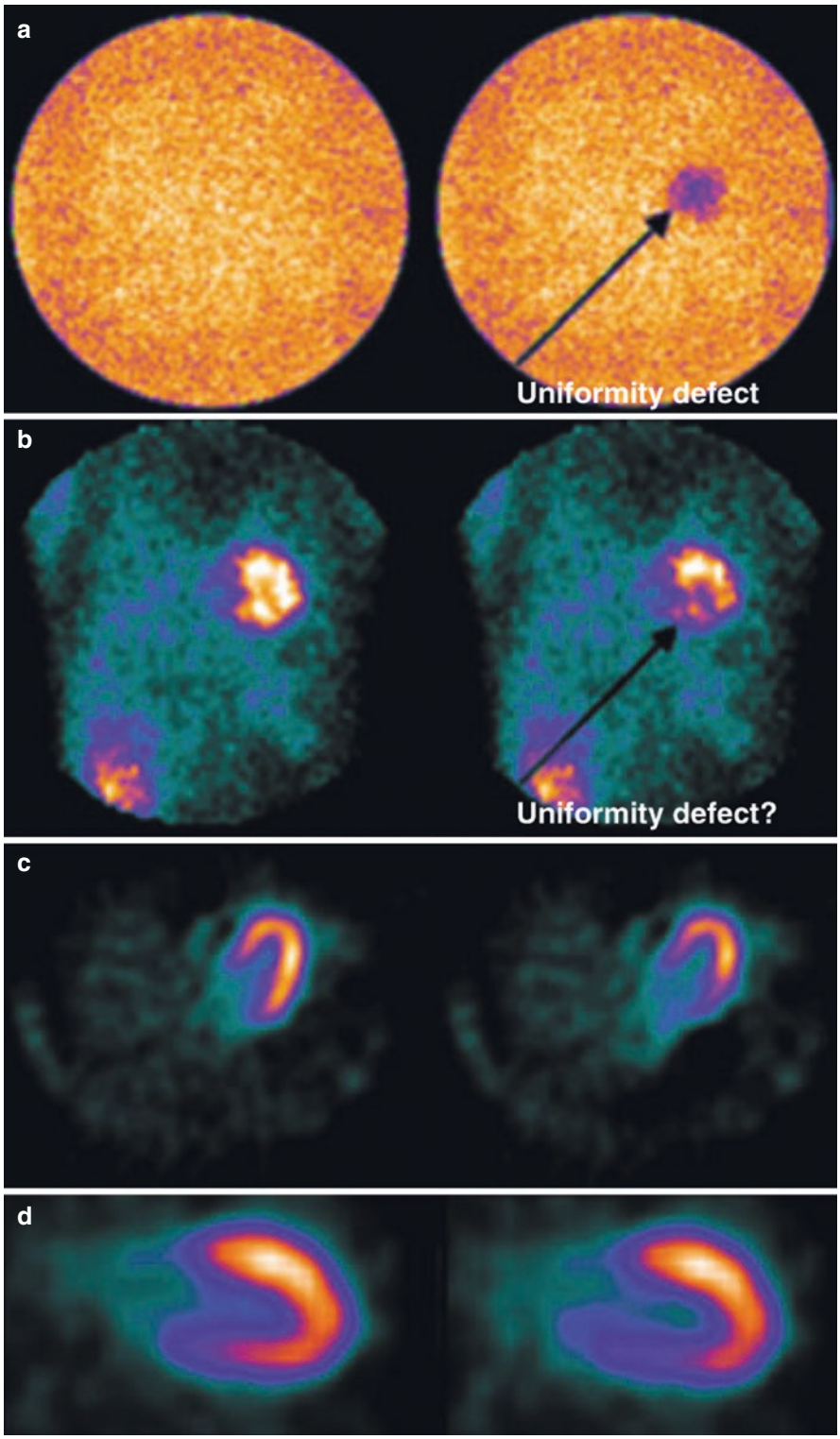

Fig. 2.40 Camera uniformity. The Joint Commission on the Accreditation of Healthcare Organizations (JCAHO) requires that a uniformity flood be acquired on each scintillation camera before clinical studies are done for any given day. These three-million-count floods can be used to detect uniformity defects. (**a**) Two examples of floods, one using a camera without a uniformity defect (*left*) and one with a uniformity defect that might be caused by a poor photomultiplier tube (*right*). (**b**) In the same patient, corresponding thallium planar projections were acquired with these cameras. Note that the planar image on the *right* shows decreased counts compared with the one on the *left*. The problem is that even if cine displays of the planar images are viewed, it will be very difficult to detect that the decreased counts in the inferior myocardial wall were caused by a camera uniformity problem rather than a true physiologic perfusion abnormality. (**c**) Correspondingly, when the transaxial slices are reconstructed, the basolateral wall is decreased in counts. Although a ring artifact is caused by this uniformity problem and can be seen in the transaxial images when imaging a uniform source, in this patient they are difficult to detect just by looking at the images if the quality control step is not performed. (**d**) The vertical long-axis images make it even harder to detect when a decrease in counts might be the result of a uniformity defect. It is very important that floods be performed every day to detect uniformity problems before they affect clinical images. Differences in positioning of the patient between rest and stress scans may cause uniformity artifacts to appear in different locations in the two images, possibly mimicking ischemia [12]

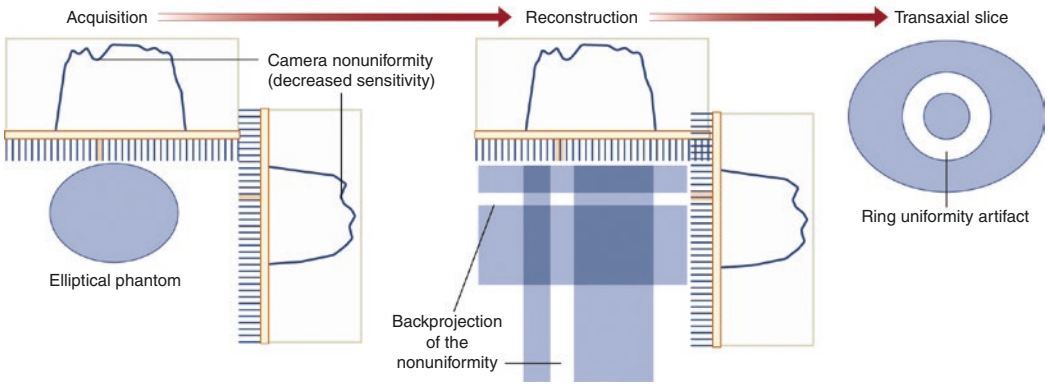

Fig. 2.41 Uniformity artifacts. Uniformity artifacts occur when one area of the camera face has decreased sensitivity compared with the other areas. This can occur when a photomultiplier tube begins to work improperly, as in Fig. 2.38, or if the collimator is damaged. For example, if an acquisition is performed of an elliptical quality control phantom that was filled with a uniform distribution of technetium, it can generate the two count profiles on the *left side* of the figure. These count profiles should be steep on the sides and fairly flat across the top, depending on the shape of the phantom. In the case of uniformity problems, regions of decreased sensitivity are seen in each of these curves, represented by a small dip at one point. The small dip will correspond to the same location on the camera in all of the projection views. When the images are reconstructed, this small dip is backprojected, as shown in the *middle image*, and with more and more projections, it will scribe out a circle in the transaxial image, as shown on the *right*. This kind of artifact may occur when the collimator is damaged and one or a few of the holes in the lead septa have been closed. To correct for small variations across the face of a collimator, 30-million-count floods are used. These high-count floods should be acquired at least once a month and are applied to images acquired with the same collimator being used by the same camera [12]

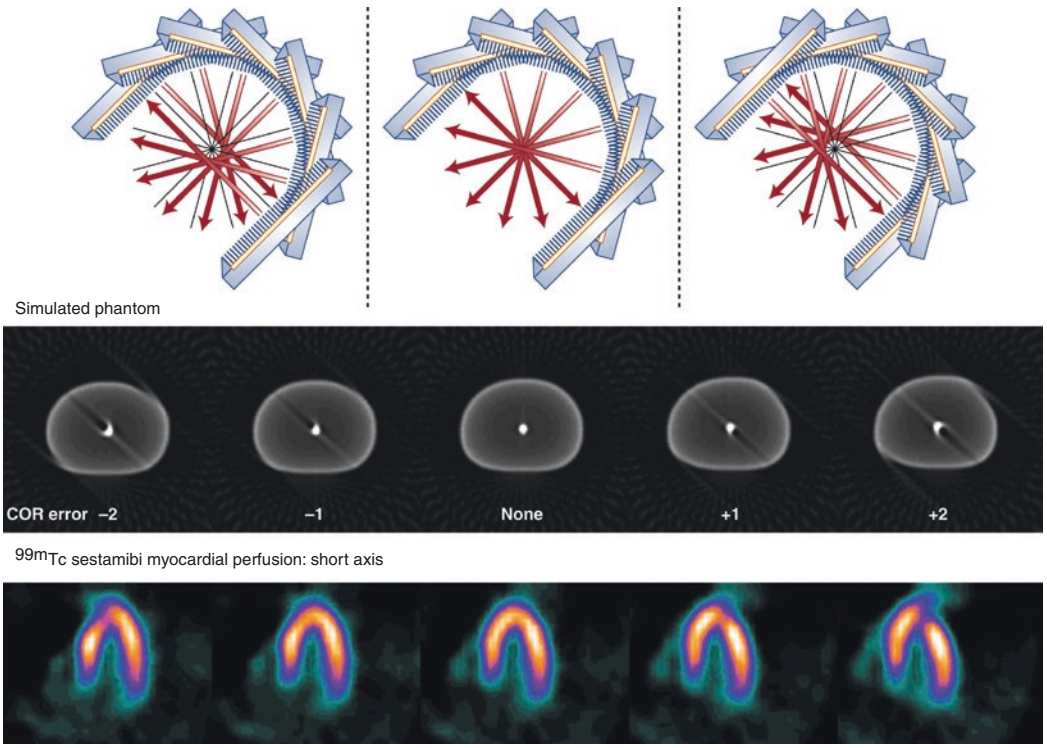

Fig. 2.42 Center of rotation (COR). COR is a calibration performed frequently to ensure that the frame of reference used by the computer in reconstructing images is aligned with the mechanical axis of rotation of the SPECT camera system. If the center of rotation is properly calibrated, a radioactive point source placed in the center of the camera orbit should project to the center of the computer matrix. These results are seen in the *middle panels*

For most cardiac SPECT, a 180° orbit is used. When a radioactive point source is used with this orbit, a point source should also be reconstructed as a point in the image. With a COR error, however, the reconstruction no longer yields a point. Instead, the point is smeared and resembles a tuning fork, with two lines in one direction and something that looks like a stem in the opposite direction ("tuning fork artifact"). If the COR calibration errs by a negative amount, the images in the *left panels* are seen. In the *middle left panels*, the smeared radioactive point sources reconstructed with this error are seen. If the error is in the positive direction, the images shown in the *top right* are seen. The camera processes that generated these errors are seen in the *top diagrams*

COR errors are easy to detect with radioactive point sources, but they may be very difficult to detect with a clinical distribution of activity. In the *bottom panels*, COR errors can be seen that correspond to the images of point sources directly above them. The COR error manifests itself in the myocardial perfusion horizontal long-axis images as an area of reduced counts on either side of the myocardium (often surrounding an area of higher counts). It is sometimes difficult to distinguish between the COR errors demonstrated here and true clinical defects, so it is extremely important that the technologists who perform the QC procedures properly calibrate the COR for the camera [12]

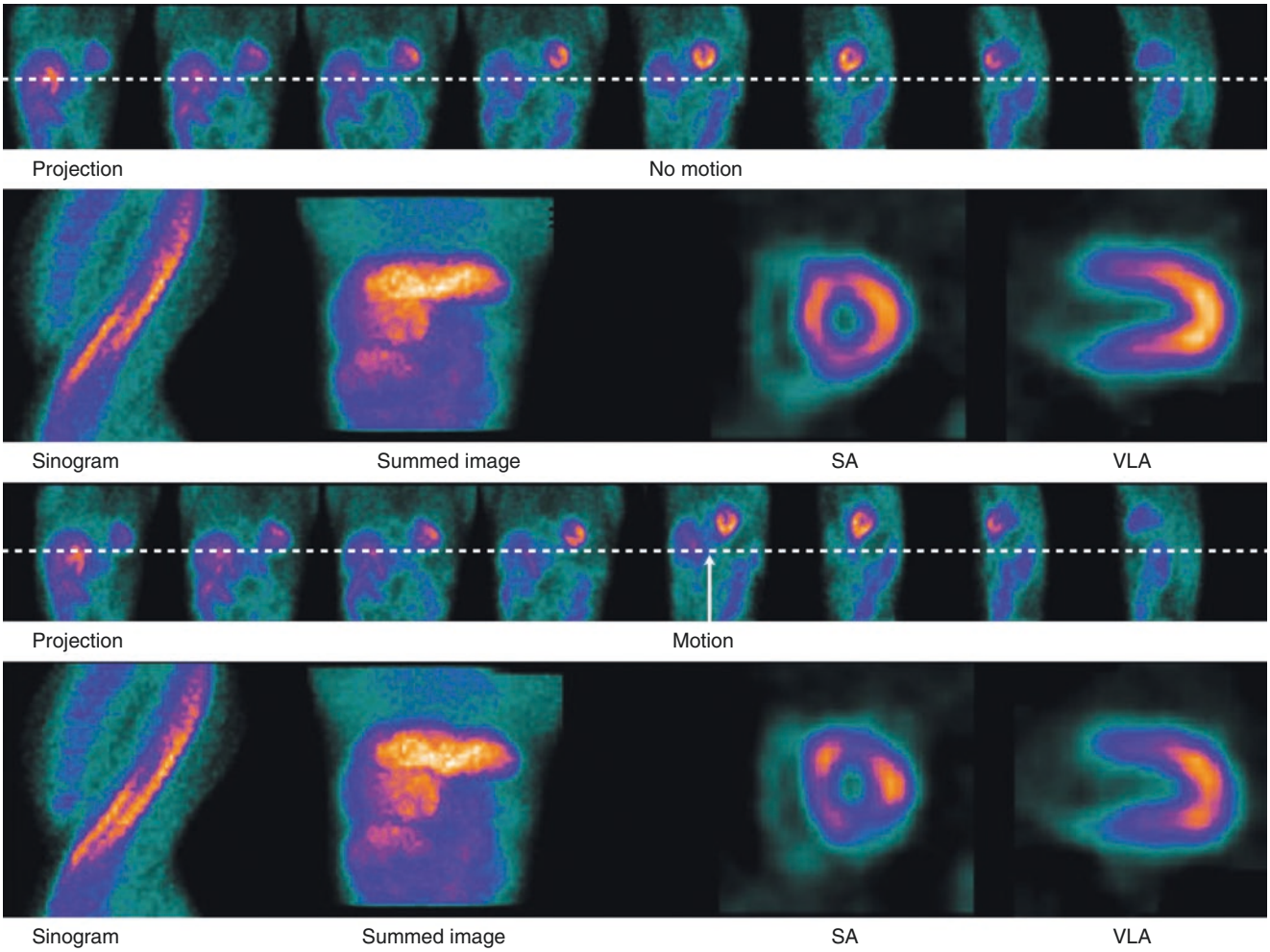

Fig. 2.43 Detecting patient motion. Patient motion can be detected by cine displays, sinograms, and summed planar images. Cine displays of the planar projections are perhaps the simplest and best way to detect patient motion. Watching the heart as it moves from right to left in the planar projections can be used to detect all types of motions. The clinician should watch the movie of the planar projections at a fairly rapid cine rate and observe any up-and-down motion of the heart, particularly in relation to a fixed horizontal line just below the heart. The best way to detect and correct motion is for the technologist to observe the patient and repeat the scan if sufficient motion occurs, to prevent the patient from having to return for a repeated scan if the original acquisition is technically impossible to interpret. The projections at the top of each of the two panels illustrate how patient motion might be detected using a cine display. If the distance between the heart and the horizontal line is compared in each of these planar projections, the *top images* show no variation in the distance between the inferior wall of the left ventricle and the line, whereas in the *bottom panel*, the heart is seen to move vertically away from the line starting with the projection to which the *arrow* points. Note that the short-axis (SA) and vertical long-axis (VLA) images in the *bottom panel* show regions of decreased counts as compared with those in the *upper panel* of the same patient with no motion. Even a slight amount of motion (3 mm) may result in an artifact in the SPECT images. If this motion is not detected by the clinician before interpreting the images, a false-positive report may result

A sinogram is another way to detect patient motion. A sinogram is an image composed of one line of pixels through the planar projections plotted vertically for each of the angular projection views. Thus, the *x-axis* of the sinogram represents pixels across the camera face, and the *y-axis* represents different planar projections, with the first planar projection at the *top*. The heart can be seen as a bright stripe from the top right to the lower left of the sinogram. The clinician looks for a break in this stripe, which would represent the patient moving to the left or right. Thus, sinograms are best for detecting horizontal motion across the table. Sinograms may also show vertical motion, but not quite as well as horizontal motion

Patient motion can also be detected by using summed projections. The summed projection is formed by adding all of the planar projections for the SPECT acquisition. The heart can be traced as a blurry horizontal line across the center of the image. To evaluate patient motion, the clinician should look for a change in the height of the heart that would indicate movement during the acquisition. This method is best used for detecting vertical motion—that is, motion of the patient along the table

There are a number of software algorithms, both manual and automatic, for correcting patient motion [29]. These algorithms work best when the motion is vertical along the table and no twisting motion has occurred. As with any algorithm, they may sometimes fail, although in general they correct for motion quite well. Sometimes, when these algorithms are applied to patients who have not moved during acquisition, the software gets confused and corrects for a nonexistent motion. It is advisable to always visually confirm that the motion correction software has performed appropriately

Advances in Cardiology Imaging

Figures 2.44, 2.45, 2.46, 2.47, 2.48, 2.49, 2.50, 2.51, 2.52, 2.53, 2.54, 2.55, and 2.56 illustrate some recent advances in imaging systems for cardiology.

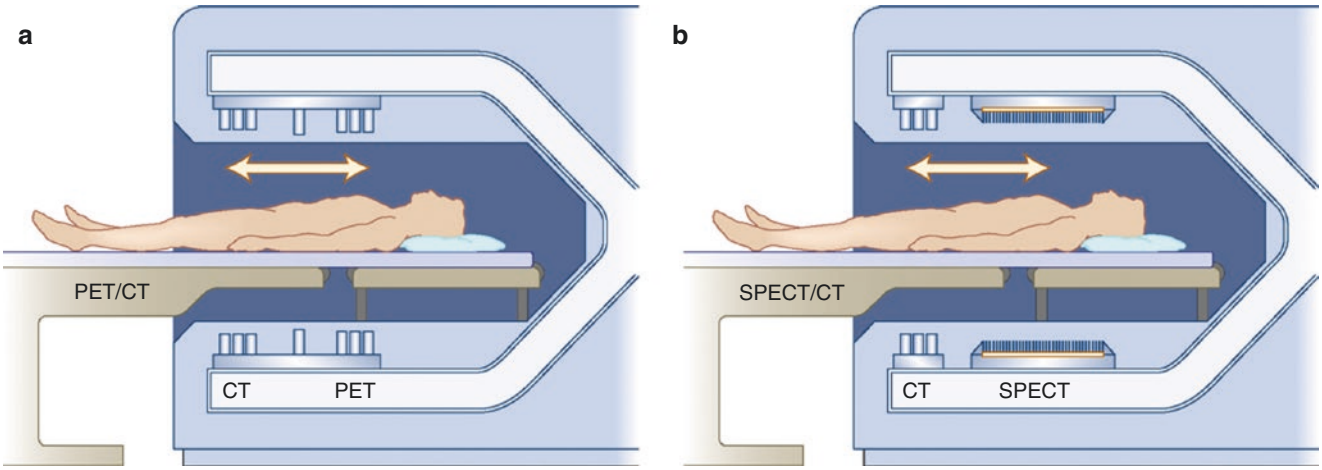

Fig. 2.44 Hybrid PET/CT and SPECT/CT imaging systems. Hybrid systems, which physically couple a CT scanner with a PET (**a**) or a SPECT (**b**) scanner, are now in routine clinical use. The coupled CT scanner, ranging from 1 to 64 slices, is commonly used for attenuation correction and, if supported by the CT scanner, can be used to evaluate coronary calcium and/or perform CT angiographic studies. An advantage of these systems is that they can provide comprehensive cardiac evaluation of anatomic information from the CT scan and physiologic information from the PET or SPECT scans in a single imaging study [30]

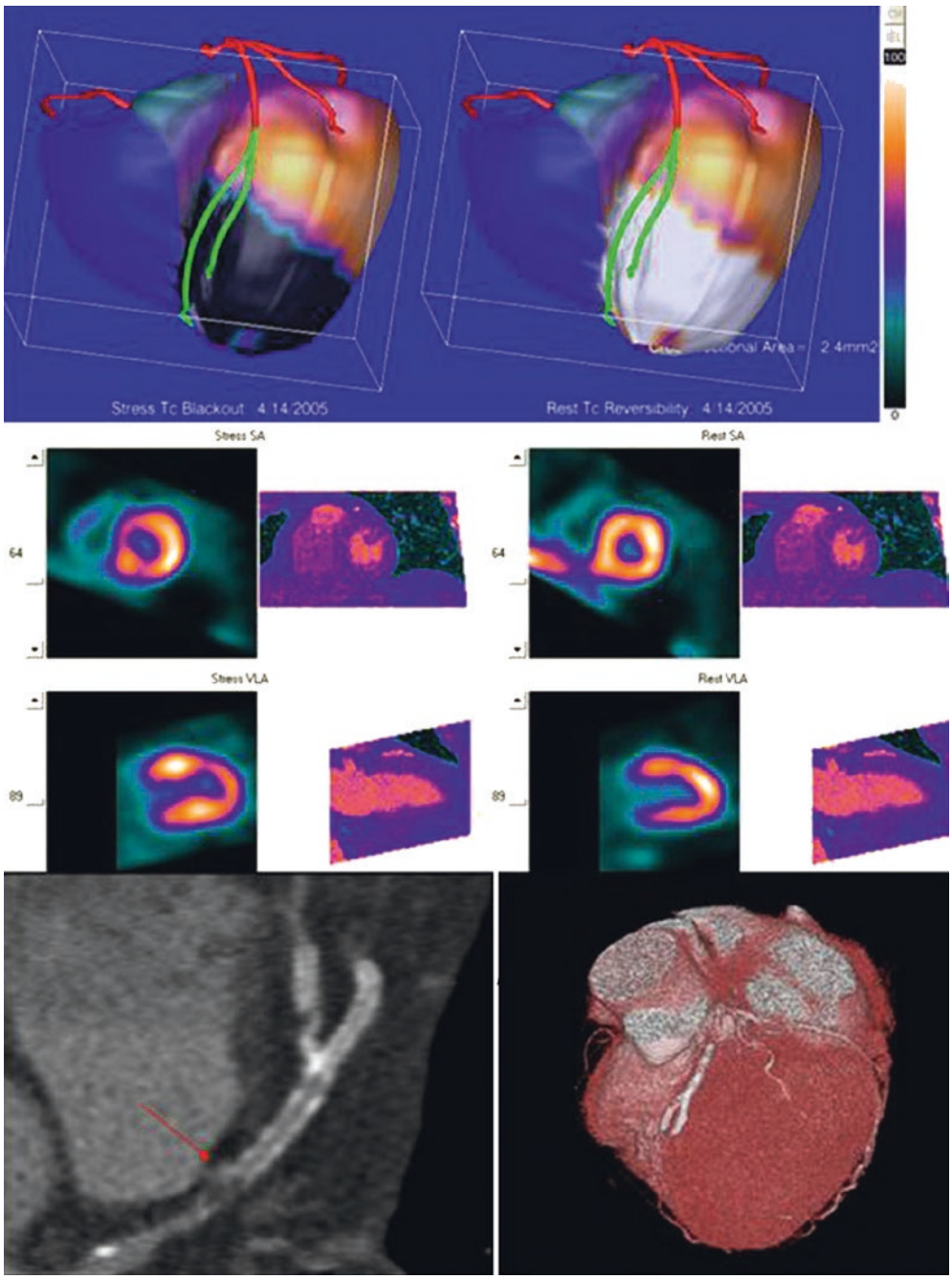

Fig. 2.45 PET/CT and SPECT/CT image fusion. Software methods are required to fuse the anatomic information from the CT angiographic (CTA) study and the physiologic information from a nuclear myocardial perfusion PET or SPECT study in three dimensions (3D). Because the emission and transmission studies are not acquired simultaneously, software fusion is needed regardless of whether a hybrid system or two stand-alone systems are used to acquire the information. Two types of fusion are used today: quantitative and qualitative fusion. In *quantitative* fusion, the 3D coronary tree is extracted from the CTA study and superimposed onto the 3D myocardial perfusion distribution using landmarks and shape operators [31]. In this approach, the quantitatively determined hypoperfused regions are highlighted in *black*, and the vessels distal to a coronary stenosis are highlighted in *green*. Compared with the accuracy of CTA, this fused information has been shown to provide significantly higher specificity and positive predictive value at no loss of sensitivity or negative predictive value [32]. This quantitative fusion approach has also been clinically validated to demonstrate increased diagnostic quality for detecting and localizing coronary artery disease compared with side-by-side displays of the nonfused perfusion and CT information [33]. In the *qualitative* approach, the 3D surface-rendered CTA study (*top right*) is painted with the 3D myocardial perfusion distribution angled in the same orientation as the CTA study. This fused qualitative information has also been reported to improve diagnostic accuracy over CTA [34]. More recently, a second-generation quantitative fusion approach has been developed, which combines the attributes of both the quantitative and qualitative approaches and uses the right ventricular epicardium for improved fusion of the arteries [35]. Shown here is the second-generation fusion of a patient with >70% stenosis in the left anterior descending coronary artery (LAD), just proximal to the stent. *Top* fusion displays show the left ventricle and translucent right ventricle detected from the CTA, color-coded for quantitative perfusion after automatic alignment of the SPECT study with the CT. Stress blackout is on the *left*, and reversibility whiteout is on the *right*. Coronary arteries are color-coded as *green* distal to the stenosis. *Middle* slice displays show aligned stress SPECT and (rest) CT coronary angiography (CTCA) on the left and rest SPECT and CTCA on the right. *Bottom* displays are zoomed multiplanar format of the stenosis in the LAD (*left*) and a typical 3D display generated from the CTA only (*right*)

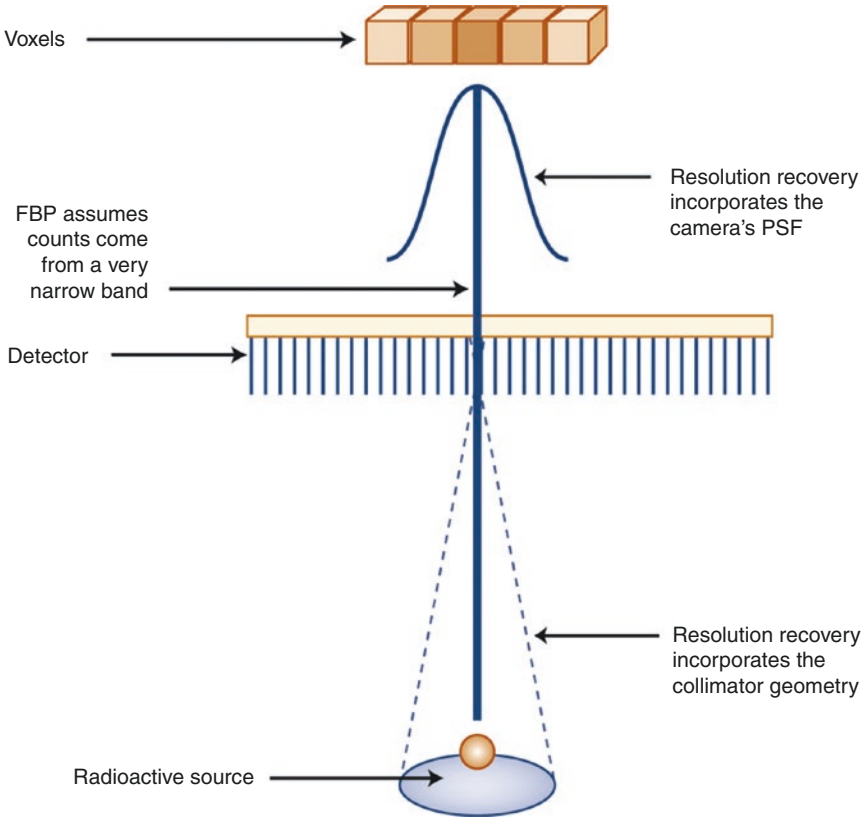

Fig. 2.46 Image reconstruction advances allow half-time acquisition. This diagram shows how conventional filtered backprojection (FBP) reconstruction assumes that the photons counted in a voxel over a collimator's parallel hole have emanated in a straight line from a radioactive source perpendicular to the detector surface and aligned with the hole. It assumes that all other photons counted from this source are either image noise or counts from other sources positioned in a very narrow line parallel to and directly in front of the hole. Recent software improvements in image reconstruction take into account the loss of resolution with distance that is inherent in parallel-hole collimators, depicted here by the cone drawn as a dashed line [36, 37]. Using this knowledge in conjunction with the properties of the entire point spread function (PSF) allows for a more accurate resolution recovery. In principle, instead of backprojecting the acquired counts from the planar projection in a straight line, the counts are backprojected (iteratively) along a cone

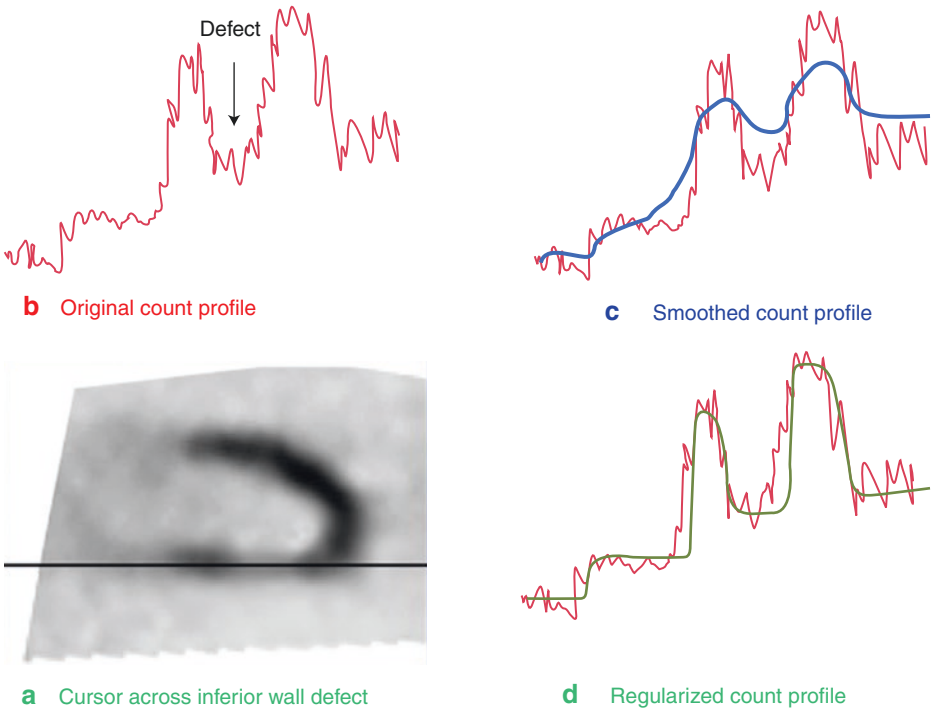

Fig. 2.47 Effect of noise regularization on defect contrast. At the same time the resolution recovery is performed, noise is suppressed or regularized because additional counts are now correctly considered (modeled) rather than treated as noise. (**a**) A vertical long-axis myocardial perfusion SPECT tomogram of a patient with a hypoperfused defect in the inferior wall. (**b**) What a noisy count profile across the inferior wall might look like if the study was not corrected for noise; the defect contrast is demonstrated as the region of reduced counts between the two normal increased count regions (albeit noisy). The larger the difference in counts between the defect and the normal region, the larger the defect contrast and the easier it is to detect it. (**c**) Superimposed on the original noisy count profile is what a conventional smooth count profile (*yellow*) might look like. The jagged high-frequency noise has disappeared, but taking with it the defect borders, reducing the difference in counts between the normal and hypoperfused regions, and thus reducing the defect contrast. (**d**) Superimposed on the original noisy count profile is a regularized count profile (*green*), which has been modeled using *a priori* physical knowledge of the imaging system. The jagged high-frequency noise has now been removed but the original defect contrast has been preserved, thus making it possible to reduce noise without compromising image contrast. It has been reported that SPECT myocardial perfusion imaging may be performed with these new resolution recovery/noise regularization algorithms using half the conventional scan time without compromising perfusion imaging results [38]. In another study, it was shown that these new algorithms, applied to half-time ECG-gated myocardial perfusion imaging SPECT acquisitions, compare favorably with the filtered backprojection (FBP) of full-time algorithms in image quality and the correlation of functional parameters. However, systematic offset in these functional parameters was reported owing to the increase in contrast of the resolution recovery–gated images over FBP images [39]

Fig. 2.48 Limitations of conventional SPECT imaging. Myocardial perfusion SPECT imaging has had widespread clinical use, owing to its well-documented diagnostic accuracy for detecting coronary artery disease. Nevertheless, the basic camera design is more than 50 years old and limited when using standard parallel-hole collimators to image the heart, as it uses only a small portion of the available, useful sodium iodide (NaI) crystal detector area

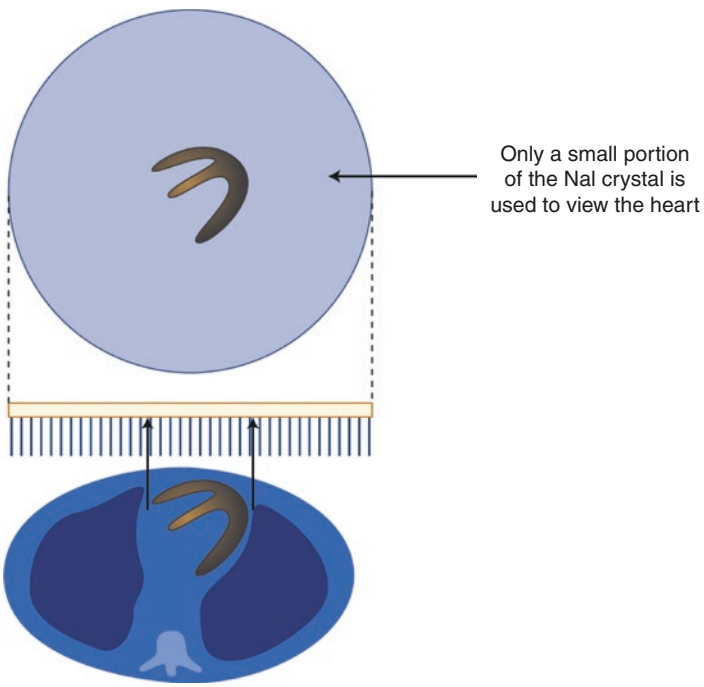

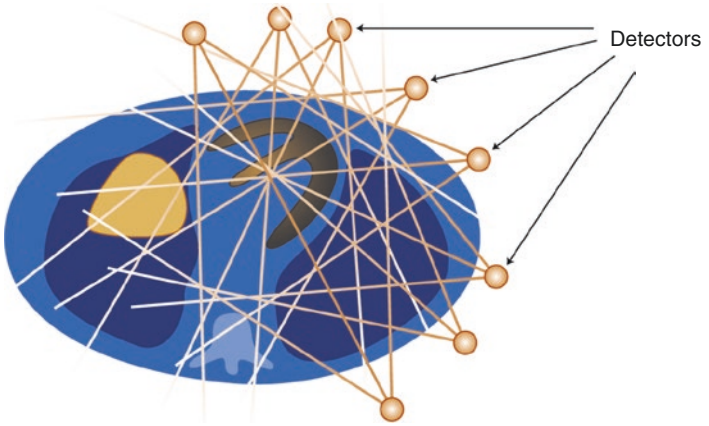

Fig. 2.49 Design of new-generation dedicated cardiac ultrafast acquisition scanners. Several manufacturers have begun to break away from the conventional SPECT imaging approach to create innovative designs of dedicated cardiac scanners. These scanners' designs have in common that all available detectors are constrained to imaging only the cardiac field of view. This diagram shows how eight detectors surrounding the patient are all simultaneously imaging the heart. These new designs vary in the number and type of scanning or stationary detectors and whether sodium iodide or cadmium zinc telluride solid-state detectors are used. They all have in common the potential for a fivefold to tenfold increase in count sensitivity at no loss (or even a gain) in resolution, resulting in the potential for acquiring a stress myocardial perfusion scan in 2 minutes or less with injection of a standard dose [36, 37, 40]

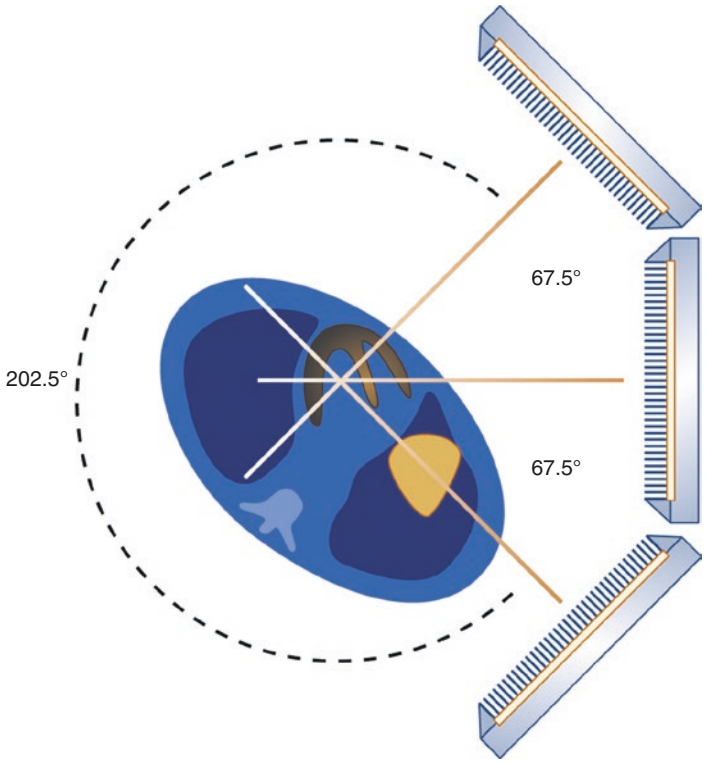

Fig. 2.50 Cardius® 3 XPO system configuration (Digirad; Suwanee, GA). This diagram shows how patient data are acquired with the Cardius® 3 XPO camera by keeping the three detectors stationary and simultaneously imaging the heart while the chair on which the patient is seated is rotated through a 202.5° arc. This commercial system is one of the first systems developed to take advantage of solid-state electronics and use more than two detectors simultaneously for imaging the heart. It uses 768 pixilated, thallium-activated cesium iodide [CsI(Tl)] crystals coupled to individual silicon photodiodes and digital Anger electronics to create the planar projection images used for reconstruction [41]. This image shows how the three detectors are fixed using a 67.5° angular separation while the patient is rotated. The typical acquisition time for a study is 7.5 minutes. In a large multicenter trial using this device and resolution recovery reconstruction, a subset of 189 patients acquired using conventional doses was compared with conventional SPECT. Using this combination, the study showed that a 5-minute rest acquisition and a 4-minute stress acquisition yielded perfusion and function information from gated SPECT myocardial perfusion imaging studies, which were diagnostically equivalent to full-time acquisition and two-dimensional ordered-subsets expectation maximization reconstructions [41]

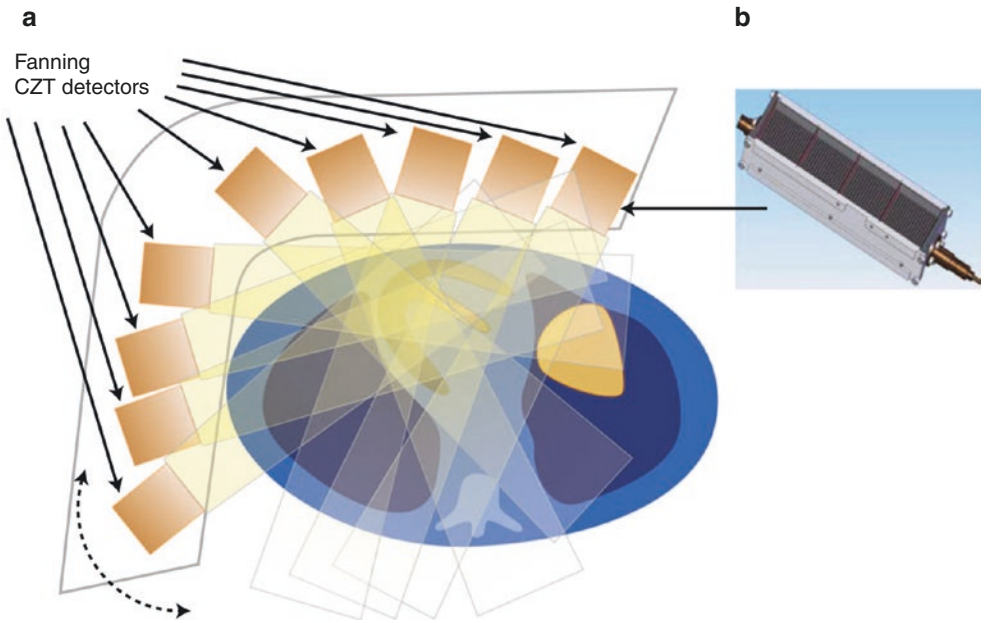

Fig. 2.51 D-SPECT® system configuration (Spectrum Dynamics Medical; Sarasota, FL). (**a**) This diagram is of the 9-cadmium-zinc-telluride (CZT) detector column configuration of the D-SPECT® system, in which each detector column uses a tungsten parallel-hole collimator that is fanned back and forth, constrained angularly to the heart's field of view. This is the first SPECT system to offer a totally different design [42–45]. This system uses solid-state detectors in the form of CZT mounted on nine vertical columns and placed in a 90° geometry, as shown in this figure. Each of the nine detector assemblies (**b**) is equipped with a tungsten, square, parallel-hole collimator. Each collimator square hole is 2.46 mm on its side, which is large in comparison to conventional collimators, which partially accounts for the increased count sensitivity. Each detector assembly is made to fan in synchrony with the other eight detector assemblies while all nine are simultaneously imaging the heart. The patient is imaged sitting in a reclining position, similar to a dentist's chair, with the patient's left arm placed on top of the detector housing

Data acquisition is performed by first obtaining a 1-minute scout scan for the nine detectors to identify the location of the heart, to set the limits of each detector's fanning motion. The actual diagnostic scan is then performed with each detector assembly fanning within the limits set from the scout scan. Reconstruction is performed using a modified iterative algorithm that compensates for the loss of spatial resolution that results from using large square holes in the collimator by mathematically modeling the acquisition, collimator, and left ventricle geometry

In a recent single-center clinical trial publication, it was concluded that using a stress/rest myocardial perfusion imaging (MPI) protocol and 4-minute and 2-minute D-SPECT® acquisitions yielded studies that highly correlated with 16-minute and 12-minute stress/rest conventional SPECT, with an equivalent level of diagnostic performance [42]. In a report of a multicenter trial using D-SPECT®, it was shown that using normal database quantitative analysis and a comparison protocol similar to the previous report correlated well with quantitative analysis of conventional SPECT MPI [43]. Another preliminary multicenter trial reported the potential for the D-SPECT® device to perform simultaneous Tl-201 (rest)/Tc-99m sestamibi (stress) 15-minute acquisitions [44]

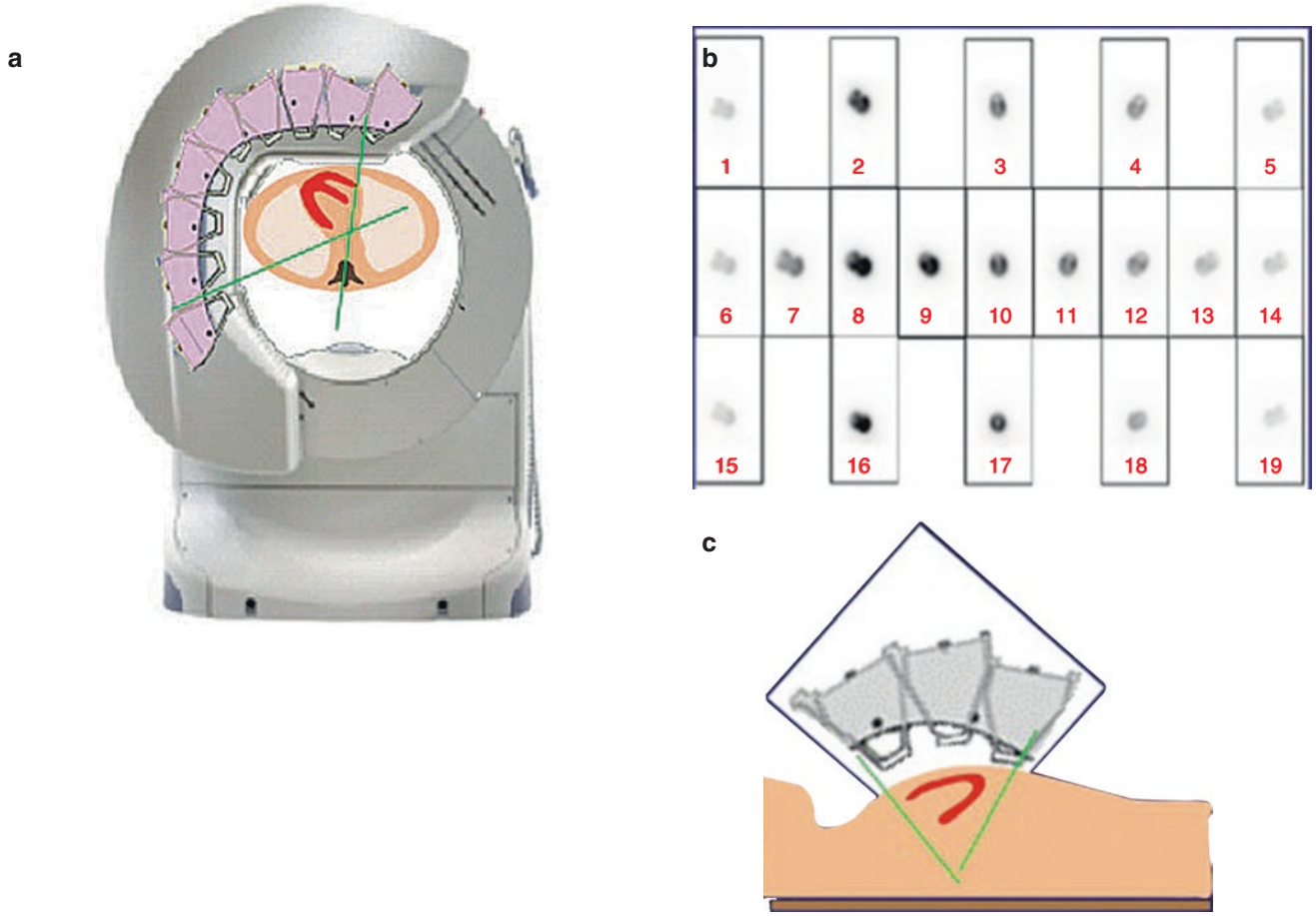

Fig. 2.52 Discovery NM 530c system configuration. The second SPECT system to offer a revolutionary new design is the system developed by GE Healthcare (Waukesha, WI) [45–48], known as the Discovery Nuclear Medicine (NM) 530c system. (**a**) The SPECT design uses Alcyone technology, consisting of an array of 19 pinhole collimators, each with four solid-state CZT pixilated detectors. (**b**) Projections from all 19 pinholes simultaneously image the heart, with no moving parts during data acquisition. Nine of the pinhole detectors are oriented perpendicular to the patient's long axis, five are angulated above the axis, and five below, for a true 3D acquisition geometry (**c**). The use of simultaneously acquired views improves the overall sensitivity and gives the complete and consistent angular data needed for both dynamic studies and for the reduction of motion artifacts. In addition, attenuation artifacts may be reduced because not all projections are viewed through the attenuator; some may view the heart from above or below. The detector assembly is mounted on a gantry that allows for patient positioning in the supine or prone positions

In the first multicenter trial, it was demonstrated that using a conventional 1-day technetium-99m (^{99m}Tc) tetrofosmin rest/stress MPI protocol and 4-minute and 2-minute Alcyone acquisitions yielded studies that diagnostically agreed 90% of the time with 14-minute and 12-minute rest/stress conventional SPECT acquisitions [46]. Importantly, this trial also showed excellent left ventricular ejection fraction correlations between the 530c and conventional SPECT for rest-gated MPI studies ($r = .93$, $P < 0.001$) and stress-gated MPI studies ($r = .91$, $P < 0.001$) [46]. A subsequent single-center trial was performed using a 1-day ^{99m}Tc tetrofosmin adenosine-stress/rest MPI protocol and a 3-minute scan for stress and 2 minutes for rest using the 530c camera compared with 15-minute conventional SPECT acquisitions for stress and rest [47]. These investigators concluded that the 530c camera allows a more than fivefold reduction in scan time and provides clinical perfusion and function information equivalent to conventional dual-head SPECT MPI

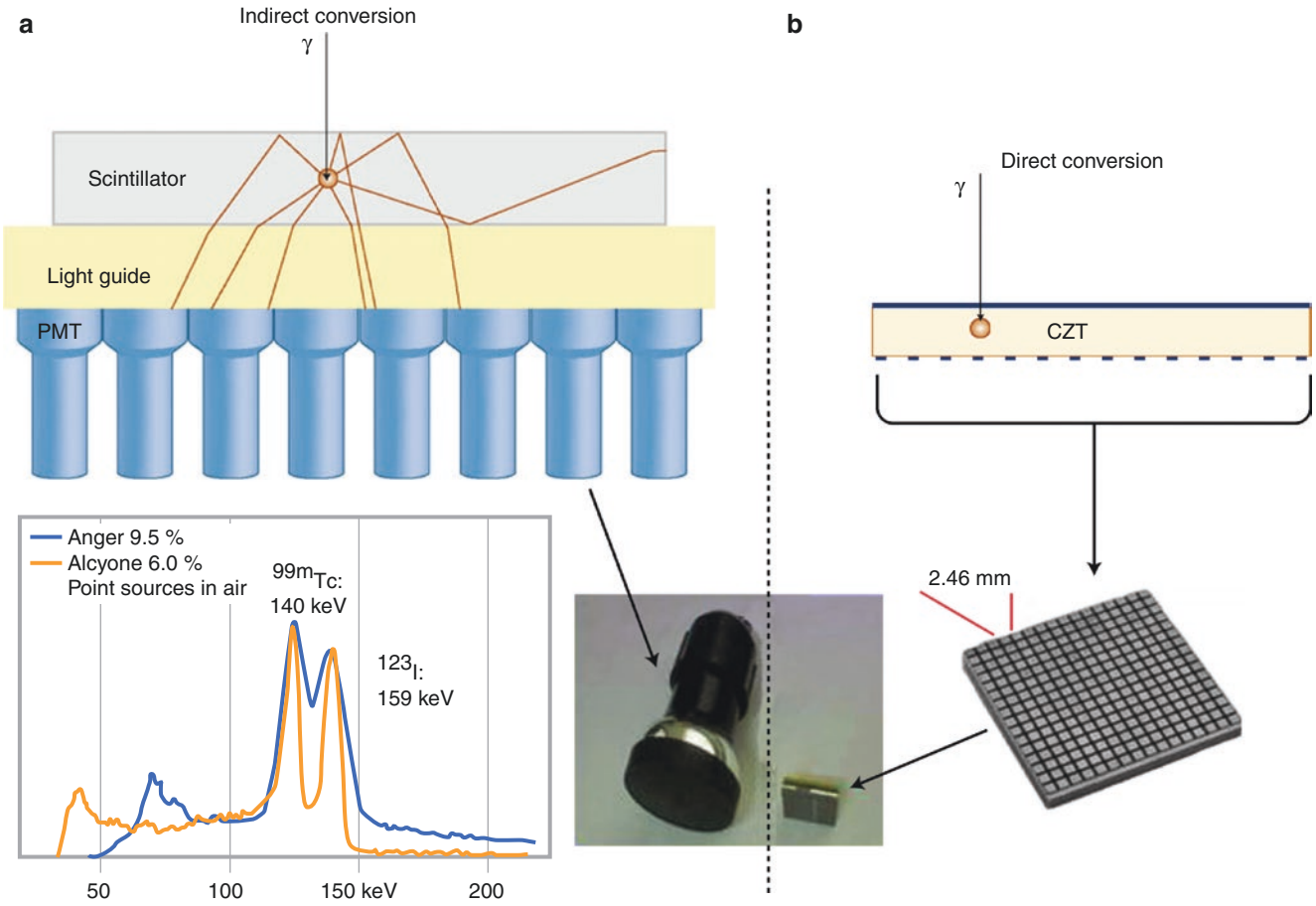

Fig. 2.53 Indirect versus direct radiation conversion. (**a**) Indirect conversion: This figure illustrates how a conventional second SPECT detector works where the NaI (Tl) crystal absorbs the γ-ray from the patient and converts its energy to visible photons, which are then converted to electrical pulses by the entire array of photomultipliers (PMT). The sum of all pulses is used as energy information, and the distribution of pulses provides the location of the event in the crystal. The large number of steps to reach these final data results is an opportunity for the information to be degraded as it is transferred from one system to another, thus reducing both the energy and spatial resolution of the system. (**b**) Direct conversion: This figure illustrates how a CZT detector works, where the detector absorbs the γ-ray from the patient, directly converting its energy to charge carriers that form an electrical pulse with the information of the energy of the event; the location is given by the location of the pixel within the CZT detector where the event took place. This more direct transfer of energy and location information results in superior energy and spatial resolution over conventional SPECT cameras. The *middle lower* insert compares the size of one photomultiplier tube (PMT) used in conventional SPECT versus the size of a CZT detector. The *lower left* panel illustrates the superior energy resolution of the CZT detector (*blue*) over conventional cameras (*purple*) by comparing a simultaneous acquisition of ^{99m}Tc and I-123 radioactive sources. (A*dapted from slides courtesy of* Aharon Peretz, Ph.D.)

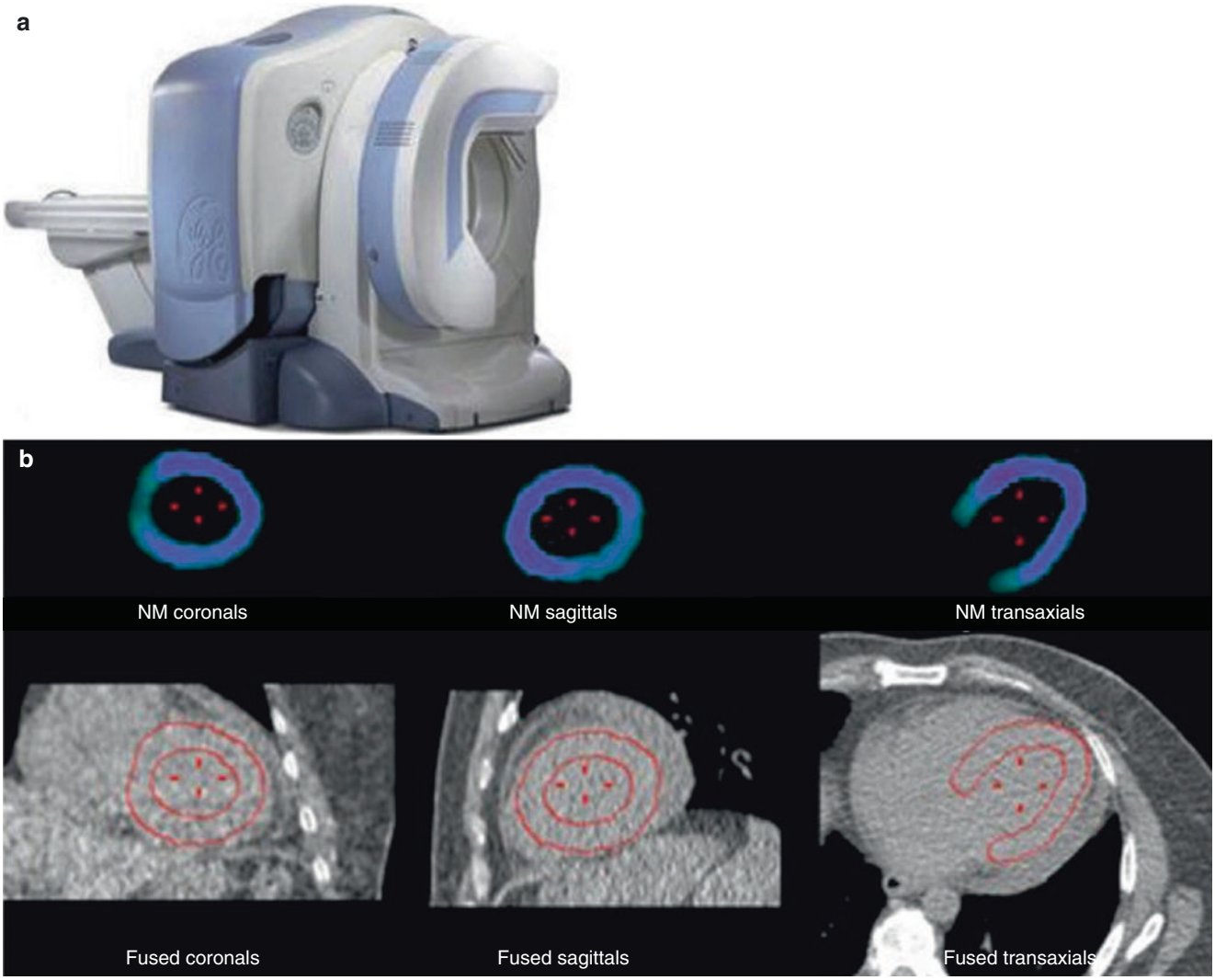

Fig. 2.54 Discovery Nuclear Medicine 570c system configuration. (**a**) The CZT detector assembly and gantry of the 530c system is physically coupled to a volumetric CT scanner for a fast SPECT/CT system configuration. (**b**) The *top row* shows the segmented SPECT images of the left ventricle (LV); the *bottom row* shows the overlay of the borders of these LV segments onto the CT transmission studies used for quality control and alignment of the emission and transmission studies. Iterative reconstruction adapted to this geometry is used to create transaxial slices of the heart and to perform attenuation correction [50, 51]

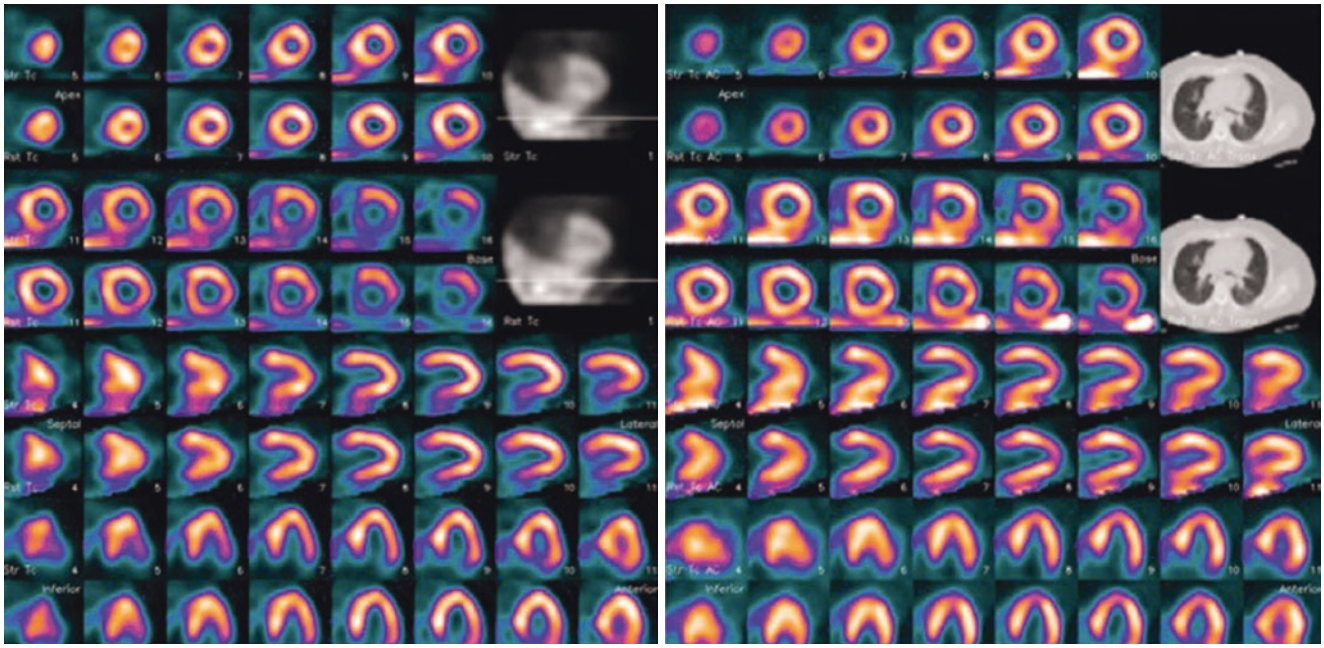

a Before AC **b** After AC

Fig. 2.55 Normal patient images with diaphragmatic attenuation used to illustrate the advantage of using attenuation correction (AC) with the Discovery NM 530c cardiac system. Results are shown from a patient who underwent rest/stress technetium-99m tetrofosmin MPI using 10 mCi for rest and 30 for stress. (**a**) 530c system images without AC are shown. Rest and stress acquisitions were 4 and 2 minutes, respectively. The figure shows short, vertical, and horizontal oblique axis slices starting with stress images in the *first row*, with the corresponding resting images immediately below. The *top right* black/white images show planar reprojections. Note the fixed defect in the inferobasal wall. (**b**) 530c system images with AC are shown. This is the same patient as in (**a**), but with the use of a CT transmission for AC, shown in the *top right* black/white panels. Note the increased tracer uniformity throughout the left ventricle and a normally perfused inferior wall

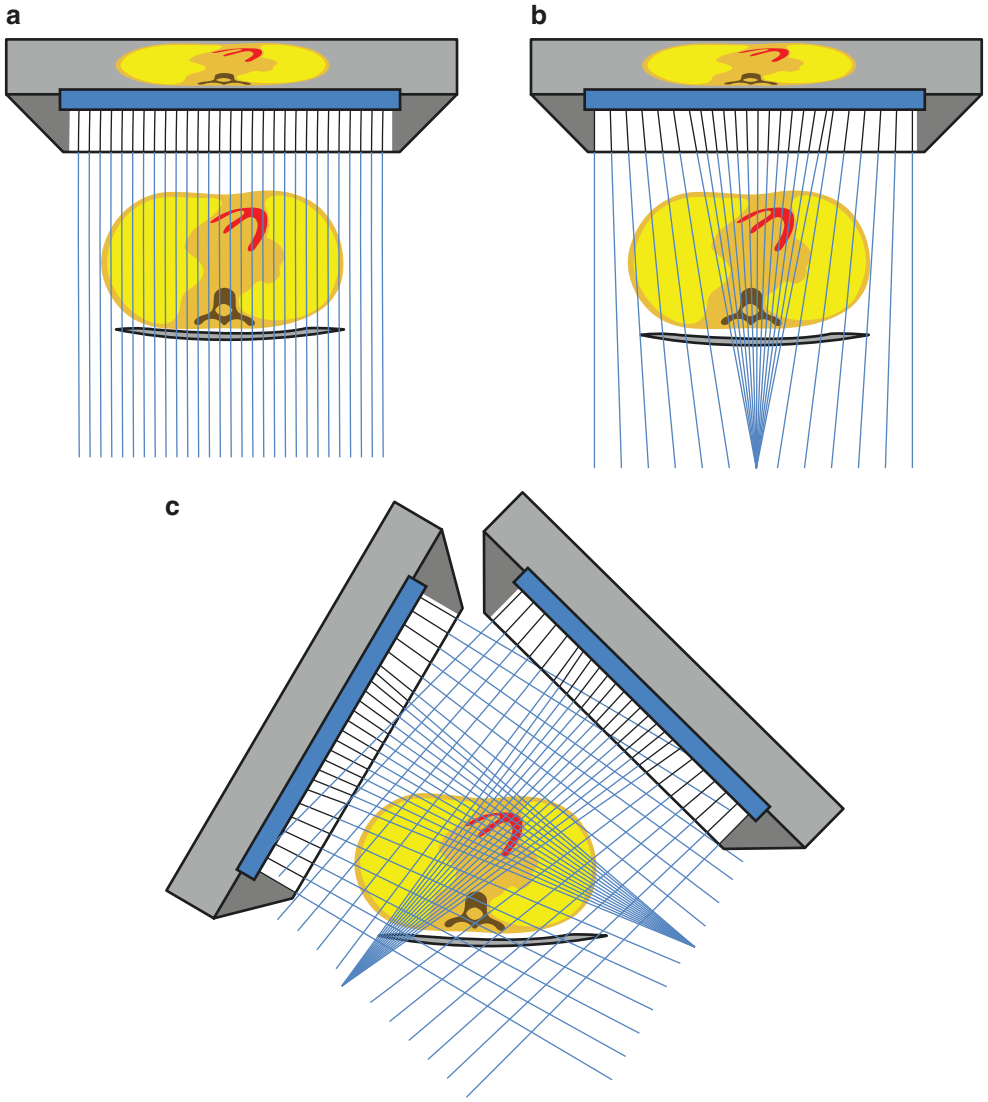

Fig. 2.56 The IQ•SPECT system (Siemens; Erlangen, Germany) achieves high sensitivity by using a unique collimator design mounted on a standard, large field-of-view, dual-detector SPECT or SPECT/CT system. The collimators used in IQ•SPECT have a central area with converging collimation designed to focus on the heart and transition to parallel-hole collimation around the periphery of the camera. This design allows increased sensitivity over the heart, where it is most needed, but avoids truncation of the body [52]. (**a**) The image of the heart formed by a parallel-hole collimator is the same size as the heart. (**b**) The IQ•SPECT collimator utilizes more of the crystal for the heart, at the expense of a smaller field of view. (**c**) The angle between the detectors is set to 76° and the heart is positioned so that it is in the region of highest magnification of both collimators throughout acquisition. Although slight mispositioning may be tolerable, poor patient set-up may be less forgiving than in standard parallel-hole collimation. Some have noted that attenuation artifacts may differ from those recognized with parallel-hole collimation and that attenuation-corrected images may be preferred [52]

The use of IQ•SPECT to reduce imaging time and/or radiopharmaceutical dose has been demonstrated. In one study, Lyon et al. [53] compared attenuation-corrected stress SPECT to IQ•SPECT using a dose of 925–1100 MBq (25–30 mCi) Tc-99m sestamibi. Several different count levels were simulated for IQ•SPECT, and were evaluated using system- and count- level–specific normal files. The study concluded that IQ•SPECT could be used to reduce both the dose and the time by half compared with conventional SPECT. Thus the standard dose could be reduced to below 550 MBq (15 mCi) and the imaging time reduced from 13 minutes (standard SPECT) to 7 minutes [53]

The high-sensitivity hardware designs discussed in Figs. 2.50, 2.51, 2.52, 2.53, 2.54, and 2.55 are dedicated-cardiac cameras, but only when the IQ•SPECT collimator is mounted is the system restricted to nuclear cardiology. When equipped with standard collimators, the system is a general-purpose SPECT or SPECT/CT, a factor that may appeal to clinics that also perform general nuclear medicine studies

Table 2.7 shows how some of the increased count sensitivity of these new systems may be traded off for a reduced injected dose and, thus, a reduced total effective dose to the patient. It is clear that these imaging systems with more efficient hardware and software also allow for high-quality images that are obtained using a lower injected radiopharmaceutical dose and, thus, a decrease in the radiation dose that is absorbed by the patient and staff. This reduction in dose comes at an increase in acquisition time, even if the total time is less than what has been traditionally used in conventional systems. Recently, the American Society of Nuclear Cardiology published an information statement [49] recommending that laboratories use imaging protocols that achieve a median dose of ≤9 mSv or less in MPI, and stress-first imaging is an important tool to meet this goal. Although many different protocols that may be implemented to accomplish this exposure goal, use of the more efficient hardware/software described would greatly facilitate this goal and allow for increases in efficiency over the imaging protocols used today.

Rest		Stress		Total	
Injected dose, *MBq*	Acquisition time, *min*	Injected dose, *MBq*	Acquisition time, *min*	Effective dose,[a] *MSv*	Acquisition time, *min*
370	4	1110	2	12	6
185	8	555	4	6	12
93	16	278	8	3	24

[a]Effective dose estimated from tissue dose coefficients using the International Commission on Radiological Protection (ICRP) Publication 60 tissue-weighting factors

Table 2.7 Reduced dose versus increased efficiency

References

1. Chandra R. Introductory physics of nuclear medicine. Philadelphia: Lea and Febiger; 1992.
2. Christensen EE, Curry TS, Dowdey JE. An introduction to the physics of diagnostic radiology. 2nd ed. Philadelphia: Lea and Febiger; 1978. p. 159.
3. Powsner RA, Powsner ER. Essentials of nuclear medicine physics. Malden: Blackwell Science; 1998.
4. Hubble JH, Seltzer SM. Tables of x-ray mass attenuation coefficients, and mass energy-absorption coefficients. Gaithersburg: National Institute of Standards and Technology; 1996. Available at: http://physics.nist.gov/PhysRefData/XrayMassCoef/tab1.html. Accessed Jul 2018.
5. Cherry SR, Sorenson JA, Phelps ME. Physics in nuclear medicine. Philadelphia: WB Saunders; 2003.
6. Beller GA, Bergmann SR. Myocardial perfusion imaging agents: SPECT and PET. J Nucl Cardiol. 2004;11:71–86.
7. Saha GB. Fundamentals of nuclear pharmacy. New York: Springer; 2003.
8. Anger HO. Scintillation camera with multichannel collimators. J Nucl Med. 1964;5:515–31.
9. Maublant JC, Peycelon P, Kwiatkowski F, Lusson JR, Standke RH, Veyre A. Comparison between 180° and 360° data collection in technetium-99m MIBI SPECT of the myocardium. J Nucl Med. 1989;30:295–300.
10. Hoffman EJ. 180° compared to 360° sampling in SPECT. J Nucl Med. 1982;23:745–6.
11. Knesaurek K, King MA, Glick SJ, Penney BC. Investigation of causes of geometric distortion in 180° and 360° angular sampling in SPECT. J Nucl Med. 1989;30:1666–75.
12. Garcia EV, Galt JR, Cullom SJ, Faber TL. Principles of myocardial perfusion SPECT imaging. North Billerica: DuPont Pharma; 1994. p. 30.
13. Galt JR, Garcia EV, Robbins WL. Effects of myocardial wall thickness on SPECT quantification. IEEE Trans Med Imaging. 1990;9:144–50.
14. Shepp LA, Vardi Y. Maximum likelihood reconstruction for emission tomography. IEEE Trans Med Imaging. 1982;1:113–22.
15. Hudson HM, Larkin RS. Accelerated image reconstruction using ordered subsets of projection data. IEEE Trans Med Imaging. 1994;13:601–9.
16. Jaszczak RJ, Greer KL, Floyd CE Jr, Harris CC, Coleman RE. Improved SPECT quantification using compensation for scattered photons. J Nucl Med. 1984;25:893–900.
17. Ogawa K, Ichihara T, Kubo A. Accurate scatter correction in single photon emission CT. Ann Nucl Med Sci. 1994;7:145–50.
18. Glick SJ, Penney BC, King MA, Byrne CL. Noniterative compensation for the distance-dependent detector response and photon attenuation in SPECT imaging. IEEE Trans Med Imaging. 1994;13:363–74.
19. Zeng GL, Gullberg GT, Tsui BM, et al. Three-dimensional iterative reconstruction algorithms with attenuation and geometric point response correction. IEEE Trans Med Imaging. 1990;22:1475–9.
20. Smith WH, Kastner RJ, Calnon DA, Segalla D, Beller GA, Watson DD. Quantitative gated single-photon emission computed tomography imaging: a counts-based method for display and measurement of regional and global ventricular systolic function. J Nucl Cardiol. 1997;4:451–63.
21. Machac J, Chen H, Almeida OD, et al. Comparison of 2D and high dose and low dose 3D gated myocardial Rb-82 PET imaging [abstract]. J Nucl Med. 2002;43:777.
22. Karp JS, Surti S, Daube-Witherspoon ME, Muehllehner G. Benefit of Time-of-Flight in PET: Experimental and clinical results. J Nucl Med. 2008;49(3):462–70.
23. Schaart DR, van Dam HT, Seifert S, Vinke R, Dendoover P, Lohner H, Beekman FJ. SiPM-Array Based PET detectors with depth-of-interaction correction. IEEE Nuc Sci Symposium Conference Record. 2008:3581–5.

24. Schelbert HR, Beanlands R, Bengel F, Knuuti J, Dicarli M, Machac J, Patterson R. PET myocardial perfusion and glucose metabolism imaging: Part 2-Guidelines for interpretation and reporting. J Nucl Cardiol. 2003;10:557–71.
25. Dorbala S, Ananthasubramaniam K, Armstrong IS, Chareonthaitawee P, DePuey EG, Einstein AJ, et al. Single photon emission computed tomography (SPECT) myocardial perfusion imaging guidelines: instrumentation, acquisition, processing, and interpretation. J Nucl Cardiol. 2018;25(5):1784–46.
26. Nichols KJ, Galt JR. Quality control for SPECT imaging. In: DePuey EG, Garcia EV, Berman DS, editors. Cardiac SPECT imaging. 2nd ed. New York: Lippincott Williams & Wilkins; 2001. p. 17–39.
27. DePuey EG. Artifacts in SPECT myocardial perfusion imaging. In: DePuey EG, Garcia EV, Berman DS, editors. Cardiac SPECT imaging. 2nd ed. New York: Lippincott Williams & Wilkins; 2001. p. 349.
28. DePuey EG, Garcia EV. Optimal specificity of thallium-201 SPECT through recognition of imaging artifacts. J Nucl Med. 1989;30:441–9.
29. Geckle WJ, Frank YL, Links JM, Becker LC. Correction for patient motion and organ movement in SPECT: application to exercise thallium-201 cardiac imaging. J Nucl Med. 1988;29:441–50.
30. Di Carli MF, Hachamovich R. New technology for noninvasive evaluation of coronary artery disease. Circulation. 2007;115:1464–80.
31. Faber TL, Santana CA, Garcia EV, Candell-Riera J, Folks RD, Peifer JW, et al. Three-dimensional fusion of coronary arteries with myocardial perfusion distributions: clinical validation. J Nucl Med. 2004;45:745–53.
32. Rispler S, Keidar Z, Ghersin E, Roguin A, Soil A, Dragu R, et al. Integrated single-photon emission computed tomography and computed tomography coronary angiography for the assessment of hemodynamically significant coronary artery lesions. J Am Coll Cardiol. 2007;49:1059–67.
33. Santana CA, Garcia EV, Faber TL, Sirineni GK, Esteves FP, Sanyal R, et al. Diagnostic performance of fusion of myocardial perfusion and computed tomography coronary angiography. J Nucl Cardiol. 2009;16:201–11.
34. Gaemperli O, Schepis T, Valenta I, Husmann L, Scheffel H, Duerst V, et al. Cardiac image fusion from stand-alone SPECT and CT: clinical experience. J Nucl Med. 2007;48:696–703.
35. Faber TL, Arepalli CD, Nye JA, et al. Second generation fusion of myocardial perfusion distributions with coronary artery data from CT angiography. J Nucl Cardiol. 2010;17(4):724–722 (abstr).
36. Garcia EV, Faber TL. New trends in camera and software technology in nuclear cardiology. Cardiol Clin. 2009;27:227–36.
37. Garcia EV, Faber TL, Esteves FP. Cardiac dedicated ultrafast SPECT cameras: new designs and clinical implications. J Nucl Med. 2011;52:210–7.
38. Borges-Neto S, Pagnanelli RA, Shaw LK, Honeycutt E, Shwartz SC, Adams GL, Coleman RE. Clinical results of a novel wide beam reconstruction method for shortening scan time of Tc-99m cardiac SPECT perfusion studies. J Nucl Cardiol. 2007;14:555–65.
39. DePuey EG, Gadiraju R, Clark J, Thompson L, Anstett F, Shwartz SC. Ordered subset expectation maximization and wide beam reconstruction "half-time" gated myocardial perfusion SPECT functional imaging: a comparison to "full-time" filtered backprojection. J Nucl Cardiol. 2008;15:547–63.
40. Sharir T, Slomka PJ, Berman DS. Solid-state SPECT technology: fast and furious. J Nucl Cardiol. 2010;17:890–6.
41. Maddahi J, Mendez R, Mahmarian J, Thomas G, Babla H, Bai C, et al. Prospective multi-center evaluation of rapid gated SPECT myocardial perfusion upright imaging. J Nucl Cardiol. 2009;16:351–7.
42. Sharir T, Ben-Haim S, Merzon K, Prochorov V, Dickman D, Ben-Haim S, Berman DS. High-speed myocardial perfusion imaging: initial clinical comparison with conventional dual detector anger camera imaging. JACC Cardiovasc Imaging. 2008;1:156–63.
43. Sharir T, Slomka PJ, Hayes SW, DiCarli MF, Ziffer JA, Martin WH, et al. Multicenter trial of high-speed versus conventional single-photon emission computed tomography imaging: quantitative results of myocardial perfusion and left ventricular function. J Am Coll Cardiol. 2010;55:1965–74.
44. Ben-Haim S, Hutton BF, Van Grantberg D. Simultaneous dual-radionuclide myocardial perfusion imaging with a solid-state dedicated cardiac camera. Eur J Nucl Med Mol Imaging. 2010;37:1710–21.
45. Garcia EV, Tsukerman L, Keidar Z. A new solid state ultra fast cardiac multi-detector SPECT system. J Nucl Cardiol. 2008;15:S3 (abstr).
46. Esteves FP, Raggi P, Folks RD, Keidar Z, Askew JW, Rispler S, et al. Novel solid-state-detector dedicated cardiac camera for fast myocardial perfusion imaging: multicenter comparison with standard dual detector cameras. J Nucl Cardiol. 2009;16:927–34.
47. Buechel RR, Herzog BA, Husmann L, Burger IA, Pazhenkottil AP, Treyer V, et al. Ultrafast nuclear myocardial perfusion imaging on a new gamma camera with semiconductor detector technique: first clinical validation. Eur J Nucl Med Mol Imaging. 2010;37:773–8.
48. Herzog BA, Buechel RR, Katz R, Brueckner M, Husmann L, Burger IA, et al. Nuclear myocardial perfusion imaging with a cadmium-zinc-telluride detector technique: optimized protocol for scan time reduction. J Nucl Med. 2010;51:46–51.
49. Cerqueira MD, Allman KC, Ficaro EP, Hansen CL, Nichols KJ, Thompson RC, et al. Recommendations for reducing radiation exposure in myocardial perfusion imaging. J Nucl Cardiol. 2010;17:709–18.
50. Herzog BA, Buechel RR, Husmann L, Pazhenkottil AP, Burger IA, Wolfrum M, et al. Validation of CT attenuation correction for high-speed myocardial perfusion imaging using a novel cadmium-zinc-telluride detector technique. J Nucl Med. 2010;51:1539–44.
51. Pazhenkottil AP, Husmann L, Kaufmann PA. Cardiac hybrid imaging with high-speed single-photon emission computed tomography/CT camera to detect ischaemia and coronary artery obstruction. Heart. 2010;96:2050. https://doi.org/10.1136/hrt.2010.201996.
52. Gremillet E, Agostini D. How to use cardiac IQ•SPECT routinely? An overview of tips and tricks from practical experience to the literature. Eur J Nucl Med Mol Imaging. 2016;43:707–10.
53. Lyon MC, Foster C, Ding X, Dorbala S, Spence D, Bhattacharya M, et al. Dose reduction in half-time myocardial perfusion SPECT-CT with multifocal collimation. J Nucl Cardiol. 2016;23:657–67.